

# University of Naples Federico II



School of Engineering

Department of Chemical Engineering, Materials and  
Industrial Production

Ph.D in Engineering of Materials and Structures

## **ENGINEERED BUILDING BLOCKS TO PRINT ENDOGENOUS TISSUE AND COMPLEX ORGANS *IN VITRO***

Ph.D Thesis

Alessandro Garziano

### TUTOR

Prof. Paolo A. Netti

### COORDINATOR

Prof. Giuseppe Mensitieri

### ADVISORS

Giorgia Imparato Ph.D

Francesco Urciuolo Ph.D

April 2015



*...à Chiara...*



# CONTENTS

<b>INTRODUCTION</b>	<b>11</b>
<b>CHAPTER 1</b>	
<b>ENGINEERED BIO-INK FOR TISSUE PRINTING</b>	<b>16</b>
<b>1.1 Introduction</b>	<b>16</b>
<b>1.2 Material and methods</b>	<b>20</b>
1.2.1 Microscaffold production	20
1.2.2 Cell expansion	22
1.2.3 Bio-ink engineering	22
HD- $\mu$ TP culture	22
Cell proliferation on HD- $\mu$ TP	23
1.2.4 HD- $\mu$ TP morphology	23
Immunofluorescence and multiphoton imaging	23
Histology	24
1.2.5 Dynamic interaction among HD- $\mu$ TPs	25
Multi particles tracking	25
1.2.6 collagen fraction quantification	27
1.2.7 Oxygen consumption kinetics measurements	27
1.2.8 Realization and characterization of 3D tissue	28
1.2.9 Engineered bio-ink printing	31
1.2.10 Characterization of symbolic shape	32
<b>1.3 Results</b>	<b>33</b>
1.3.1 $\mu$ TP Evolution: cell proliferation aggregation and remodeling	33
1.3.2 $\mu$ TP Evolution: metabolic and biosynthetic activity	36
1.3.3 $\mu$ TP age on final 3D tissue printed	38
1.3.4 Collagen distribution in the 3D printed tissue	39
1.3.5 Characterization of symbolic shape	41
<b>1.4 Discussion</b>	<b>43</b>
<b>CHAPTER 2</b>	
<b>MICROFLUIDIC DEVICE AS SCREENING SYSTEM FOR 3D-TISSUE CULTURE</b>	
<b>CONDITION</b>	<b>48</b>
<b>2.1 Introduction</b>	<b>48</b>

<b>2.2 Material and methods</b>	<b>53</b>
2.2.1 Microscaffold production	53
2.2.2 Cell expansion	54
2.2.3 HD- $\mu$ TP culture	54
2.2.4 Device realization	55
2.2.5 Theoretical optimal flow rate calculation	57
2.2.6 Oxygen consumption rate and profile inside the chamber	58
2.2.7 Live/dead assay	59
2.2.8 Collagen observation and quantification	60
2.2.9 Immunofluorescence on HD- $\mu$ TP and quantification	61
<b>2.3 Results</b>	<b>62</b>
2.3.1 Features of the device design	62
2.3.2 Oxygen consumption rate and profile inside the chamber	63
2.3.3 Cells viability VS flow rate	65
2.3.4 MMP-1 profile	66
2.3.5 SHG intensity VS flow rate	67
2.3.6 SHG intensity VS ascorbic acid concentration	69
<b>2.4 Discussion</b>	<b>70</b>
<b>CHAPTER 3</b>	
<b>3D AIRWAY EPITHELIUM EQUIVALENT</b>	<b>74</b>
<b>3.1 Introduction</b>	<b>74</b>
<b>3.2 Material and methods</b>	<b>79</b>
3.2.1 Microscaffold production	79
3.2.2 Cell expansion	80
3.2.3 HL- $\mu$ TP culture	81
3.2.4 Realization of 3D human lung equivalent	81
3.2.5 Realization of human bronchial epithelium	82
3.2.6 Immunofluorescence, mutiphoton imaging and histology on HL- $\mu$ TP	83
3.2.7 Scanning Electron microscopy	85
<b>3.3 Results</b>	<b>85</b>
3.3.1 HL- $\mu$ TP Evolution: cell proliferation and biosynthetic activity	85
3.3.2 Morphological analysis of human lung equivalent	87
3.3.3 Morphological analysis of 3D human bronchial epithelium equivalent	90
<b>3.4 Discussion</b>	<b>92</b>

<b>CHAPTER 4</b>	
<b>HUMAN SKIN EQUIVALENT MAINTAINS EXOGENOUS HAIR VIABILITY AND FUNCTIONALITY</b>	<b>95</b>
<b>4.1 Introduction</b>	<b>95</b>
<b>4.2 Materials and Methods</b>	<b>100</b>
4.2.1 Microscaffold production	100
4.2.2 Cell expansion	101
4.2.3 HD- $\mu$ TP culture	102
4.2.4 Hair follicle extraction	102
4.2.5 Realization of 3D Human dermis equivalent with hair	103
4.2.6 Keratinocyte extraction from foreskin	104
4.2.7 Realization of human skin equivalent	105
4.2.8 Immunofluorescence, mutiphoton imaging and histology on biohybrids	106
4.2.9 Hair elongation measurement	107
<b>4.3 Results</b>	<b>109</b>
4.3.1 Morphological analysis of dermis equivalent	109
4.3.2 Hair elongation	111
<b>4.4 Discussion</b>	<b>113</b>
<b>CONCLUSION</b>	<b>116</b>
<b>REFERENCES</b>	<b>117</b>

# FIGURES

**Figure 1 Spheroid based tissue printing; Diagram of digital dispensing of spheroids in fluids (a); Tissue spheroids in loaded micro-pipette before dispensing (bi) and during (bii); Scheme for the bio-assembly of tubular tissue construct (c); Assembled ring like structure and tissue fusion process Labeled spheroids showing absence of cell mixing during the fusion process (di). Sequential steps during tissue fusion process (dii) adapted from [18]..... 17**

**Figure 2 Formation of millimeter-scale 3D tissue architectures by molding monodisperse cell beads. Method used to produce the 3D tissue architectures using monodisperse cell beads (a); A microscopy image of the doll-shaped PDMS mold chamber reveals 3D tissue formation (b); Microscopy images of NIH 3T3 cell beads immediately after stacking (c,d). Cavities (indicated with yellow arrows) among the cell beads are observed at this time point (0 h). Microscopy images of NIH 3T3 cell beads, 17 h after stacking (e,f). Adapted from [18]..... 18**

**Figure 3  $\mu$ tp evolution during culture time: nuclei ad actina distribution (a-d) and growth curve..... 34**

**Figure 4  $\mu$ tp evolution during culture time: H/E staining, scale bar 200  $\mu$ m (a-d); aggregation and diffusion coefficient ..... 36**

**Figure 5  $\mu$ tp collagen evolution (a-d) and quantification; maximum oxygen rate consumption. .... 37**

**Figure 6 effects of  $\mu$ tp age on the final 3D printed tissue; masson tricrome (a-e), picosirius red (f-l), immature and mature collagen quantification; scale bar 200  $\mu$ m..... 39**

**Figure 7 collagen distribution (a-e) acquired by second harmonic generation in the 3D printed tissue, and quantification ..... 40**

**Figure 8 Symbolic printed shape; nuclei staining, collgen and elastin MP exitation..... 42**

**Figure 9 spinner flask bioreactor..... 48**

**Figure 10 perfusion bioreactor..... 49**

**Figure 11 microfluidic device ..... 51**

**Figure 12 Device configuration ..... 56**

**Figure 13 perfusion chamber zoom..... 56**

**Figure 14 oxygen consumption rate measured during culture time ..... 64**

**Figure 15 simulation of oxygen profile inside the chamber for three several flow rate conditions: Q[0]; Q[1]; Q[-1]; oxygen concentration along length device. .... 65**

Figure 16 total cells number; live dead fraction VS flow rate at 0 days (a-f) and 4 days (g-n); fraction of live/dead cells quantification ..... 66

Figure 17 MMP-1 synthesis VS flow rate; MMP-1 in red, nuclei in blue, quantification of the red signal per cell ..... 67

Figure 18 volumetric collagen intensity VS flow rate ..... 68

Figure 19 Volumetric collagen intensity VS ascorbic acid concentration ..... 70

Figure 20 Schematic figure showing different steps of fabrication and configuration of the 3D tissue engineered airway epithelium. Calu-3 epithelial cells are seeded onto one PET scaffold and MRC-5 fibroblasts are seeded onto a second, separate scaffold (A). Following 72 h culture, scaffolds are combined by layering the epithelial scaffold monolayer on top of the fibroblast scaffold layer to form the coculture model. Cells are subsequently cultured for 2 weeks at the ALI to allow for differentiation of the epithelial cells, including establishment of tight junctions (B). Monocyte-derived DCs are seeded onto separate PET scaffolds and then inserted into the coculture model. The upper epithelial scaffold is temporally lifted away from the lower MRC-5 fibroblast layer so that the separate third scaffold containing dendritic cells may be placed on-top of the MRC-5 scaffold layer (C). The Calu-3 layer is placed on-top of the DC scaffold layer, resulting in the DC layer sandwiched between the epithelial and fibroblast scaffold layers to form the triculture model (D). adapted from [77] ..... 77

Figure 21 Development of the organotypic culture. Normal human bronchial epithelium contains ciliated columnar cells, mucous-producing goblet cells, and basal cells (A). To produce a bronchial “submucosa” in vitro, fibroblasts were combined with type I collagen, allowed to gel (B, top), then the gel was released from the dish and allowed to contract over a period of 4–7 days (B, bottom). Bronchial epithelial cells were then seeded onto the top of the gels and allowed to attach for 4 hr to create the organotypic culture. Cultures were submerged for 4 days, then placed into a 6-well insert which was fed from beneath by media placed into well below the insert (C), thereby leaving the upper surface of the tissue emerged from the media. Triplicate cultures were placed into each insert. Cultures were fed every other day, and harvested at various time points in culture. Adapted from [72] ..... 78

Figure 22 growth curve of NHLF per bead during culture time ..... 86

Figure 23 HL-  $\mu$ tp evolution during culture time: H/E staining during (a-e), SHG collagen signal (f-i) nuclei ad actina distribution (l-o)..... 87

Figure 24 comparison of human skin equivalent, airway epithelium equivalent and lung structure; H/E staining (a-d-g), SEM (b-e-h) and MP (c-f-i) image..... 89

<b>Figure 25 immunofluorescence analysis of histological section with thick 5 <math>\mu\text{m}</math> of human lung equivalent; Collagen I in green (a) and Collagen IV in red (b); scale bar 50 <math>\mu\text{m}</math> .....</b>	<b>89</b>
<b>Figure 26 Scanning electron microscopy (SEM) top view of bronchial epithelium, ciliate and goblet cells (a-b), cilia structures (d-e), transmission electron microscopy (TEM) section of bronchial epithelium stratification (e) and tight junction (f). scale bar: 1 <math>\mu\text{m}</math> (a-c) 100 nm (d), 2 <math>\mu\text{m}</math> (e), 200 nm (f). .....</b>	<b>91</b>
<b>Figure 27 immunofluorescence analysis of histological section with thick 5 <math>\mu\text{m}</math> of human bronchial epithelium; Keratine 14 in red and P63 in green (a); ZO-1 (b) .....</b>	<b>92</b>
<b>Figure 28 schematic illustration of principles of skin tissue engineering. Primary keratinocytes and fibroblasts are isolated from human donor tissues, which are then in vitro expanded prior seeding onto suitable scaffold materials/matrices. For a full-thickness skin equivalent, the fibroblasts and the matrix are initially used to establish the dermal part. The keratinocytes are seeded afterwards on the top of the dermis to ultimately form the epidermal part of the skin substitute. The in vitro-engineered skin can serve as skin graft or can be used as human-cell based in vitro test system. Adapted from [92].....</b>	<b>97</b>
<b>Figure 29 Commercially available skin substitutes .....</b>	<b>98</b>
<b>Figure 30 histological analysis of cross section of human skin equivalent with endogenous dermis. (A, B,C) hematoxylin and eosin staining and introduction of basal layer was indicated by black arrow ; (D,E,F) Masson trichrome staining. Adapted from [97].....</b>	<b>100</b>
<b>Figure 31 hair follicle cycle (a); hair implantation inside the maturation chamber (b) and 3D dermis equivalent with hair after two weeks of maturation time (c) ....</b>	<b>104</b>
<b>Figure 32 schematic procedure for human skin equivalent realization .....</b>	<b>106</b>
<b>Figure 33 H/E staining (a-b) and masson trichrome staining (d-e) of biohybrid with 4 weeks of maturation; scale bar 200 <math>\mu\text{m}</math> (a-d) and 50 <math>\mu\text{m}</math> (d-e); collagen signal acquired by SHG MP microscopy (c) and SEM image (f).....</b>	<b>110</b>
<b>Figure 34 hair elongation during maturation time; quantification of hair elongation in fresh medium, conditioned medium, exogenous collagen and cells, biohybrid .....</b>	<b>112</b>
<b>Figure 36 biohybrid with exogenous hair (a); H/E staining of human skin equivalent with hair implantation (b-c); immunofluorescence analysis of hair follicle, Versican in green and CD133 in red; H/E staining of exogenous hair bulb (e-f); scale bar 1mm (a), 200 <math>\mu\text{m}</math> (b), 50 <math>\mu\text{m}</math> (c-f).....</b>	<b>113</b>

# Introduction

The classical goal of tissue engineering is the production of functional tissues to substitute or restore *in vivo* a damaged tissue or its function. However the clinical applications of 3D tissue model, is not the only purpose for realizing *in vitro* functional 3D tissue equivalent. Indeed compared to conventional 2D cell cultures, that lack of adequate extracellular matrix [1] 3D *in vitro* models offer the possibility to study different mechanisms involved in many diseases, as drug screening platforms and have a great potential on reducing, in some cases, experiments performed on animals [2]. Although several strategies have been developed, the realization of high-fidelity tissue mimicking the structures and functions of the native tissues still remain a major challenge. Traditional tissue engineering strategies typically employ a “top-down” approach, in which cells are seeded on a biodegradable polymeric scaffold [3-5]. In top-down approaches, the cells are expected to populate the scaffold and create the appropriate extracellular matrix (ECM) and microarchitecture often with the aid of perfusion, growth factors [6, 7] and/or mechanical stimulation [8]. Top-down approaches often have difficulty in recreating the intricate microstructural features of tissues. Subsequently, from an engineering point of view, it was proposed to build tissues by assembling blocks mimicking those units in a “bottom-up” or “modular approach” [9-12]. This approach

brings versatility and scalability to the fabrication of *in vitro* tissue models. The fabrication of those tissue models necessitates of tools to create an initial architecture and to systematically manipulate their microenvironments in space and time [10]. One of the major challenges of “bottom-up” tissue engineering is to assemble modular tissues with specific micro architectures into macroscale engineered tissues, without changing the microarchitecture and cellular behavior of modular tissues [6]. In this scenario, the modular tissue engineering is emerging as new paradigm for the *in vitro* fabrication of 3D biological structures. Several kinds of micromodules were performed, but systems composed by an aggregate of cells, or cells embedded in an exogenous matrices, still represent an approximation of the real tissues. Thus, the fabrication of engineered micromodules able to control the synthesis and the assembly of an endogenous ECM, represents a formidable task. In this direction, our group developed a new class of tissue micromodules, named micro tissue precursor ( $\mu$ TP), which led to the formation of a completely endogenous 3D tissue [7, 13], this technique is applicable to several kinds of cells, in order to obtain several kind of tissues. How the process conditions and micro-scaffold degradation rate modulated the synthesis and the assembly of the newly-formed ECM in the final 3D tissue have been previously demonstrated [13].

In the first chapter of this work we proposed  $\mu$ tp as a new class of bio-ink for

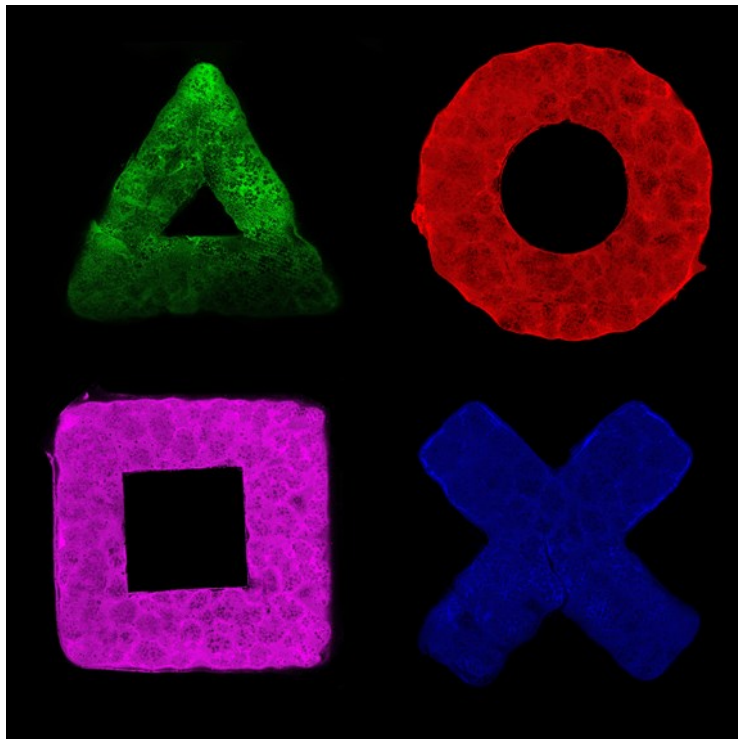
organ printing strategy and demonstrate that they evolve during culture time and strongly influence the morphology of the final printed tissue. We argue that the initial composition of the ECM present in the  $\mu$ TP change with  $\mu$ tp “age” and affects the maturation of the ECM in the final 3D tissue. We focused our attention on crucial aspects such as fusion capability, degree of maturation and mechanical properties of its ECM, as well as the evolution of oxygen consumption kinetic parameters. Finally we demonstrated the capability of  $\mu$ tp to be printed in unusual shapes meeting one of the need of organ printing strategy to overcome shape limitation and to obtain functional and complex tissues.

In the second chapter we proposed a model of TOC (tissue on chip) by inserted  $\mu$ TP in a microfluidic platform, designed in order to induce flow perfusion of the  $\mu$ TP. This micro-perfusion bioreactor, can be performed in order to evaluate the effect of flow rate and biochemical factors on the tissue development. By using this system together with  $\mu$ TP, it is possible in “short time” optimize the fluid dynamics parameters and bio-chemicals concentration inside the medium and evaluating the effect of external factors on the collagen assembly, cells viability and metalloproteinase synthesis. These capabilities made it an important tool for studying cause-effect relation, in particular how each single factor influences the tissue characteristics.

In the third chapter it is explored the possibility to realize  $\mu$ TP by using bronchial fibroblast in order to obtain “lung-stroma” on which build up bronchial epithelium. We found that  $\mu$ TP not only synthesize their own ECM, but that they organize it leading to a final tissue having a morphology very similar to native lung stroma. By seeding bronchial epithelial cells on this lung stroma, they differentiate and recreate the complete airway epithelium in air-liquid condition. Finally, by exploiting the knowledge of our group to recreate a human skin model, we evaluate its capability to maintains exogenous hair viability during the time, in terms of elongation capability and anagen phase of hair follicle maintenance. We realized a human skin model that, better than other competitors, is a good environment for the exogenous hair. This is a starting step in order to obtain a complete model that itself recapitulate all the hair follicle structures.

# Chapter 1

Engineered bio-ink for tissue printing



# Chapter 1

## 1.1 Introduction

In the field of tissue engineering, the reconstruction of organs and tissues for use as living replacement parts in the body and as pharmacokinetic models is a major challenge [14]. To achieve this goal, cells must be grown in an environment similar to that found in living tissues [15]. Many types of cells *in vivo* interact with other cells and with extracellular matrices (ECMs) within three-dimensional (3D) structures [16]. The cell–cell and cell–ECM interactions provide mechanical and biochemical cues that can influence cellular function and differentiation [14]. Therefore, 3D cell culture models combining cells and ECMs should be used to mimic and analyze the cellular functions of living tissues [16]. However, it is difficult to mimic dense and complex cellular morphologies in living tissues using conventional 3D cellular constructs produced using large biodegradable scaffolds [14–16]. Actually, these materials cannot represent the complexity of natural extracellular matrices (ECMs) and thus are inadequate to recreate a microenvironment with cell–cell connections and three-dimensional (3D) cellular organization that are typical of living tissues [17]. A potential solution would be to produce composite printable microcarriers (MCs) [7, 13]. The MCs are particles designed to promote attachment and survival of adherent cells, due to their small size they offer a very high specific surface

area for cell proliferation [13]. Tissues are so fabricated in the form of micromodules, obtained by either cellular spheroids (fig. 1) [18, 19]

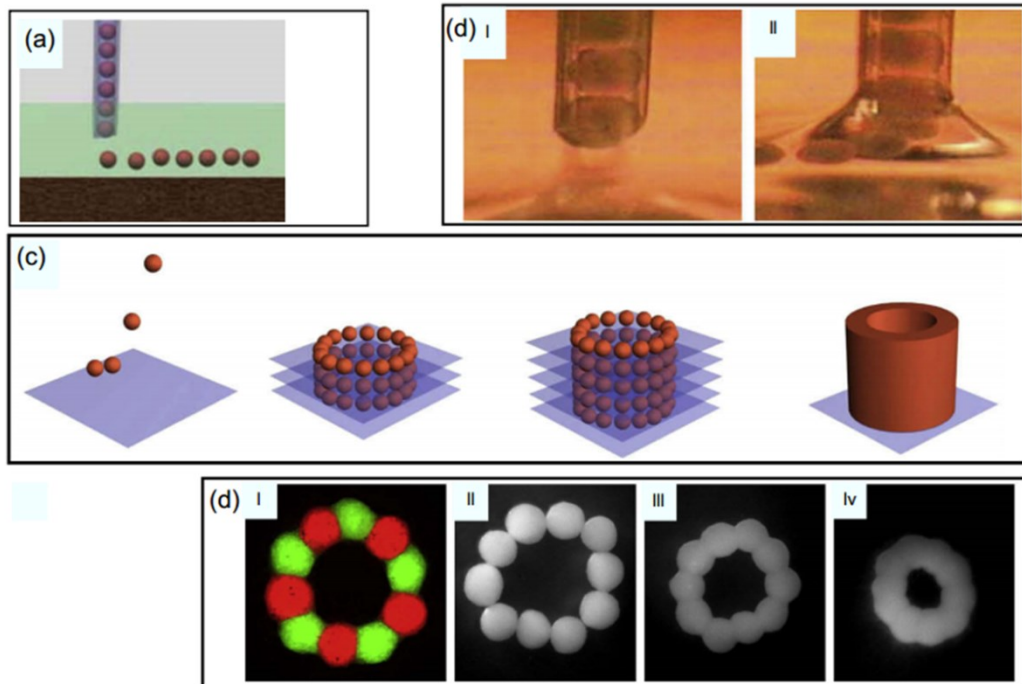


**Figure 1 Spheroid based tissue printing; Diagram of digital dispensing of spheroids in fluids (a); Tissue spheroids in loaded micro-pipette before dispensing (bi) and during (bii); Scheme for the bio-assembly of tubular tissue construct (c); Assembled ring like structure and tissue fusion process Labeled spheroids showing absence of cell mixing during the fusion process (di). Sequential steps during tissue fusion process (dii) adapted from [18].**

or cell-laden micro scaffold technology [13]. Different kinds of micromodules can be then arranged in a defined spatial arrangement, and their fusion led to the formation of a 3D structure resembling the modular nature of the native tissues [18]. For instances, by positioning in a defined spatial coordinates cellular spheroids made by smooth muscle cells and endothelial cells respectively, it has been obtained a 3D toroidal-shaped

biological structures, resembling the organization of a blood vessel [20]. Cellular spheroids can be easily printed and organized in a 3D arrangement with a high spatial resolution but due to the absence of an ECM, the cells in the final 3D tissue are mainly engaged in cell-cell interactions.

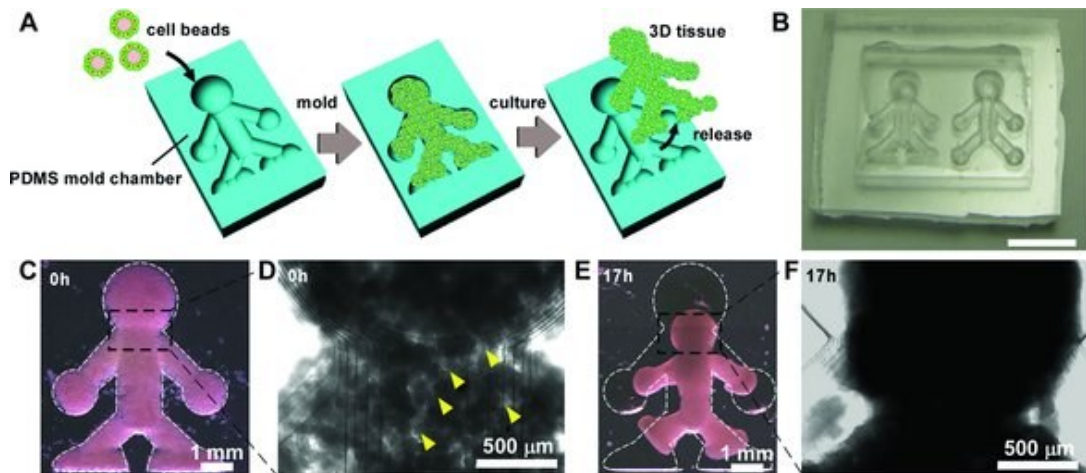


**Figure 2** Formation of millimeter-scale 3D tissue architectures by molding monodisperse cell beads. Method used to produce the 3D tissue architectures using monodisperse cell beads (a); A microscopy image of the doll-shaped PDMS mold chamber reveals 3D tissue formation (b); Microscopy images of NIH 3T3 cell beads immediately after stacking (c,d). Cavities (indicated with yellow arrows) among the cell beads are observed at this time point (0 h). Microscopy images of NIH 3T3 cell beads, 17 h after stacking (e,f). Adapted from [18]

Collagen gel in the form of bead, wire, or plug has been used to realize tissues micromodules populated by fibroblasts, neurons [7, 13, 21], or by co-culturing cardiac cells and endothelial cells [6]. Once packed, such micromodules were able to fuse and to generate macroscopic monotypic or heterotypic tissue-like structures. Microgel of complex shapes have been also fabricated by stereolithography and photopolymerization generating micromodules made by cell-seeded poly(ethylene glycol) microgels

organized in “key and lock” fashion. In the systems described so far, the mechanism that led to the fusion of the tissue micromodules comprised mainly cell-cell contacts, or microgel-microgel interactions occurring *via* multiphase liquid-liquid [22] interactions or *in situ* post polymerization [23]. Although the obtained 3D structures recapitulate the architecture of the native tissues, an assemblage of cells or cell embedded in exogenous biopolymers mainly composed them. Many studies report the role that the ECM plays in both *in vivo* and *in vitro* [24-26]. The response of a living tissue to any perturbations is mediated by the cross-talk existing among cells and their own ECM [27]. In parallel, different works, investigating on the role of the ECM composition *in vitro*, demonstrated that as the composition of the exogenous matrices approached that of the native tissues, the corresponding engineered tissues had more reliable response to external stimuli [28-30]. Bio-printing is an innovative technology that allows for the generation of organized 3D tissue constructs deposition process of cells seeded microcarries [31]. A crucial aspect of bio-printing is that the printing process must be cytocompatible [32]; bioinks are critical components in biofabrication, as they should possess the right rheological parameters required for the printing process and simultaneously offer an optimal environment for cell survival, proliferation, migration and biosynthetic activity [32]. The bio-ink can be molded into a designed silicone chamber to form the macroscopic 3D tissue structures; finally, the

fabricated tissue can be released from the mold, preserving the desired shape [33]. The advantages of this method are that we can: i) prevent tissue necrosis during tissue formation; ii) reconstruct 3D tissues with uniform cell density because the cell density of each cell bead can be tuned; and iii) easily overcoming tissue shapes to achieve geometrical control of the final printed tissue. In this chapter we show a new class of bio-ink, able to print tissues with endogenous ECM. We focused our attention regards the evolution of the bio-ink during the time, and how its “age” can influence the final characteristics of the printed tissue in terms of fusion capability, metabolic activities, collagen synthesis stiffness and distribution.

## **1.2 Material and methods**

### **1.2.1 Microscaffold production**

Gelatin porous microbeads (GPMs) have been prepared according to a modified double emulsion technique (O/W/O). Gelatin (type B Sigma Aldrich Chemical Company, Bloom 225, Mw=1 76654 Dalton) was dissolved into 10 ml of water containing TWEEN 85 (6% w/v) (Sigma Aldrich Chemical Company). The solution was kept at 40°C. Toluene containing SPAN 85 (3% w/v) (Sigma Aldrich Chemical Company) was continuously added to

the aqueous gelatin solution (8% w/v) to obtain primary oil in water emulsion. Beads of gelatin containing droplets of toluene were produced through the addition of excess toluene (30 ml) that allowed for a double emulsion (O/W/O). The resulting microspheres were filtered and washed with acetone and then dried at room temperature. Microspheres were separated selectively by using commercial sieves (Sieves IG/3-EXP, Retsch, Germany). GPMs with 75-150  $\mu\text{m}$  size range were recovered and further processed. GPMs have been stabilized by means of chemical treatment with glyceraldehyde (GAL), in order to make them stable in aqueous environment at body temperature. In particular, GPMs were dispersed into an acetone/water solution containing 4% of GAL and mixed at 4°C for 24 h. Then microspheres were filtered and washed with acetone and dried at room temperature. Before their use in cell culture dry GPM were sterilized by absolute ethanol sub-immersion for 24h. After that, in order to remove ethanol completely, several washings in calcium-free and magnesium-free phosphate-buffered saline (PBS) were performed. Before cell seeding PBS was removed and replaced with the culture medium.

## **1.2.2 Cell expansion**

Human dermal fibroblasts (neonatal HDF 106-05n ECACC) were sub-cultured onto 150 mm<sup>2</sup> Petri dishes in culture medium (Eagle's BSS Minimum Essential Medium containing 20% fetal bovine serum, 100 µg/mL L-glutamine, 100 U/mL penicillin/streptomycin, and 0,1 mM Non Essential Amino Acids). Cells were maintained at 37°C in humidified atmosphere containing 5% CO<sub>2</sub>. HDF of passages 4-7 were used.

## **1.2.3 Bio-ink engineering**

### **HD-µTP culture**

To realize the HD-µTP, spinner flask bioreactor was inoculated with 10<sup>5</sup> cell\*ml<sup>-1</sup> and 2mg\*ml<sup>-1</sup> of microbeads, corresponding to an initial ratio of 10 cells per bead. The culture suspension was stirred intermittently at 30 rpm (5 min stirring and 30 min static incubation) for the first 6h post-inoculation to allow adhesion, and then continuously stirred at 30 rpm up to 28 days. The growth medium was replenished on the first day and every 2 days until the end of experiments. From the day 4, 50 µg/ml of ascorbic acid (l-ascorbic acid Sigma A-5960) were added and freshly added at each medium change.

## **Cell proliferation on HD- $\mu$ TP**

At culture day 1, 3, 7, 14, 21 and 28, aliquots of 1ml were collected from spinner culture. Then, 3 aliquots of 300  $\mu$ l each was transferred to a cell culture dish (w/2 mm grid Nunc) and the number of HD- $\mu$ TPs were counted by visual inspection under microscope. After that, the each microcarriers suspension was placed in the 1,5ml eppendorf tube, gently washed twice with PBS, and then treated with trypsin solution (Lonza 17-161E 37°C 5 min) to allow cell detachment and harvesting. Finally, the detached cells were counted using an hemocytometer and the cell per HD- $\mu$ TP ratio was evaluated.

### **1.2.4 HD- $\mu$ TP morphology**

#### **Immunofluorescence and mutiphoton imaging**

Aliquot of 1 ml aliquots were collected at day 1, 3, 7, 14, 21 and 28 from the spinner culture and the HD- $\mu$ TP were stained with phalloidin tetramethylrhodamine B isothiocyanate (Sigma-Aldrich) and SYTOX® Green (INVITROGEN) for cell cytoskeleton and cell nuclei detecting respectively. Briefly, for both analyses, the HD- $\mu$ TP were fixed with 4% paraformaldehyde for 20 min at room temperature, rinsed twice with PBS buffer, and incubated with PBS-BSA 0.5% to block unspecific binding. In

particular the samples were incubated with SYTOX® Green stock solution (10 mg/mL in dimethyl sulfoxide) diluted in PBS (1/500 v/v) for 10 min at 37°C, and after rinsing in PBS, they were stained with phalloidin for 30 min at room temperature. After that, the stained HD- $\mu$ TP were imaged under multichanneled Leica TCS SP5 II coupled with a Multiphoton Microscope where the NIR femtosecond laser beam was derived from a tunable compact mode-locked titanium: sapphire laser (Chameleon Compact OPO-Vis, Coherent). Two channels were used for confocal imaging of cell nuclei ( $\lambda_{\text{ex}} = 500 \text{ nm} / \lambda_{\text{em}} = 520\text{-}530 \text{ nm}$ ) and cytoskeleton ( $\lambda_{\text{ex}} = 573 \text{ nm} / \lambda_{\text{em}} = 588\text{-}598 \text{ nm}$ ) respectively. Two-photon excited fluorescence ( $\lambda_{\text{ex}} = 840 \text{ nm}$ ) was used in another channel to induce second harmonic generation (SHG) of unstained neo-synthesized collagen structures by collecting the emission wavelength in the range  $\lambda_{\text{em}} = 420 \pm 5 \text{ nm}$ .

## **Histology**

For histological analysis, 1 ml of HD- $\mu$ TP suspension was fixed in a solution of 10% neutral buffered formalin for 24 h, dehydrated in an incremental series of alcohol (75%, 85%, 95% and 100%, and 100% again, each step 20 min at room temperature) treated with xylene and then embedded in paraffin. Successively, the samples were sectioned at a thickness of 6 $\mu$ m, and stained with hematoxylin and eosin. The sections were mounted with

Histomount Mounting Solution (INVITROGEN) on coverslips and the morphological features of constructs were observed with a light microscope (Olympus, BX53).

## **1.2.5 Dynamic interaction among HD- $\mu$ TPs**

### **HD- $\mu$ TP Aggregation**

To evaluate the aggregation capability, aliquots of HD- $\mu$ TP were collected at each time point (days 3, 7, 14, 21 and 28), and placed under microscope (Olympus CK X41). The acquired images were processed by using imageJ software: after transforming in binary images thresholding,, by means analyze particles plugin it was measured the area distribution of the HD- $\mu$ TP. 100 HD- $\mu$ TPs were analyzed at each time point . Data were reported as mean value $\pm$ SD.

### **Multi particles tracking**

Custom made multiple particle tracking microrheology apparatus was used to probe the local mechanics of the neo-synthesized ECM macromolecule on the surface of the HD- $\mu$ TP by monitoring and tracking the motion of particles embedded in the samples. Fluorescent polystyrene particles (100 nm Polyscience) were shot on the HD- $\mu$ TPs using a ballistic gun (Bio-Rad, Hercules, CA). Helium gas at 2200 psi was used to force a macrocarrier

disk coated with particles to crash into a stopping screen. The force of collision was transferred to the particles, causing their dissociation from the macrocarrier and the bombardment of HD- $\mu$ TPs. Then, the samples were placed in a microscope stage-incubator at controlled temperature and CO<sub>2</sub> (37 °C and 5%, respectively). Movies of embedded particles were recorded via a gated intensified high-speed camera (Lambert Instruments, Roden, The Netherlands) mounted on an inverted epifluorescence microscope (Olympus IX70, Olympus, Melville, NY) at 100x magnification. The displacements of particle centroids were monitored by a time-lapse acquisition of 6 s at a rate of 50 frames per second. Movies of particles were analyzed by a ourself-developed algorithm in Matlab (Matlab 6). It detects each position in every frame by intensity measurements and links this point detection into trajectories, basing on the principle that the closest positions in successive frames belong to the same particle (proximity principle). Once obtained the trajectories, mean square displacements (MSD) described by the equation 1:

$$\langle \Delta r^2(\tau) \rangle = \langle [x(t - \tau) - x(t)]^2 + [y(t - \tau) - y(t)]^2 \rangle \quad (1)$$

was obtained. In the equation 1  $\langle \rangle$  means time average,  $\tau$  is the time scale and  $t$  the elapsed time.

The MSD provide information about the mechanical properties of intracellular and extracellular environments. Indeed, it was demonstrated that the MSD amplitude is inversely related to the rheological properties of living cells [34]. Here we compared MSD to have information about the evolution of structural and mechanical organization of ECM deposited and assembled on surfaces of the HD- $\mu$ TP during the culture period.

### **1.2.6 collagen fraction quantification**

SHG images from HD- $\mu$ TP were analyzed by using imagej software in order to quantify the collagen fraction. The portion of the HD- $\mu$ TP not occupied by the microscaffolds was considered as the space occupied by the newly synthesized ECM (ECM space). The ECM space was divided in collagen portion and non-collagen portion. The former appears as bright pixel due to SHG signal, the latter as dark pixel. We define “collagen fraction” the ratio between bright pixels to total pixels (dark plus gray)-

### **1.2.7 Oxygen consumption kinetics measurements**

In order to evaluate the oxygen consumption kinetics of the HD- $\mu$ TP along culture time (days 0, 3, 7, 14, 21, 28) a small amount of microtissues were spilled from the spinner flask at each time point and placed in 3 different vials of frosted glass. The vials were filled with fresh culture medium and

then placed in an incubator and kept at 37°C, under gentle agitation. The vials were then closed in order to avoid oxygen exchange with the surrounding environment. By means of an optical detector (OXY-4 PreSens) it was measured the oxygen concentration of the medium in the vials. The partial pressure was converted in oxygen concentration (C) by means of Henry's law ( $5 \cdot 10^{-4}$  atm/ molar fraction). As control the same measurements were performed in three vials containing only medium and maintained in the same conditions. At the end of the experiment the HD- $\mu$ TP were enzymatically treated and the cell number was counted in order to obtain cell density in the medium ( $\rho$ ). By performing centered time derivative of the oxygen concentration curve, is possible to obtain the consumption velocity (V). By plotting V vs C a Michelis-Menten law kinetic is obtained. In order to evaluate the kinetics parameters, a linearization of the kinetics curve was performed by plotting  $V^{-1}$  and  $C^{-1}$ ; the intercept with y axis is  $V_{\max}^{-1}$ , and the intercept of x axis is  $-K_m^{-1}$

## **1.2.8 Realization and characterization of 3D tissue**

### **HD- $\mu$ TP packing and culturing.**

HD- $\mu$ TP suspension was transferred from the spinner flask to the a maturation chamber and casted in cylindrically shaped mold 1 mm in thickness and 5 mm in diameter. The maturation chamber was kept under

controlled dynamic culture conditions to allow bio-fusion of the HD- $\mu$ TPs as previously described. The maturation process had a duration of 2 week generating 3D-Tissue having the dimension of the initial cylindrical mould. This procedure was repeated at each time point of the HD- $\mu$ TP culture (days 3, 7, 14, 21 and 28) in order to have 3D-Tissues generated by HD- $\mu$ TP having different properties and age.

### **Evaluation of the newly-formed collagen assembling kinetics**

After two weeks of culture maturation chamber was opened and the 3D-Tissues were fixed in a solution of 10% neutral buffered formalin for 24 h. After the fixation and dehydration procedure the 3D-Tissues was embedded in paraffin to be sectioned transversally to the circular surface. In order to characterize the ECM morphology and composition, histological analysis on transverse sections of biohybrid, was performed along the biohybrid's thickness. Transverse sections 7 $\mu$ m thick, were stained using Masson's trichrome (Sigma Aldrich) and Picro Sirius Red (Sigma Aldrich) following standard procedure and analyzed by an optical microscope (BX53; Olympus). The samples stained with Picro Sirius red were observed by using a polarized microscope. Polarized light images of samples stained with Picrosirius Red alone were acquired with an inverted microscope (BX53; Olympus) with a digital camera (Olympus DP 21). A linear polarizer

was placed between the light source and the specimen, while the analyzer was installed in the light path between the specimen and the camera. The color of collagen fibers stained with picosirius red and viewed with polarized light depends upon fiber thickness; as fiber thickness increases, the color changes from green to red [35, 36]. To quantitatively determine the proportion of different colored collagen fibers, we resolved each image into its hue, saturation and value (HSV) components by applying the software's "color threshold" function. Only the hue component was retained and a histogram of hue frequency was obtained from the resolved 8-bit hue images, which contain 256 colors. We used the following hue definitions; red 0-51, green 52-120. The number of pixels within each hue range was determined and expressed as a percentage of the total number of collagen pixels, which in turn was expressed as a percentage of the total number of pixels in the image. Since the aim of imaging analysis was to investigate the evolution of endogenous ECM composition, it was necessary to exclude by region of interest (ROI) the areas occupied by the microsc scaffold when it was still present.

### **Evaluation of the newly-formed collagen distribution**

The degree of assembling of collagen network was evaluated by analyzing the intensity of SHG signal [37, 38]. The analysis was performed within the

3D-Tissue space, where the SHG was present, by distinguishing two different zone: i)  $\mu$ TP-bulk, indicating the newly deposited collagen within the HD- $\mu$ TP space; (ii)  $\mu$ TP-interstices indicating the newly deposited collagen between the HD- $\mu$ TP interstices. All SHG images were subjected to noise subtraction and the average intensity in the two different zones was evaluated as described by the equation 2:

$$\bar{I} = \frac{\sum_{i=1}^{255} I_i p_i}{\sum_{i=1}^{255} p_i} \quad (2)$$

where:  $\bar{I}$  is the average intensity,  $I_i$  is the intensity corresponding to the  $P_i$  pixel while the index  $i$  runs in the gray value interval: from 1 (less intensity) to 255 (more intensity). The intensity is proportional to the degree of assembly of the newly synthesized collagen [37, 38].

### 1.2.9 Engineered bio-ink printing

“Symbolic” mold for “symbolic” printed shape were carved onto a Poly(methyl methacrylate) (PMMA, Goodfellow) using micromilling machine (Minitech CNC Mini-Mill). Four shapse were realized: triangle, cross, circle, square (1mm in thickness, 2 mm in width and 4 mm in length for each side

and circle diameter). In order to obtain a uniform distribution of the bio-ink during the printing process, the HD- $\mu$ tps were loaded glass Pasteur to guarantee the alignment of the HD- $\mu$ tps; the Pasteur was connected to a syringe pump in order to have a constant flow rate and a consequent uniform spill of the HD- $\mu$ tps. During the filling procedure the “symbolic” mold were accommodated on a moving stage to guarantee X and Y moving, and connected with a vacuum pump to assure that no bubbles were in maturation space. Completed the printing process the “symbolic” mold were placed on the bottom of a spinner flask and completely surrounded of culture medium for two weeks. The spinners was operated at 60rpm and the medium was exchanged every three days. The maturation lasted 2 weeks.

### **1.2.10 Characterization of symbolic shape**

Using optimized bio-ink (14 days), same symbolic shape were printed; line shape (1 mm in thickness, 2 mm in width and 9 mm in length); Geometrical shapes (1mm in thickness, 2 mm in width and 4 mm in length for each side and circle diameter). All the symbolic shapes were stained with SYTOX® Green (INVITROGEN) for cell nuclei detecting. Briefly, the printed tissues were fixed with 4% paraformaldehyde for 20 min at room temperature, rinsed twice with PBS buffer, and incubated with PBS-BSA 0.5% to block

unspecific binding. In particular the samples were incubated with SYTOX® Green stock solution (10 mg/mL in dimethyl sulfoxide) diluted in PBS (1/500 v/v) for 10 min at 37°C, and after rinsing in PBS. The printed tissue were imaged under multichanneled Leica TCS SP5 II coupled with a Multiphoton Microscope where the NIR femtosecond laser beam was derived from a tunable compact mode-locked titanium: sapphire laser (Chameleon Compact OPO-Vis, Coherent). Two-photon excited fluorescence ( $\lambda_{\text{ex}} = 840\text{nm}$ ) was used to induce second harmonic generation (SHG) of unstained neo-synthesized collagen structures by collecting the emission wavelength in the range  $\lambda_{\text{em}} = 420\pm 5\text{ nm}$ . The second channel was used for confocal imaging of cell nuclei ( $\lambda_{\text{ex}} = 504\text{ nm} / \lambda_{\text{em}} = 520\text{-}530\text{ nm}$ ). The third channel was set to visualize the elastin auto-fluorescent signal ( $\lambda_{\text{ex}} = 740\text{ nm} / \lambda_{\text{em}} = 480\text{-}600\text{ nm}$ ).

## **1.3 Results**

### **1.3.1 $\mu$ TP Evolution: cell proliferation aggregation and remodeling**

The  $\mu$ tps evolution during 28 days were evaluated, in figure 14 are reported the time evolution of cells and ECM organization. At day 3-7 of spinner culture, the cells colonized mainly the external surface of the microbeads

(a-b), while during third and fourth week, cells invasion and ECM synthesis occurred also in the bulk of the HD- $\mu$ TP forming a micrometric tissues completely made-up of cell embedded in their own ECM (c-d). The number of cells per  $\mu$ tp grows exponentially during two first weeks, starting from 10 cells per microbeads until to  $2 \cdot 10^3$  cells per microtissue; moreover between 14th and 28th day the duplication rate drastically decrease and no statistical difference were detected.

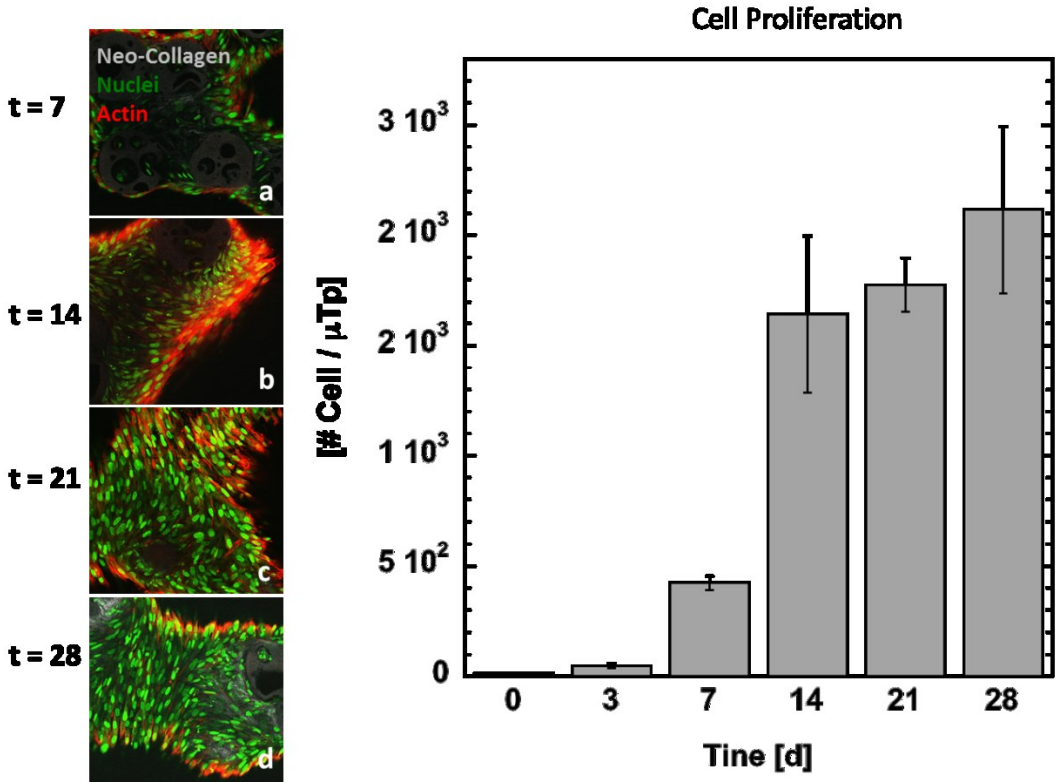


Figure 3  $\mu$ tp evolution during culture time: nuclei ad actina distribution (a-d) and growth curve

The figure 4 shows the aggregation capability of the  $\mu$ tps in dynamic condition (a-d); the graph quantifies the areas evolution, the value start from  $5 \cdot 10^4 \mu\text{m}^2$  and increase of four time until  $2 \cdot 10^5 \mu\text{m}^2$  in correspondence of two weeks. Starting from third week the  $\mu$ tps lose this intrinsic characteristic, and the values of the areas decrease. This trend is due to the contribution of two several factors: contraction, and less of fusion capability. During the early time point the contribution of the fusion overbear the contraction, while later of two weeks the contraction itself exceeded the micro tissues fusion. The value of MSD at  $\tau=1$  s was reported. MSD analyses showed that there was a significant reduction of distance traveled by particles from day 7 to day 14, and a successive stabilization of MSD value until day 28. In active systems, such as HD- $\mu$ TPs, in which remodeling processes of both cytoskeleton and ECM network, the violation of generalized Stokes-Einstein equation prevents the direct correlation between MSDs and viscoelastic moduli. Nevertheless, it was demonstrated that also when active processes are present, the MSD amplitude is inversely proportional to the stiffness of explored microenvironment [34]. Thus, we suggest that the reduced motion of particles observed at 14 days is associated to an increased structuration and stiffening of cytoskeleton and more abundant and organized extracellular matrix.

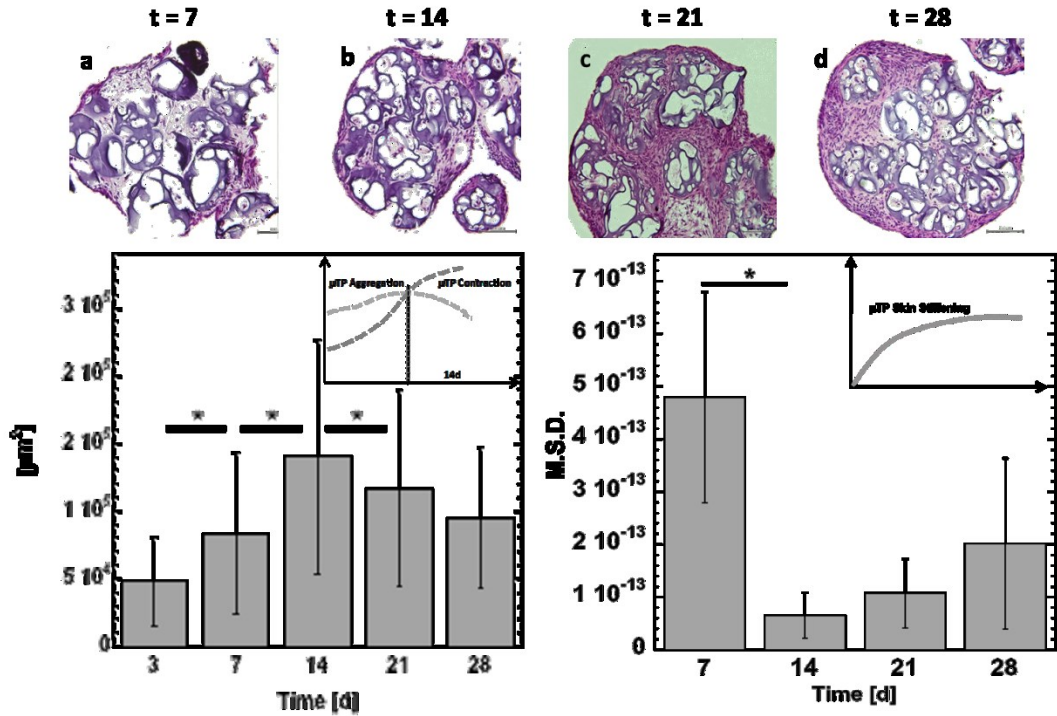


Figure 4  $\mu$ tp evolution during culture time: H/E staining, scale bar 200  $\mu$ m (a-d); aggregation and diffusion coefficient

### 1.3.2 $\mu$ TP Evolution: metabolic and biosynthetic activity

The cells are embedded in own extracellular matrix, that evolves and changes the characteristics of the final tissue. Figure 5 shows the collagen evolution during culture time (a-d), the graph of collagen fraction shows an increase of collagen I and III signals inside the extracellular matrix; the signal at 3th day (picture not shown) isn't detectable, the percent of collagen increase from 7th day to 14<sup>th</sup> day of more than ten times and reaches a plateau value of about 50% for all other time points. The oxygen

rate consumption, describe the demand of nutrients related with  $\mu$ tps age; in the first time point was measured the maximum value of  $2.1 \cdot 10^{-8}$ , two time highest of 7 days point. Just from 2 weeks the initial value let down of an order of magnitude, value confirmed at three and four weeks; this parabolic trend, concerning the collagen evolution, show two several phases of the cellular activity: biosynthetic phase (3-7 day) and maturation phase (14-21-28 days). During the biosynthetic phase the cells are engaged to synthesize new collagen, while during the maturation phase the cells reassemble the collagen previously synthesized in reticulate collagen.

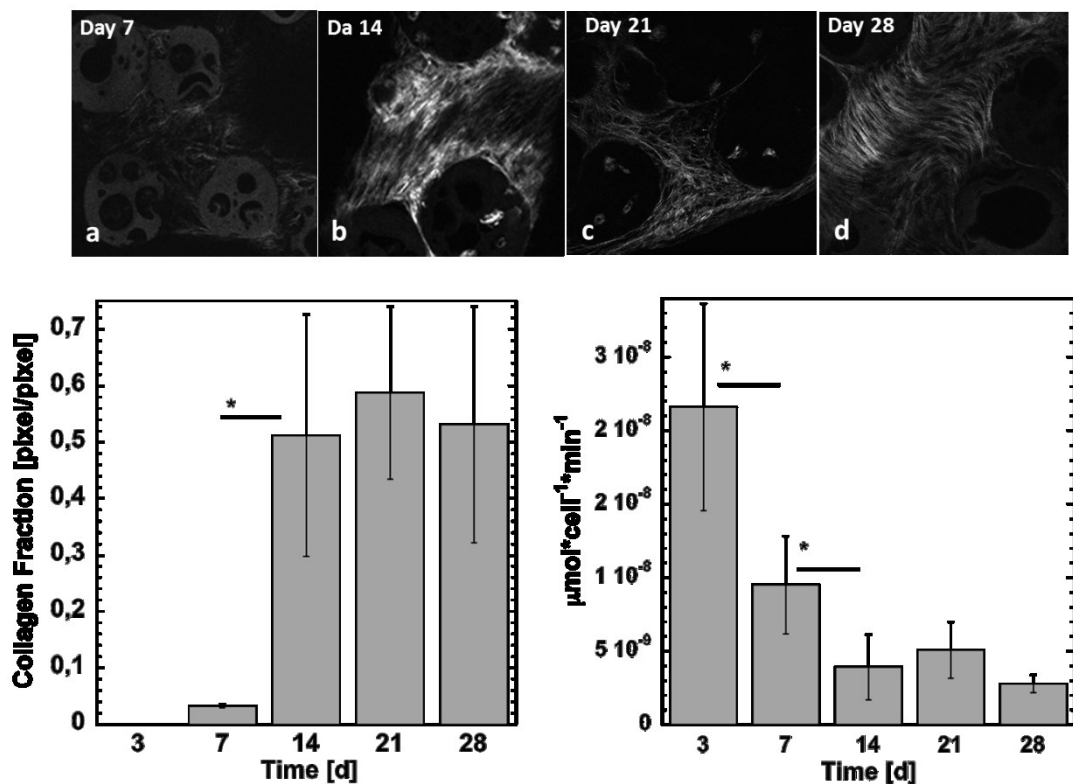


Figure 5  $\mu$ tp collagen evolution (a-d) and quantification; maximum oxygen rate consumption.

### 1.3.3 $\mu$ TP age on final 3D tissue printed

The final 3D characteristics changes in relationship to  $\mu$ tps age, in terms of collagen fraction, architecture and distribution. The biohybrids, build up starting from several  $\mu$ tps age, show a compact structure in all cases, as shown from trichrome masson ( figure 6 a-e). The picrosirius red (figure 6 f-l) demonstrate a consistently variation in terms of architecture and distribution of the ECM; in particular until 14<sup>th</sup> day the resultants biohybrids are characterized from an uniform ECM structure, whereas the final 3D build up whit 21<sup>th</sup> 28<sup>th</sup> days  $\mu$ tps appear a discontinuity inside the interstices amongst  $\mu$ tps themselves, clear evidence of the incapacity of the long time  $\mu$ tps to close the gap in the ECM between singles  $\mu$ tps. The fraction of immature collagen shows the capability of the  $\mu$ tps to synthetize new collagen in bioibrids realized starting from  $\mu$ tp of 14 days, the value during the first two weeks increase of four times; in the next time point the value decrease until 1.2%. Though the collagen of mature fraction increase growth of ten times during culture time, the lowest value of immature collagen elucidate why the gaps aren't covered.

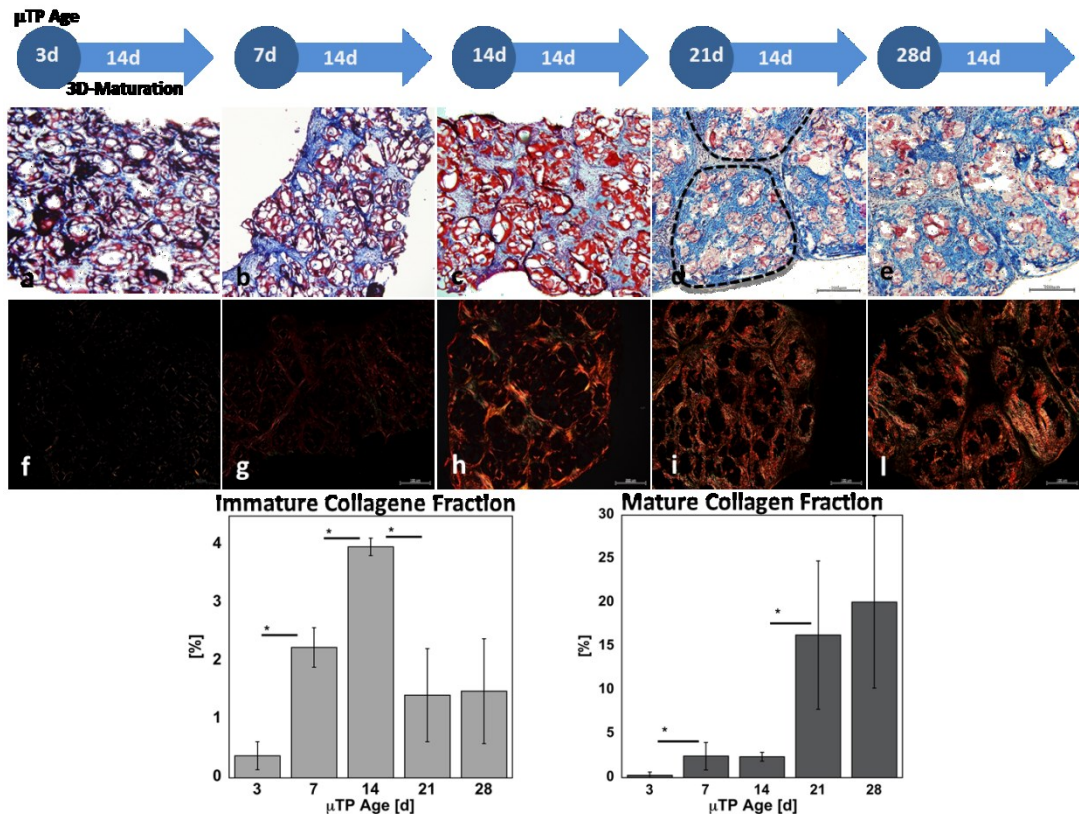


Figure 6 effects of  $\mu$ tp age on the final 3D printed tissue; masson trichrome (a-e), picrosirius red (f-l), immature and mature collagen quantification; scale bar 200  $\mu$ m

### 1.3.4 Collagen distribution in the 3D printed tissue

Figure 7 shows SHG collagen signals (a-e) inside the 3D printed tissues. This kind of signal confirm the results of figure 6 in which is possible to note the formation of the discontinuity zones inside the ECM. The graph shows the intensity of the collagen signal, inside the and between the  $\mu$ tps. The collagen concentration inside the  $\mu$ tps get on during the second week starting from a value of 10 pixel/pixel to 30 pixel/pixel and it fluctuates

around maximum value for the three weeks more. The characterization of the collagen in the interstice show an increasing trend until 14<sup>th</sup> day, in which the value is 15 pixel/pixel, and a decrease in the next weeks where it back to the initial values of 8-10 pixel/pixel. This evidence shows an incapability of the 21<sup>th</sup> and 28<sup>th</sup> days  $\mu$ tps to bridging the gap during the fusion process.

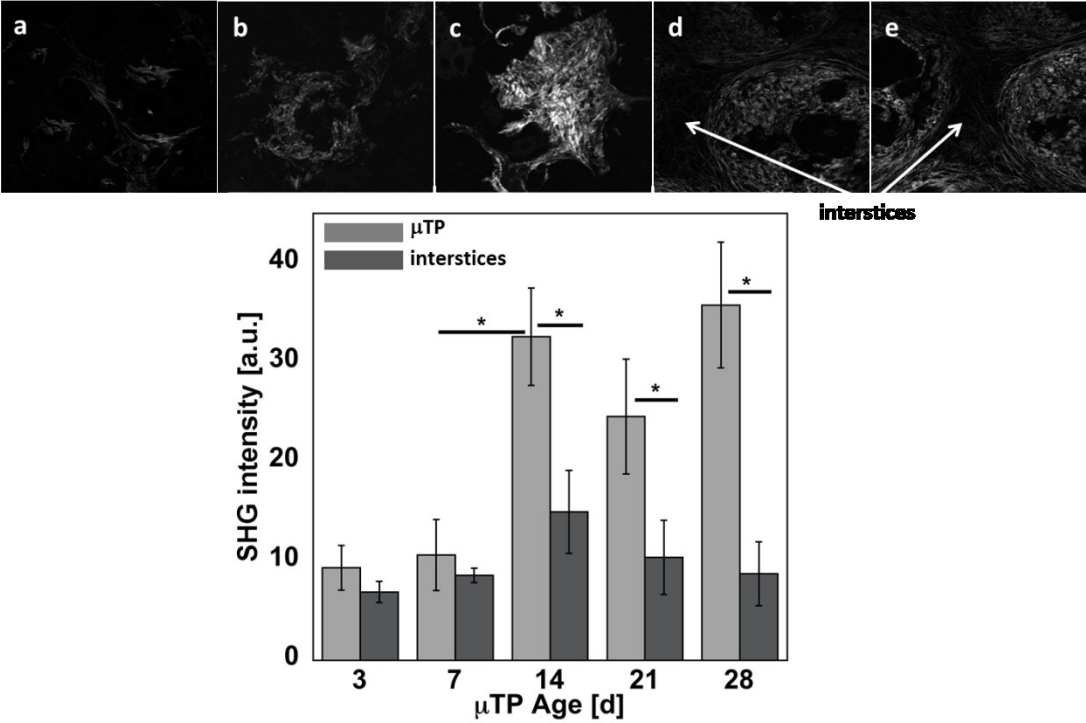


Figure 7 collagen distribution (a-e) acquired by second harmonic generation in the 3D printed tissue, and quantification

### **1.3.5 Characterization of symbolic shape**

The image 8 shows the printed tissue with “symbolic” shape as above described, by using this technique is possible to overcoming the shape limits. The fluorescent signal display an homogenous cells distribution without discontinuity zone. Furthermore the SHG reconstruction shows that the final result is a complete tissue composed by cells and own extra cellular matrix, with collagen and elastin, and not only a macro-metric cellular aggregate.

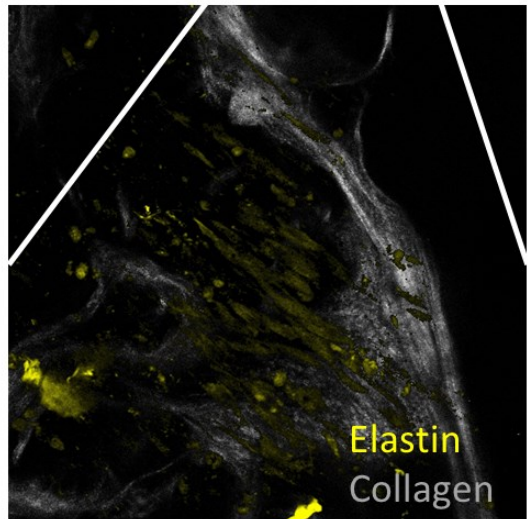
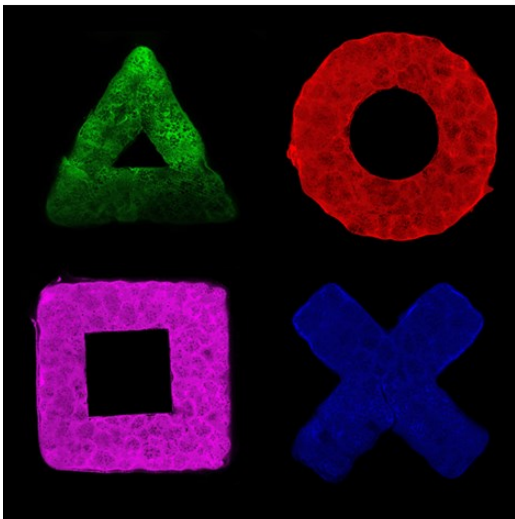
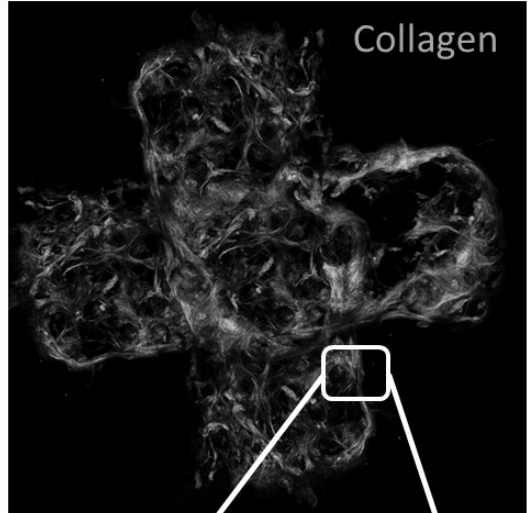


Figure 8 Symbolic printed shape; nuclei staining, collagen and elastin MP excitation.

## 1.4 Discussion

Tissue and organ functions are strongly regulated by the cross talk between cells and its own ECM [39]. As a consequence engineered tissues, that aims to be an *in vitro* functional replica of the corresponding native one, must reproduce the dynamic environment in which the cells are naturally embedded. In this scenario, we realized engineered functional tissue micromodules for *in vitro* bio-printing applications, which provide the fabrication of endogenous 3D tissue equivalents in different shapes. HD- $\mu$ TP were obtained by culturing human fibroblast within custom made gelatin porous microbeads [7, 13]. Microcarriers made of native polymers such collagen and gelatin representing a good choice in supporting the proliferation of anchorage dependent cells through favorable cell-matrix interactions [40, 41], the cell cultured in porous microcarriers, could be addressed in synthesizing their own ECM, generating endogenous microtissues that worked as micromodules (or bio-ink) for bottom-up tissue engineering [7, 13]. In general tissue micromodules are commonly designed with regard to its initial cell density, shape [6], size distribution [42], capability to induce stem cell differentiation [43] and fusion mechanisms [44]. All this parameters have been shown to affect the final 3D tissue in terms of cell distribution and viability, furnishing partial evidences concerning 3D tissue formation in terms of ECM production and

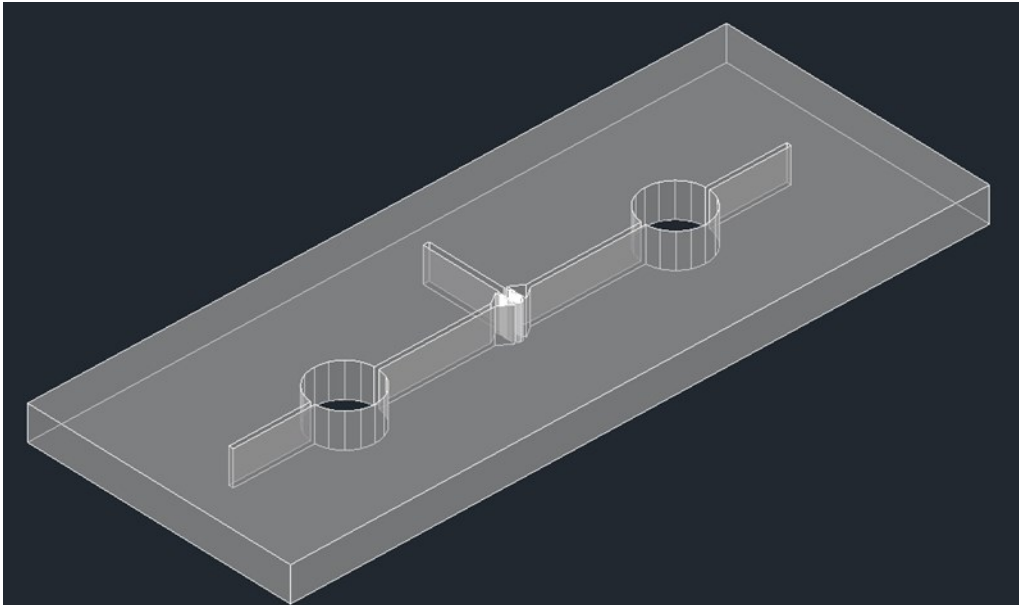
organization. During the dynamic culture cell density per HD- $\mu$ TP increased reaching a plateau at day 14 in agreement with similar studies [13]. The SHG signal detected from day 7 to day 28, indicated that cells within the HD- $\mu$ TP were engaged in the collagen production and assembling. The HD- $\mu$ TP were surrounded by a rim of tissue that induced their aggregation via cell-cell and ECM-ECM contact, as demonstrated by the increasing of the average area occurring until day 14. On the other hand, starting from day 14, HD- $\mu$ TP started to shrink. In this time frame the contraction induced by the cell traction, was the predominant process with regard to the fusion capability, leading to a reduction of the average size of the HD- $\mu$ TP. The depression of fusion capability was ascribed to the stiffening of the ECM on the surface of the HD- $\mu$ TP depressing the HD- $\mu$ TP fusion capability. Indeed, the HD- $\mu$ TP fusion was a process mediated by both cell-cell-cell and ECM-ECM interaction. The growing collagen polymeric network, worked as glue between adjacent HD- $\mu$ TP and the reduced mobility of the collagen network, detected by the MPT analyses, indicated that its “sticking” capability decreased as culture time increased. Along the culture time we observed that HD- $\mu$ TP manifested two different biological regimes. From day 3 to day 14 (biosynthetic phase), cell density and collagen amount increased, then they remained constant from day 14 to day 28 (maturation phase). During the biosynthetic phase the cells were engaged in synthesise

new collagen and in concert, the metabolic request was higher than in the maturation phase. From day 14 till day 28, the cells number remained constant as well as the amount of collagen and cells were mainly devoted in assembling the collagen previously synthesized, lowering their metabolic request was. This was in agreement with other works reporting that cell depressed their metabolic request as the number of cell-ECM interaction increased [45]. In order to assess the role of HD- $\mu$ TP properties on the final 3D tissue we fabricated 3D structures by using as bio-ink HD- $\mu$ TP from different days of culture. The histological section of the 3D tissues, revealed that regardless to HD- $\mu$ TP age, all macroscopic 3D printed tissues were viable, compact and newly formed ECM was present through the whole thickness. In contrast, 3D tissue obtained starting from cell-beads, cell-laden microgel and cell aggregates were mainly composed by cell embedded in exogenous biopolymers or cell spatially arranged in a 3D architecture [14]. In other scientific reports, it has been proved the realization of dermal-like structures by using cell-populated microbeads as bio-ink [21], although it was found a high density of viable cells along the tissue thickness, but no ECM were detected. PSR and SHG imaging allowed to elucidate that by using HD- $\mu$ TP from day 3, 7 and 14, the resultant 3D tissues were characterized by an uniform ECM structure, whereas the heterogeneity in 3D tissues was exacerbated when HD- $\mu$ TP

came from day 21 and day 28. This was due to HD- $\mu$ TP hyper-maturation at later culture time, resulting in less-communicating micromodules, in agreement with the reduced fusion capability observed in the suspension culture. The optimal bio-ink was the HD- $\mu$ TP at day 14 possessing the following features: (i) optimal size to be printed (150-200  $\mu$ m in diameter); (ii) higher fusion capability; (iii) lower oxygen request; (iv) uniform ECM maturation in the 3D tissues. The engineered HD- $\mu$ TP represents an innovative bio-ink to be used in modular tissue engineering proving that building-up 3D tissue formed by endogenous ECM is feasible. Because the presence of endogenous ECM it we propose a more reliable model than the cellular spheroids and cell-laden micromodules, HD- $\mu$ TP can be realized in starting from different cell lines and printed allowing the realization of different structures tissue that can be used in human body on chip applications.

## Chapter 2

Microfluidic device as screening system  
for 3D-tissue culture conditions



# Chapter 2

## 2.1 Introduction

The classical cells culture conditions do not closely mimic the *in vivo* microenvironment due to the absence of the fluid flow and shear stresses [46]. Also, these cultures are less suited to provide a dynamically controlled flow of cell nutrients and stimuli and, additionally, the accumulation of waste leads to a pH drift in a static culture [47]. Other drawbacks of the classical cell culture systems are the long growth times needed for cells to differentiate into functional cells and the dependence on external signal detection systems that require manual withdrawing and manipulation of samples [46]. Furthermore, crucial it becomes the choice of the bioreactor;

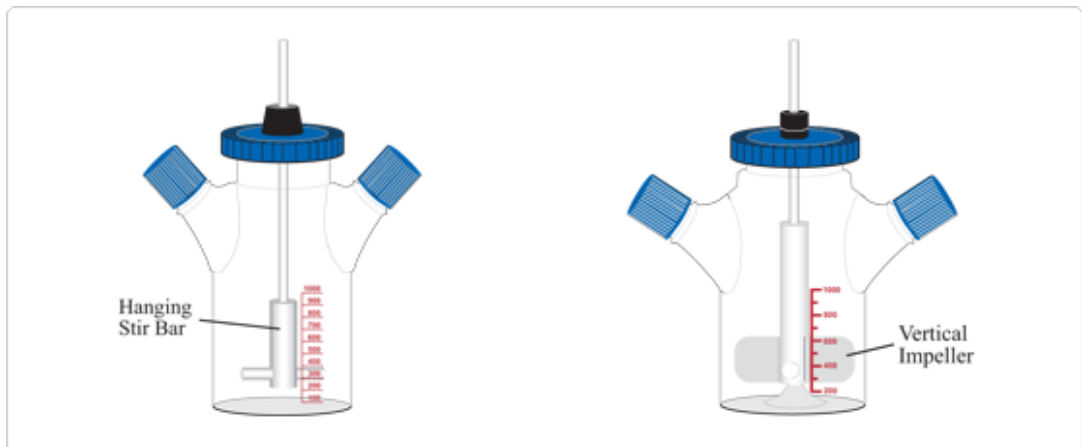


Figure 9 spinner flask bioreactor

One of the simplest bioreactor designs is the spinner flask (fig 9), the

convective forces generated by the magnetic stir bar mitigate the nutrient concentration gradients at the surface of the scaffolds [48, 49]. Spinner flasks have also been successfully used for seeding cells on scaffolds with well-controlled cell densities. Another kind of bioreactor that improves mass transfer at the interior of three-dimensional scaffolds is the flow perfusion bioreactor (fig 10).



**Figure 10** perfusion bioreactor

This type of bioreactor uses a pump to perfuse medium continuously through the interconnected porous network of the seeded scaffold [50-52]. The fluid path must be confined so as to ensure the flow path is through the scaffold, rather than around the edges. Bioreactors that employ the latter flow path, exchanging medium within the porous confines of the scaffold interior. The perfusion bioreactor offers enhanced transport of nutrients because it allows medium to be transported through the interconnected pores of the scaffolds [52]. The amount of shear stress experienced by cells cultured in a flow perfusion system can be varied simply by varying the flow rates through the system. The main drawbacks of this kind of bioreactors are related to the dimension; big size means great number of cells, great amount of products for cell culture, wide outdoor, and process expense. In order to overcoming this kind of problems, in research, micrometric device increasingly are spreading; microfluidic device are able to recreate the same conditions of the macroscopic bioreactor, by reducing trial times and costs. Great interest has focused on transferring various micro-physiological organ models, onto microfluidic platforms to enable better control over physical and biochemical factors in cell microenvironment [53, 54]. Recent developments in microfabrication and microfluidic technologies provided the tools to create advanced cell culture systems, aiming to provide *in vivo*-like cellular microenvironments (fig 11). The small culture volumes within these devices consume much less cells as well as culture and analytical reagents.

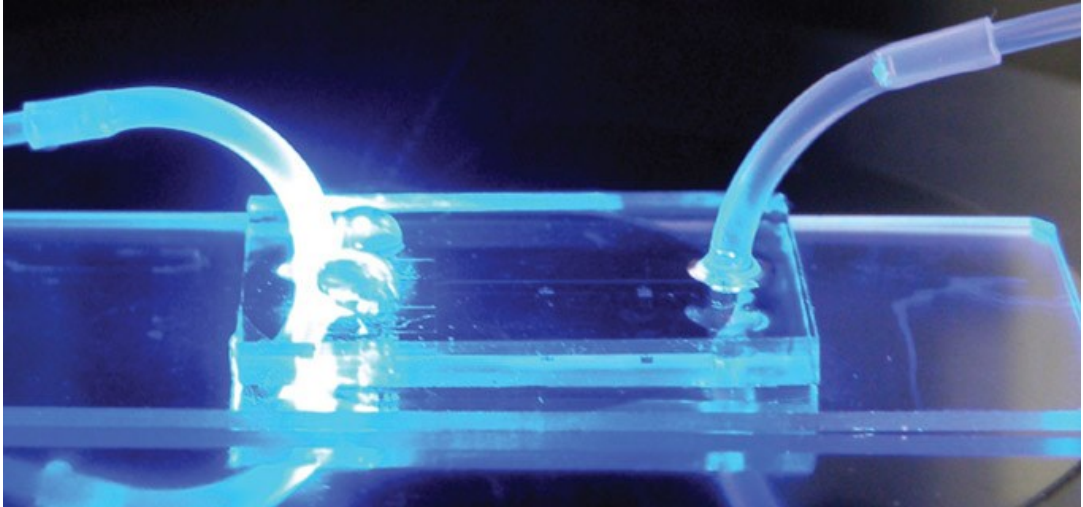


**Figure 11 microfluidic device**

They allow control of micro-environmental parameters, such as cell–cell and cell–matrix interactions [44, 53]. Additionally, the tissue-to-fluid ratio within these devices can be adjusted to mimic the physiological ratios [54]. Perfusion-based media supply allows delivery and removal of soluble molecules in the cell microenvironment and controlled application of shear stresses by the fluid flow [55]. A clear advantage of using organ-on-a-chip systems is the control of the fluid flow in physiologically-relevant dimensions, which makes it possible to regulate nutrient and drug concentrations at the level of single cells or small cell clusters [53]. Likewise, microfluidic perfusion culture allows novel experiments for controlling the microenvironment, which affects cellular phenotypes [47]. Laminar flow in microfluidic systems enables the controlled application of shear stress, and the delivery of multiple laminar streams of different

soluble molecules at the cellular or subcellular levels [56]. Conversely, microfluidic perfusion culture can effect a defined, artificial microenvironment by continuously controlling the supply and removal of soluble factors [56]. Such defined environments are unobtainable in static culture, where the background of soluble factors and nutrients changes constantly over time [57]. Furthermore, microfluidic perfusion culture allows the possibility of continuous non-recirculating culture that would be impractical at the macro-scale due to reagent volumes [58]. There is also a need for effective integration between microfluidic perfusion culture systems and ultrasensitive analytical micro-assays to enable higher-throughput extraction of the biological data required in many applications [56]. An understanding of the constraints imposed at each stage of performing microfluidic perfusion culture (e.g. microfluidic system fabrication, cell culture and assay) will enable one to design and operate a microfluidic perfusion culture system more effectively. In this work we realized a perfusion bioreactor on micrometric scale as tool to optimize culture condition; this model can be successfully used as “fast screening platform” in order to evaluate the each kind of stimulus-response in tissues.

## **2.2 Material and methods**

### **2.2.1 Microscaffold production**

Gelatin porous microbeads (GPMs) have been prepared according to a modified double emulsion technique (O/W/O). Gelatin (type B Sigma Aldrich Chemical Company, Bloom 225, Mw=1 76654 Dalton) was dissolved into 10 ml of water containing TWEEN 85 (6% w/v) (Sigma Aldrich Chemical Company). The solution was kept at 40°C. Toluene containing SPAN 85 (3% w/v) (Sigma Aldrich Chemical Company) was continuously added to the aqueous gelatin solution (8% w/v) to obtain primary oil in water emulsion. Beads of gelatin containing droplets of toluene were produced through the addition of excess toluene (30 ml) that allowed for a double emulsion (O/W/O). The resulting microspheres were filtered and washed with acetone and then dried at room temperature. Microspheres were separated selectively by using commercial sieves (Sieves IG/3-EXP, Retsch, Germany). GPMs with 75-150  $\mu\text{m}$  size range were recovered and further processed. GPMs have been stabilized by means of chemical treatment with glyceraldehyde (GAL), in order to make them stable in aqueous environment at body temperature. In particular, GPMs were dispersed into an acetone/water solution containing 4% of GAL and mixed at 4°C for 24 h. Then microspheres were filtered and washed with acetone

and dried at room temperature. Before their use in cell culture dry GPM were sterilized by absolute ethanol sub-immersion for 24h. After that, in order to remove ethanol completely, several washings in calcium-free and magnesium-free phosphate-buffered saline (PBS) were performed. Before cell seeding PBS was removed and replaced with the culture medium.

### **2.2.2 Cell expansion**

Human dermal fibroblasts (neonatal HDF 106-05n ECACC) were sub-cultured onto 150 mm<sup>2</sup> Petri dishes in culture medium (Eagle's BSS Minimum Essential Medium containing 20% fetal bovine serum, 100 µg/mL L-glutamine, 100 U/mL penicillin/streptomycin, and 0,1 mM Non Essential Amino Acids). Cells were maintained at 37°C in humidified atmosphere containing 5% CO<sub>2</sub>. HDF of passages 4-7 were used.

### **2.2.3 HD-µTP culture**

To realize the human dermal micro tissue (HD-µTP), spinner flask bioreactor was inoculated with 10<sup>5</sup>cell\*ml<sup>-1</sup> and 2mg\*ml<sup>-1</sup> of microbeads, corresponding to 10 cells per bead. The culture suspension was stirred intermittently at 30 rpm (5 min stirring and 30 min static incubation) for the first 6h post-inoculation for cell adhesion, and then continuously agitated at 30 rpm up to 28 days. The growth medium was replenished on the first day

and every 2 days until the end of experiments. From the day 4<sup>th</sup>, 50µg/ml of ascorbic acid (l-ascorbic acid Sigma A-5960) were added and freshly added at each medium change.

## **2.2.4 Device realization**

The device was carved onto a Poly(methyl methacrylate) (PMMA, Goodfellow) slab of 1.2 mm of thickness using micromilling machine (Minitech CNC Mini-Mill). The design was performed in order to obtain an inlet channel (20 mm, 0.4 mm, 0.5mm of length width height respectively), a central chamber of (1.4 mm, 0.6 mm, 0.5 mm of length, width, height respectively), and an outlet channel of (20 mm, 0.4 mm, 0.5mm of length, width, height respectively), a loading channel (6.8 mm, 0.5 mm, 0.5mm of length, width, height respectively) was carved on the top of the chamber. Along the inlet and outlet channels were designed two circular shapes of 5.5 mm of diameter with function of accommodation for oxygen optical. The carved layer were bounded with a second layer of PMMA by ethanol immersion (15 min) and heat treatment (65° C for 1h).

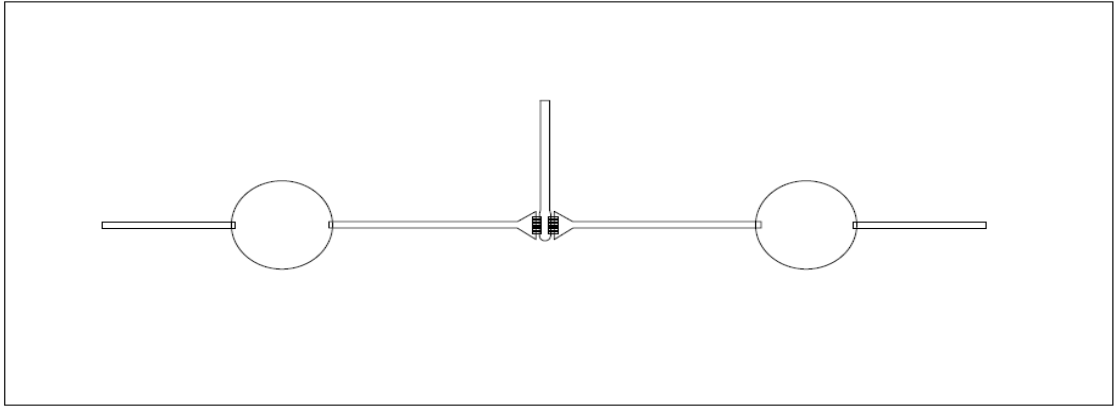


Figure 12 Device configuration

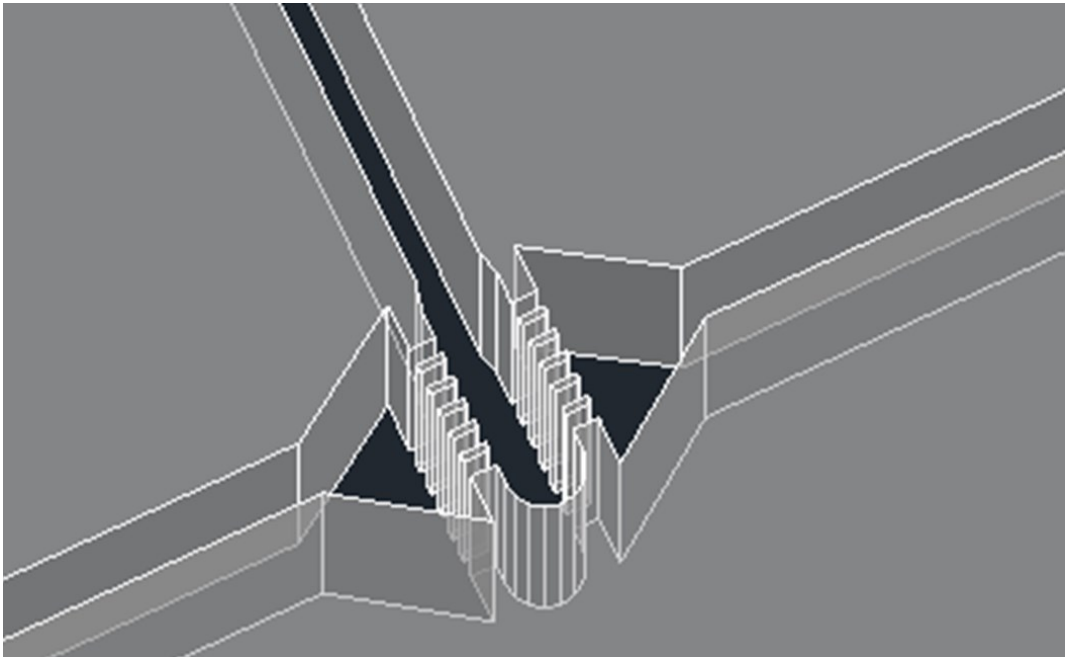


Figure 13 perfusion chamber zoom

## 2.2.5 Theoretical optimal flow rate calculation

The theoretical optimal flow rate was estimated by imposing the balance between the residence time ( $t_R$ ) of oxygen inside the chamber, and the time required to cells to consumption it ( $t_C$ ), as expressed in the equations 3-5:

$$t_R = t_C \quad (3)$$

$$t_R = \frac{L}{v} \quad (4)$$

$$t_C = \frac{V_{max} N_{cells}}{C} \quad (5)$$

where  $t$  is the time expressed in sec;  $L$  is the length of the chamber,  $v$  is the flow velocity,  $V_{max}$  is the maximum consumption rate of oxygen of the fibroblast;  $N_{cells}$  is the number of cells;  $C$  is the oxygen concentration expressed in  $\mu\text{M}$ .  $Q[0]$  means that the ratio between  $t_C$  and  $t_R$  is one,  $Q[-1]$  means that the ratio is 0.1, and  $Q[1]$  means that the ration is ten. The effectively flow rete values are 1  $\mu\text{l}/\text{min}$ , 0.1  $\mu\text{l}/\text{min}$  and 10  $\mu\text{l}/\text{min}$  respectively.

## 2.2.6 Oxygen consumption rate and profile inside the chamber

In order to evaluate the oxygen consumption kinetics of the HD- $\mu$ TP along culture time (days 0, 3, 7, 14, 21, 28) a small amount of microtissues were spilled from the spinner flask at each time point and placed in 3 different vials of frosted glass. The vials were filled with fresh culture medium and then placed in an incubator and kept at 37°C, under gentle agitation. The vials were then closed in order to avoid oxygen exchange with the surrounding environment. By means of an optical detector (OXY-4 PreSens) it was measured the oxygen concentration of the medium in the vials. The partial pressure was converted in oxygen concentration (C) by means of Henry's law. As control the same measurements were performed in three vials containing only medium and maintained in the same conditions. At the end of the experiment the HD- $\mu$ TP were enzymatically treated and the cell number was counted in order to obtain cell density in the medium ( $\rho$ ). By performing centered time derivative of the oxygen concentration curve, is possible to obtain the consumption velocity (V). By plotting V vs C a Michelis-Menten law kinetic is obtained. In order to evaluate the kinetics parameters, a linearization of the kinetics curve was performed by plotting  $V^{-1}$  and  $C^{-1}$ ; the intercept with y axis is  $V_{max}^{-1}$ , and the intercept of x axis is  $-K_m^{-1}$ . The oxygen consumption profile inside the

chamber was measured by using optical detector (OXY-4 PreSens), upstream and downstream of the cells chamber during 5h of trial. Starting from the “in” and “out” experimental oxygen values, obtained as below described, the computational fluid dynamic study (CFD) was performed by using Comsol Multiphysics vers 3.5. In particular, fixed the cells number (105 cell/ml) and the kinetic parameters ( $V_{max}= 10^{-16}$  mol\*s/cells;  $KM=10^{-6}$  mol/m<sup>3</sup>), 1  $\mu$ l/min, 0.1  $\mu$ l/min and 10  $\mu$ l/min were set as flow rate conditions respectively.

### **2.2.7 Live/dead assay**

In order to selectively stain live and dead cells for each flow rate, a LIVE/DEAD® Cell Viability solution (life technologies) were used, according to the manufacturer instruction. The HD- $\mu$ tp inside the device chamber were stained and placed on the confocal LSM710 Zeiss stage; the images were acquired by using two excitation/emission channels:  $\lambda_{ex}= 494$  nm,  $\lambda_{em}= 512-523$  nm (green channel: live cells) and  $\lambda_{ex}= 528$  nm,  $\lambda_{em}= 612-623$  nm (red channel: dead cells). The number of cells within the chamber was obtained by using the plug in analyze particle in the software imagej. The fraction of the live cells ( $\phi$ ) in each section was evaluated by using the following equation:

$$\phi = \frac{\pi^{\circ} \text{Live}}{\pi^{\circ} \text{Live} + \pi^{\circ} \text{Death}} \cdot 100 \quad (6)$$

## 2.2.8 Collagen observation and quantification

The HD- $\mu$ TP were imaged under multichanneled Leica TCS SP5 II coupled with a Multiphoton Microscope where the NIR femtosecond laser beam was derived from a tunable compact mode-locked titanium: sapphire laser (Chameleon Compact OPO-Vis, Coherent). Two-photon excited fluorescence ( $\lambda_{\text{ex}} = 840\text{nm}$ ) was used to induce second harmonic generation (SHG) of unstained neo-synthesized collagen structures by collecting the emission wavelength in the range  $\lambda_{\text{em}} = 420 \pm 5 \text{ nm}$ . For each flow rate, SHG images from HD- $\mu$ TP were analyzed by using imagej software. The degree of assembling of collagen network was evaluated by analyzing the intensity of SHG signal. The analysis was performed within the ECM space, all SHG images were subjected to noise subtraction and the intensity was evaluated as described by the equation (7):

$$\bar{I} = \frac{\sum_{i=1}^{255} I_i p_i}{\sum_{i=1}^{255} p_i} \quad (7)$$

where:  $\bar{I}$  is the average intensity,  $I_i$  is the intensity corresponding to the  $p_i$  pixel while the index  $i$  runs in the gray value interval: from 1 (less intensity) to 255 (more intensity). The intensity is proportional to the degree of assembly of the newly synthesized collagen [37, 38]. Fixed the optimal flow rate, three different concentration of ascorbic acid were tested: 0  $\mu$ g/ml and 50  $\mu$ g/ml and 100  $\mu$ g/ml.

## 2.2.9 Immunofluorescence on HD- $\mu$ TP and quantification

The HD- $\mu$ TP were fixed with 4% paraformaldehyde for 20 min at room temperature, rinsed twice with PBS buffer, and incubated for 2h at RT with PBS, BSA 5% and tryton 0.1% to block unspecific binding. Rinse again with PBS and incubated with mmp1 antibody (abcam) diluted 1:300 overnight at 4°C. Cover with the secondary antibody ALEXA FLUO 546 diluted 1:1000 at RT for 1h. After rising with PBS the samples were stained by 4',6-diamidin-2-fenilindolo (DAPI) 1:10000 for 10 minutes at RT the samples were observed with LSM710 Zeiss confocal microscopy. The quantification signal was performed by dividing the number of red pixels for the cells number, by using the following equation:

$$v = \frac{\sum_{i=1}^{255} p_i}{N} \quad (8)$$

where  $p_i$  is the number of pixel and  $N$  is the number of the cells. The number of pixels and the number of cells are obtained by imagej software routine: histogram and analyze particles tools are respectively used for the analysis.

## **2.3 Results**

### **2.3.1 Features of the device design**

The newly designed device presented here is able to simulate a perfusion bioreactor in micrometric scale in order to evaluate the better culture condition both from fluid-dynamic and biochemical point of view. Indeed this system may support several cases of study in order to test the effect of flow rates, to test substance (growth factors, biochemical, etc.) exposure, and evaluating the correlated extracellular matrix rearrangements. The innovative design is able to perform on line analysis without effecting on the

cells viability, proliferation and metabolic activity; all these characteristics integrate the set of the advantages related to microfluidic device.

### **2.3.2 Oxygen consumption rate and profile inside the chamber**

The oxygen rate consumption, describe the demand of nutrients related with  $\mu$ tps age; in the first time point was measured the maximum value of  $2.1 \cdot 10^{-8}$ , two time highest of 7 days point. Just from 2 weeks the initial value let down of an order of magnitude, value confirmed for all trial time points. This trend suggest the possibility to use tissue precursor between seven and fourteen days in order to obtain HD- $\mu$ tp with low metabolic demand. The oxygen profiles inside the chamber, evaluated in three different flow rate conditions named Q[0] (i), Q[1] (ii) and Q[-1] (iii) as described in the section 1.3.5, show how for (i) and (iii) conditions the flow rate are able to guarantee a relevant nutrient transport and exogenous substances exchange along the maturation chamber to the HD- $\mu$ tps; the measured values are  $22.13\% \pm 2.47\%$  and  $92.79\% \pm 1.30\%$  respectively. Moreover in (ii) condition, the oxygen transport doesn't happens for all the chamber length, giving as output value always zero. This suggest that this flow rate generates a stress condition for the cultured tissue.

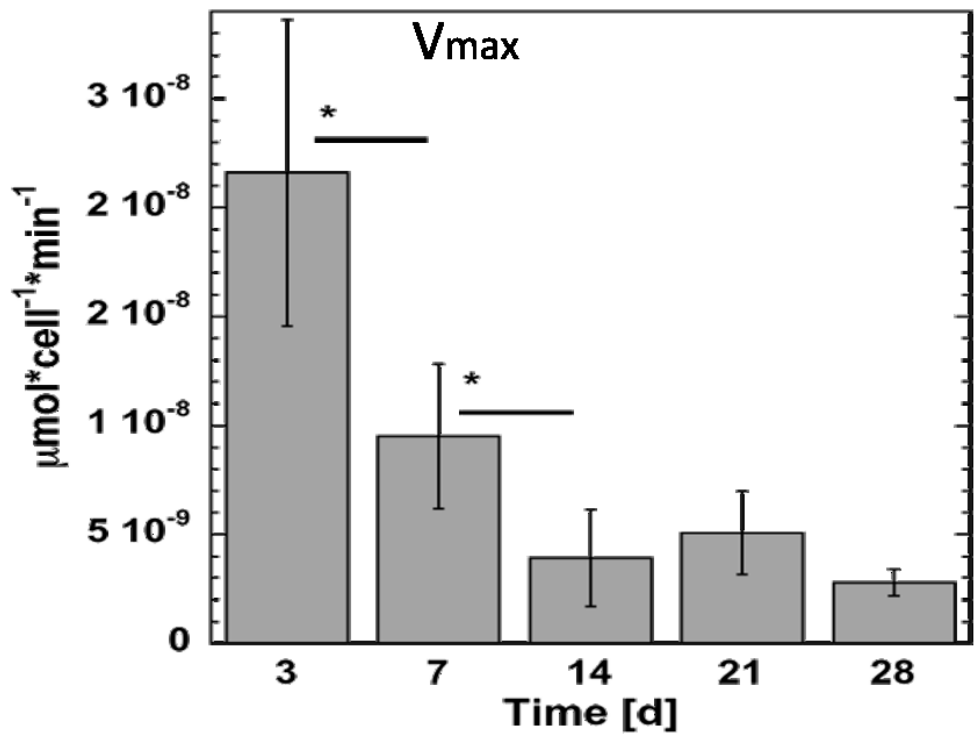


Figure 14 oxygen consumption rate measured during culture time

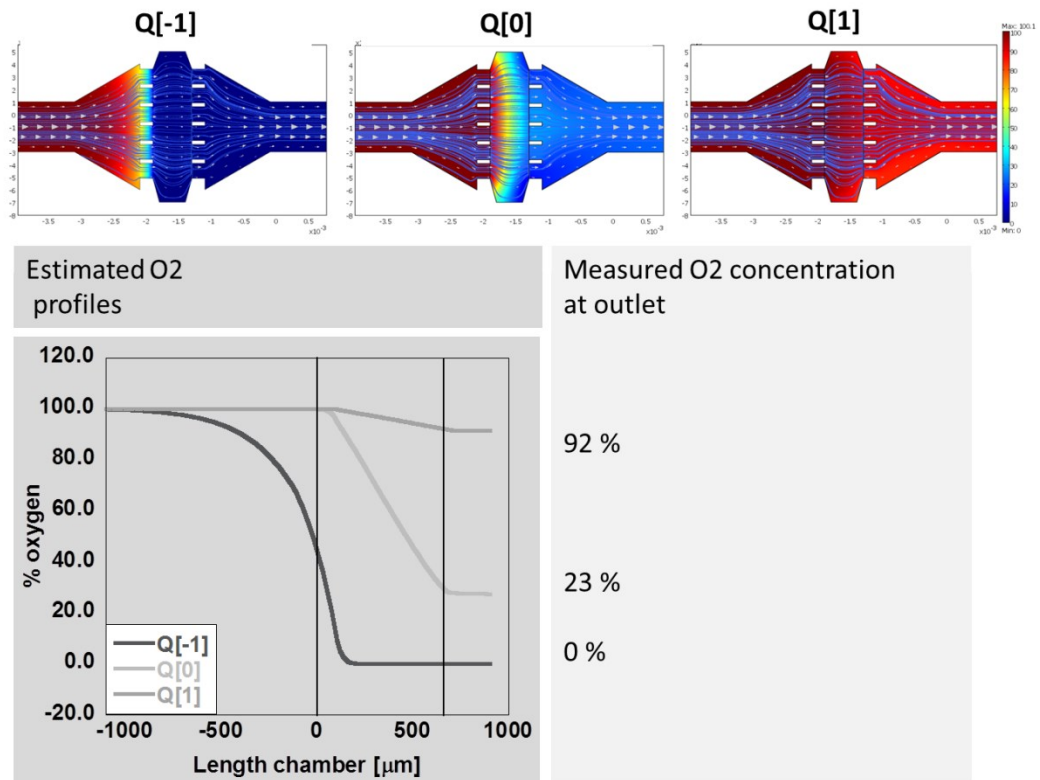


Figure 15 simulation of oxygen profile inside the chamber for three several flow rate conditions: Q[0]; Q[1]; Q[-1]; oxygen concentration along length device.

### 2.3.3 Cells viability VS flow rate

The cells vitality inside the chamber during four days of culture time, show how the flow rate influence the cellular proliferation. In particular, this results, coupled with the oxygen consumption profiles, further clarify that the for Q[0] and Q[1] flow rates conditions allow the duplication, indeed the total number of cells is around double respect to the initial value . In lower flow rate, the total number of live cells enhance of the 40%, this is due to the

lower number of live cells able to duplicate themselves. The % of dead cells increase during culture time until 30%, while is approximately constant at Q[0] and Q[1].

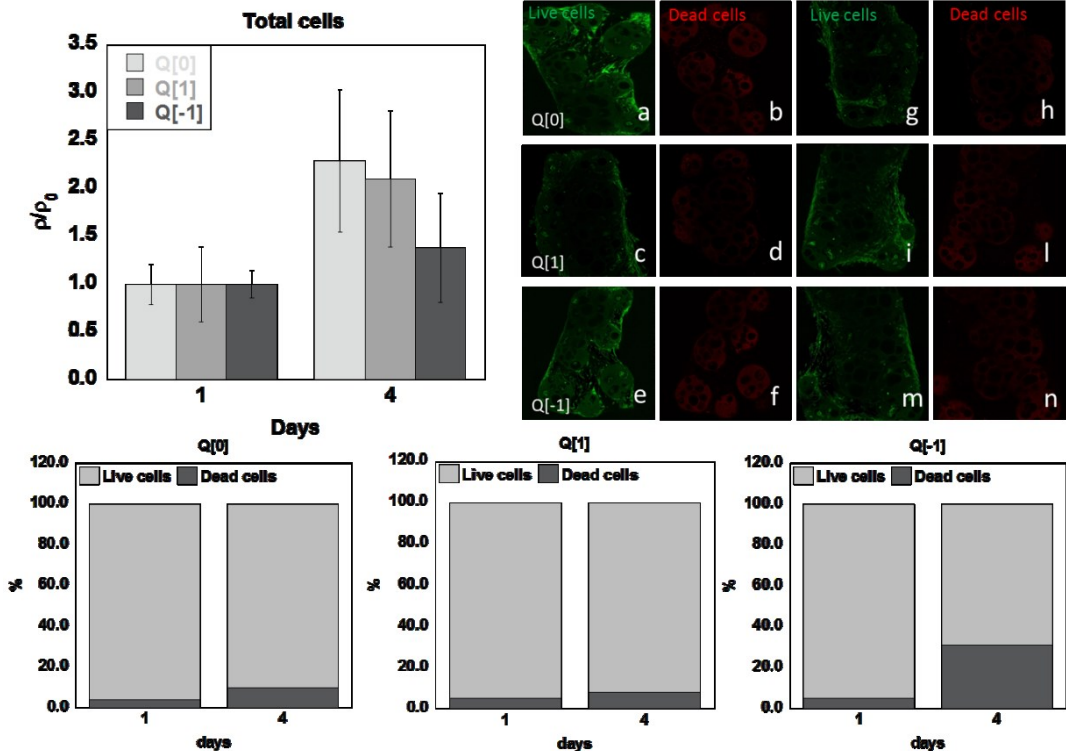


Figure 16 total cells number; live dead fraction VS flow rate at 0 days (a-f) and 4 days (g-n); fraction of live/dead cells quantification

### 2.3.4 MMP-1 profile

The metalloproteinase one synthesis shows the HD- $\mu$ tp answer to hypoxic condition; the trend for Q[0] and Q[1] flow rate is constant during culture time. Moreover for the Q[-1] flow rate condition the value increase respect

to the initial value of about 40%, and statistical difference were detected between this culture condition and the other flow rates. This result confirm that the HD- $\mu$ tps, cultured with Q[-1] flow rate, are under stress condition, and due to it, they secrete more MMP-1per cell. This increase leads to a collagen reorganization, as figure 10 shows.

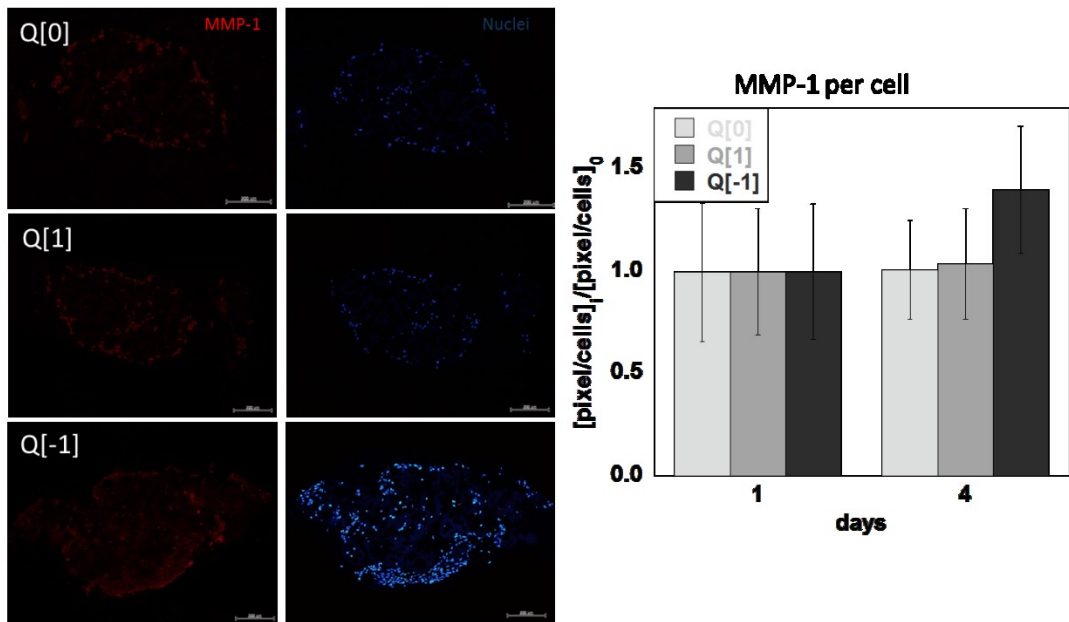


Figure 17 MMP-1 synthesis VS flow rate; MMP-1 in red, nuclei in blue, quantification of the red signal per cell

### 2.3.5 SHG intensity VS flow rate

The SHG signal intensity is an index of the collagen assembling; higher value corresponds to the assembled collagen, while lower value is due to neo synthesized collagen [37, 38]. The SHG intensity VS Q[-1] flow rate

shows how the signal decrease confirming the global suffering status of the HD- $\mu$ tp. The Q[1] flow rate, although from the oxygen profile and cells viability point of view seem to be a good culture condition, it isn't for collagen assembling. In particular the intensity value remains constant, clear evidence that the newly collagen is secreted but washed out. Only for Q[0] condition the value increase of about 50%, so we can deduce that this is the best flow rate in terms of cells viability, oxygen exchange, MMP-1 synthesis, and collagen assembling.

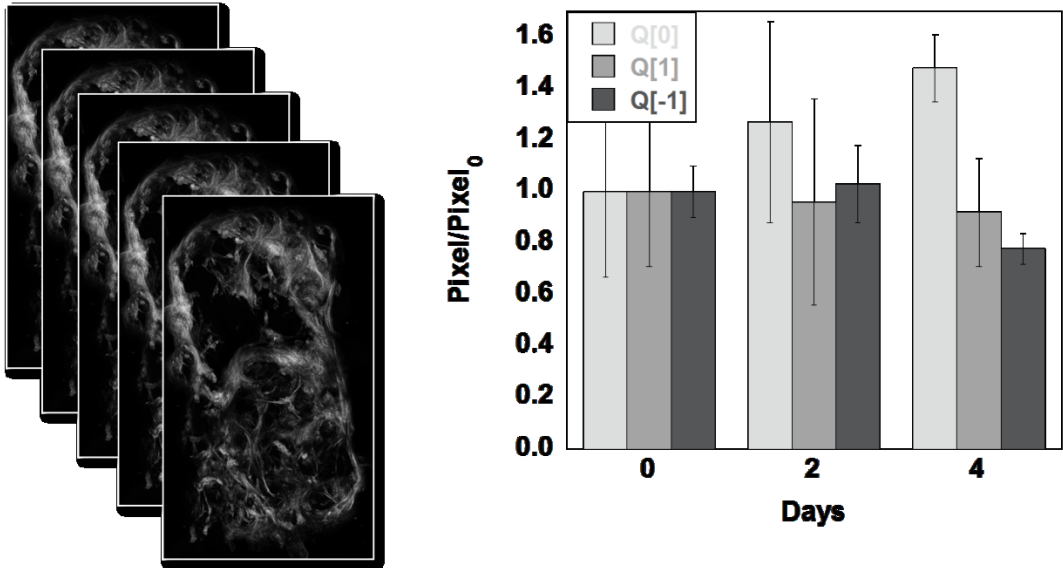


Figure 18 volumetric collagen intensity VS flow rate

### **2.3.6 SHG intensity VS ascorbic acid concentration**

The ascorbic acid addition to the culture medium increase the proliferative rate and stimulate the synthesis and the secretion of appropriate ECM components, in particular collagen [59-61]. Fixed the optimal flow rate, several ascorbic acid concentration were tested: 0 $\mu$ g/ml, 50  $\mu$ g/ml and 100  $\mu$ g/ml. In the first case study (0  $\mu$ g/ml) the intensity value increase of about 50% during four days of culture time, while in case of 50  $\mu$ g/ml the acquired signal is higher of two times respect to the initial value, and the difference is statistically significance ( $p < 0.0001$ ). For the higher concentration (100  $\mu$ g/ml) the collagen signal decrease, this is due to cytotoxicity that ascorbic acid show to the equal or greater concentration of 100  $\mu$ g/ml [61-63].

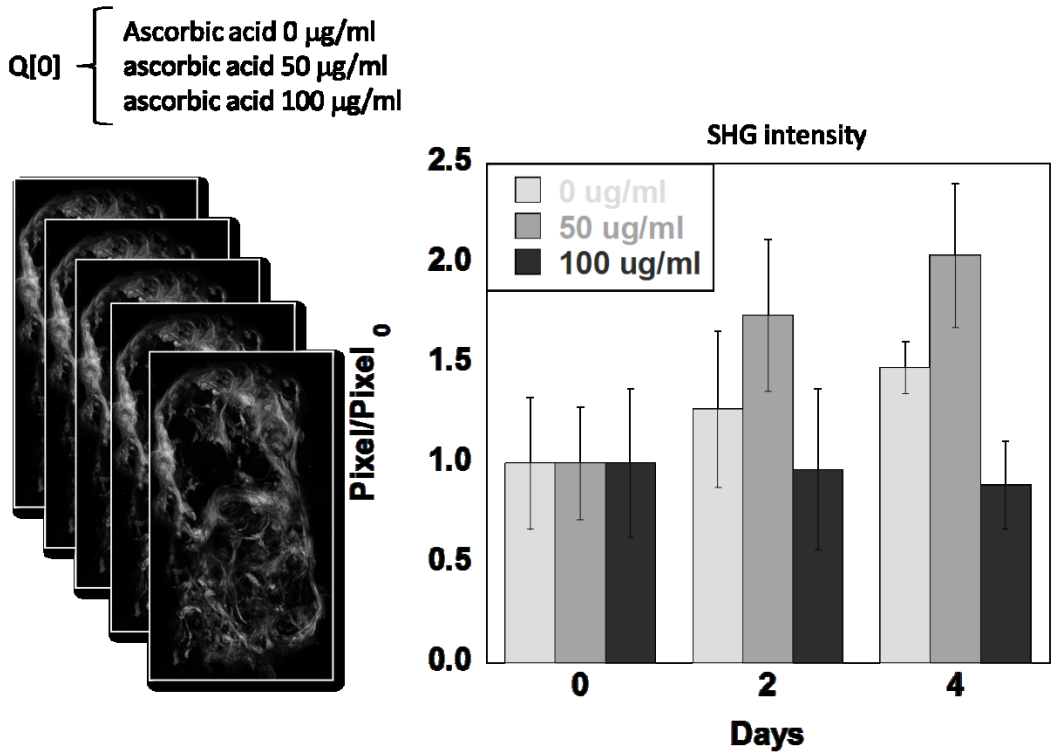


Figure 19 Volumetric collagen intensity VS ascorbic acid concentration

## 2.4 Discussion

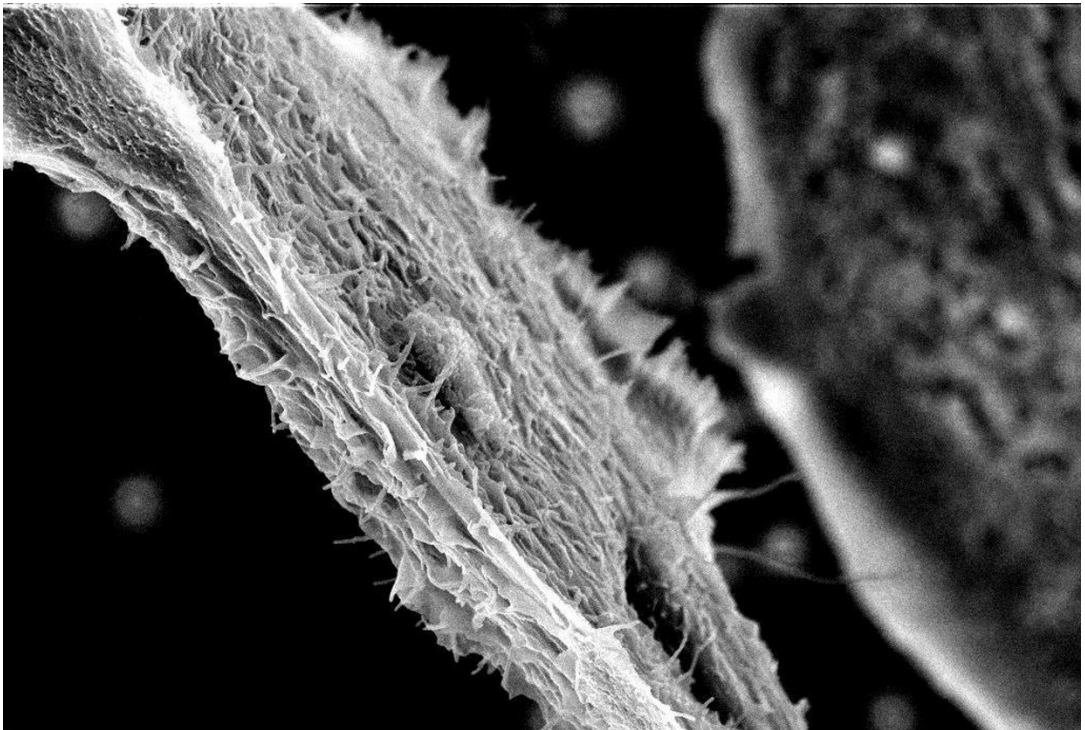
In this work we demonstrated the capability to create a perfusion micro-chamber in order to simulate a bioreactor in micrometric scale. In this system we can test, in short time (1 week), both physical and biochemical parameters, in order to establish the better culture condition. The primary advantage of this screening platform is related to the great number of on-line acquisition; this allows to do a large number of studies in only one experiment, indeed can be evaluated together several aspects of the culture

conditions (flow rate, nutrient transport, collagen assembling). Starting from a measured oxygen consumption rate of the HD- $\mu$ tp during culture time, is possible to calculate the time need to the cells for a total oxygen consumption inside the chamber. By comparing this characteristic time with the residence time of the oxygen in the chamber, it is possible to deduce the optimal theoretical flow rate ( $Q[0]$ ), test it or other flow rate conditions, for example flow rate ten time higher ( $Q[1]$ ) and flow rate ten time lower ( $Q[-1]$ ), and quickly experimentally verify the good performance for the final tissue structure point of view. Concerning the oxygen profile inside the chamber, the results show two efficient conditions  $Q[0]$  and  $Q[1]$ , due to a prevalence of the diffusive and convective transport through the chamber respect to the cellular consumption; while for  $Q[-1]$  flow rate the diffusion and the convection are negligible respect to the consumption term. The total number of cells on the 3D increase, but in  $Q[-1]$  the duplication rate is lower due to an enhance of dead cells; this stress condition brings to a MMP-1 synthesis rise too that reflect itself in a reduction of collagen assembling degree. The collagen assembling is a crux in order to select the better culture condition, indeed only  $Q[0]$  leads to an increase of it, while  $Q[1]$  doesn't allow the assembling, certainly due to the wash out phenomena. Just selected the better flow rate in terms of oxygen exchange, cells vitality, MMP-1 synthesis and collagen assembling, can be tested biochemical factors too, in our case ascorbic acid, and the concentration

effects. This possibility gives the great advantage to better understand how each factor influences the tissue answer and the extracellular matrix reorganization to external stimuli. The cellular fate is mediated by biochemical signaling, that act as a start for cascade signaling [64], to direct the cells towards the differentiation, ECM synthesis and remodeling, etc. By using this innovative micrometric testing platform, is possible to perform a short time experiment able to answer to several kind of questions; this device allows to perform on-line analysis, and this nondestructive characteristic, its versatility, is the plus respect to the others macrometric bioreactors.

## Chapter 3

### 3D airway epithelium equivalent



# Chapter 3

## 3.1 Introduction

Cellular culture in a monolayer system is a basic biological procedure for investigation of the pathogenesis of diseases [65]. Isolated cells can only simulate a small part of the body's complexity and often lose their morphology and functional properties [1]. It is well known that cells need an appropriate matrix as an optimal cell support to develop their typical differentiated phenotype in vitro [66]. There has been significant success in producing artificial skin by combining dermal fibroblasts in contracted collagen gels with human keratinocytes [67, 68], and in creating three-dimensional (3D) cultures reproducing some of the characteristics of a cornea by combining keratinocytes with corneal epithelial cells. Both of these systems exhibit a stratified squamous epithelium [69]. There has only been very limited success in producing artificial tissues using other types of epithelium such as bronchial epithelium [69], though others have reported organotypic cultures containing both human lung fibroblast cell lines and either primary or immortalized human bronchial epithelial cells (HBECs) [70]. We therefore designed this study to evaluate the feasibility of an in vitro model of bronchial mucosa produced by bottom-up tissue engineering, examining the effect of collagen concentration and arrangement, the role of

the stroma on the phenotype of primary HBECs in a 3D culture environment. The airway epithelium is pseudostratified, features leakier tight junctions and a smaller surface area than the alveolar epithelium, and is protected by a mucociliary clearance mechanism [71, 72]. To usefully predict the fate of compounds delivered to the lung, a model of the airway epithelium should reflect the drug transport characteristics and metabolic activity encountered *in vivo*. *In vitro* models of human tissues that are biomimetic and closely represent the functional properties of their respective tissues could enable better understanding of disease processes, hence providing more physiologically relevant platforms for identification of targets for therapy as well as testing the efficacy and safety of new drug leads [73]. Using such *in vitro* models in drug discovery cycle could in turn substantially reduce the number of drug leads that need to be taken forward to preclinical studies and, therefore, reducing the number of animals required for such experiments [74]. The respiratory system is constantly exposed to potentially harmful particles, allergens, and pathogens. Epithelial cells are the predominant cell type in contact with the air and as such the airway epithelium forms the first line of defense against airborne insults [75]. Epithelial cells are structurally arranged to form a continuous layer and are joined via protein junctions to create a paracellular barrier to shield interstitial tissue from the airway [74]. As well as a physical barrier, the epithelium forms a chemical barrier via cellular secretions, for example,

mucus that entraps infiltrating particles. The use of commercially available two-dimensional (2D) platforms upon which epithelial cells can be cultured at the air–liquid interface (ALI) is widely practiced. The use of a 3D tissue equivalent is favorable over 2D cell culture providing more *in-vivo*-like morphology, function, and intercellular interactions enabling greater resemblance to physiological conditions. The literature models are all made of exogenous collagen and HDF [69] , or using lung fibroblasts seeded in exogenous collagen, or polyethylene terephthalate scaffold (PET) scaffold[1, 74].

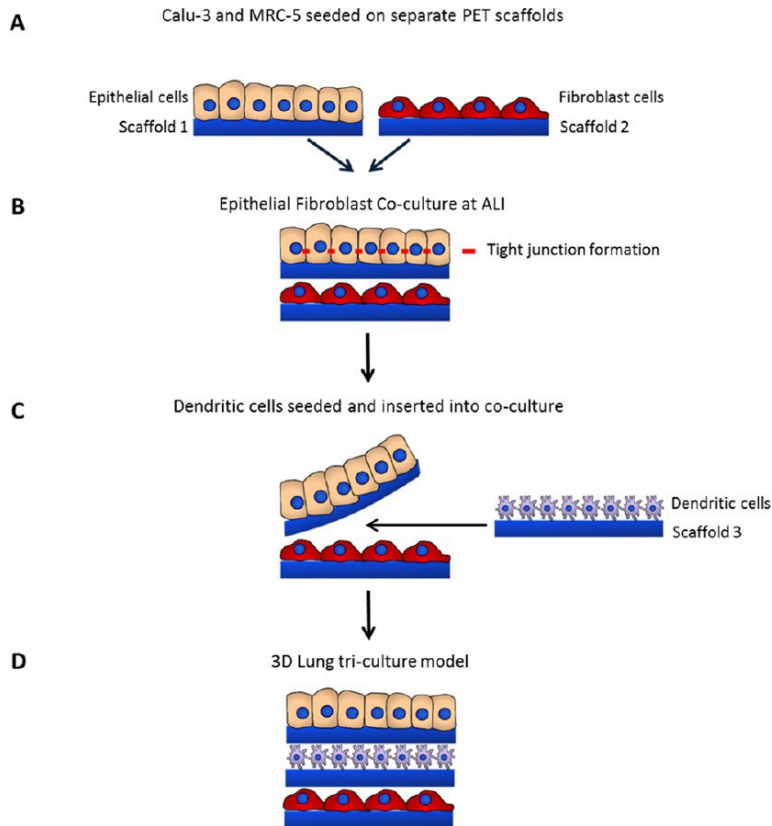


**Figure 20** Schematic figure showing different steps of fabrication and configuration of the 3D tissue engineered airway epithelium. Calu-3 epithelial cells are seeded onto one PET scaffold and MRC-5 fibroblasts are seeded onto a second, separate scaffold (A). Following 72 h culture, scaffolds are combined by layering the epithelial scaffold monolayer on top of the fibroblast scaffold layer to form the coculture model. Cells are subsequently cultured for 2 weeks at the ALI to allow for differentiation of the epithelial cells, including establishment of tight junctions (B). Monocyte-derived DCs are seeded onto separate PET scaffolds and then inserted into the coculture model. The upper epithelial scaffold is temporally lifted away from the lower MRC-5 fibroblast layer so that the separate third scaffold containing dendritic cells may be placed on-top of the MRC-5 scaffold layer (C). The Calu-3 layer is placed on-top of the DC scaffold layer, resulting in the DC layer sandwiched between the epithelial and fibroblast scaffold layers to form the triculture model (D). adapted from [77]

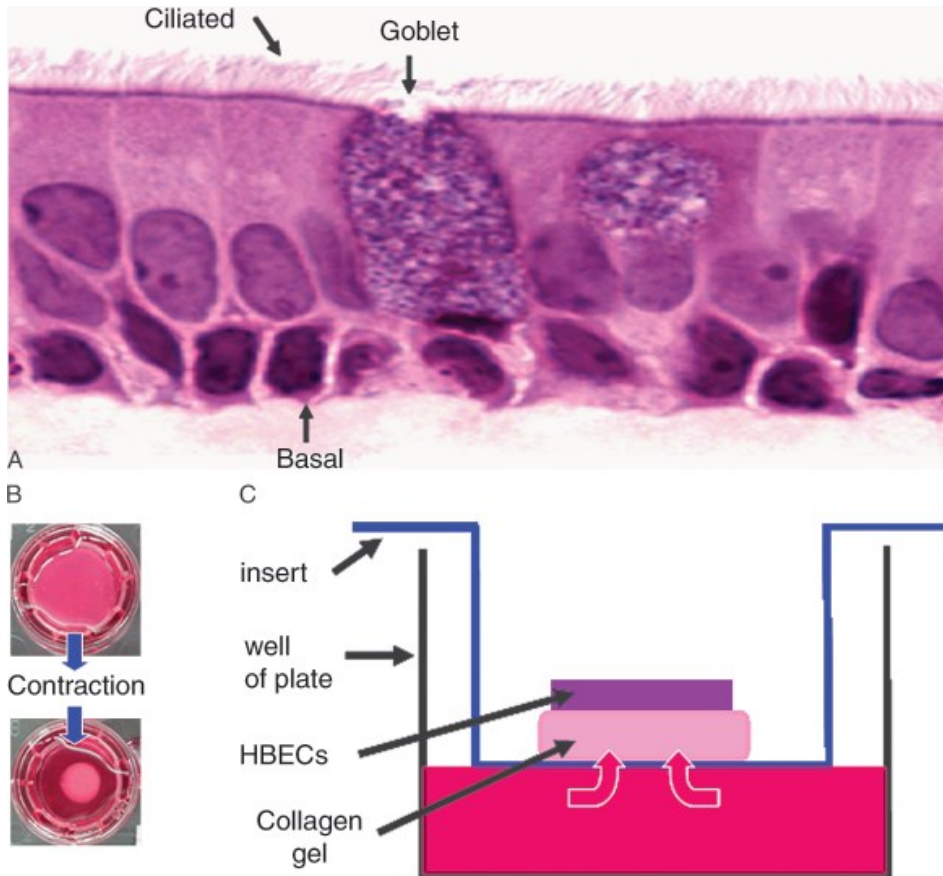


**Figure 21 Development of the organotypic culture. Normal human bronchial epithelium contains ciliated columnar cells, mucous-producing goblet cells, and basal cells (A). To produce a bronchial “submucosa” in vitro, fibroblasts were combined with type I collagen, allowed to gel (B, top), then the gel was released from the dish and allowed to contract over a period of 4–7 days (B, bottom). Bronchial epithelial cells were then seeded onto the top of the gels and allowed to attach for 4 hr to create the organotypic culture. Cultures were submerged for 4 days, then placed into a 6-well insert which was fed from beneath by media placed into well below the insert (C), thereby leaving the upper surface of the tissue emerged from the media. Triplicate cultures were placed into each insert. Cultures were fed every other day, and harvested at various time points in culture. Adapted from [72]**

Such models have some limits, including the absence of an endogenous matrix environment, which plays an important role in intercellular communications [1]. Our model possesses endogenous ECM able to

organize themselves as *in vivo* lung tissue; it is reasonable cellular and structural representation of the airway epithelium and is amenable to *in situ* monitoring, and as such, it presents an invaluable tool for academic and pharmaceutical research within the fields of lung biology, disease modeling, and drug discovery and delivery.

## **3.2 Material and methods**

### **3.2.1 Microscaffold production**

Gelatin porous microbeads (GPMs) have been prepared according to a modified double emulsion technique (O/W/O). Gelatin (type B Sigma Aldrich Chemical Company, Bloom 225, Mw=1 76654 Dalton) was dissolved into 10 ml of water containing TWEEN 85 (6% w/v) (Sigma Aldrich Chemical Company). The solution was kept at 40°C. Toluene containing SPAN 85 (3% w/v) (Sigma Aldrich Chemical Company) was continuously added to the aqueous gelatin solution (8% w/v) to obtain primary oil in water emulsion. Beads of gelatin containing droplets of toluene were produced through the addition of excess toluene (30 ml) that allowed for a double emulsion (O/W/O). The resulting microspheres were filtered and washed with acetone and then dried at room temperature. Microspheres were separated selectively by using commercial sieves (Sieves IG/3-EXP,

Retsch, Germany). GPMs with 75-150  $\mu\text{m}$  size range were recovered and further processed. GPMs have been stabilized by means of chemical treatment with glyceraldehyde (GAL), in order to make them stable in aqueous environment at body temperature. In particular, GPMs were dispersed into an acetone/water solution containing 4% of GAL and mixed at 4°C for 24 h. Then microspheres were filtered and washed with acetone and dried at room temperature. Before their use in cell culture dry GPM were sterilized by absolute ethanol sub-immersion for 24h. After that, in order to remove ethanol completely, several washings in calcium-free and magnesium-free phosphate-buffered saline (PBS) were performed. Before cell seeding PBS was removed and replaced with the culture medium.

### **3.2.2 Cell expansion**

Normal human lung fibroblast (Lonza) were sub-cultured onto 150  $\text{mm}^2$  Petri dishes in culture medium (Eagle's BSS Minimum Essential Medium containing 20% fetal bovine serum, 100  $\mu\text{g}/\text{mL}$  L-glutamine, 100 U/mL penicillin/streptomycin, and 0,1 mM Non Essential Amino Acids). Cells were maintained at 37°C in humidified atmosphere containing 5%  $\text{CO}_2$ . NHLF of passages 4-7 were used.

### **3.2.3 HL- $\mu$ TP culture**

To realize the HL- $\mu$ TP, spinner flask bioreactor was inoculated with  $10^5 \text{cell} \cdot \text{ml}^{-1}$  and  $2 \text{mg} \cdot \text{ml}^{-1}$  of microbeads, corresponding to 10 cells per bead. The culture suspension was stirred intermittently at 30 rpm (5 min stirring and 30 min static incubation) for the first 6h post-inoculation for cell adhesion, and then continuously agitated at 30 rpm up to 28 days. The growth medium was replenished on the first day and every 2 days until the end of experiments. From the day 4<sup>th</sup>,  $50 \mu\text{g}/\text{ml}$  of ascorbic acid (l-ascorbic acid Sigma A-5960) were added and freshly added at each medium change.

### **3.2.4 Realization of 3D human lung equivalent**

Tissue precursors obtained as described in 3.2.3 section, have been injected in maturation chamber to allow their molding in disc-shaped construct (1 mm in thickness, 5 mm in diameter). During the filling procedure the mold were connected with a vacuum pump to assure that no bubbles were in maturation space. Completed the filling process, the mold were closed by grids and placed on the bottom of a spinner flask and completely surrounded of culture medium for two weeks. The spinners was operated at 60rpm and the medium was exchanged every three days. After

4 weeks of culture, under dynamic conditions, the bio-hybrid obtained has been removed from the maturation chamber and seeded with Normal human bronchial epithelial cells in order to obtain the epithelial layer.

### **3.2.5 Realization of human bronchial epithelium**

The 3D stroma equivalent for bronchial epithelium was accommodate on transwell insert (corning), coated by 20µl of human fibronectin solution (Sigma Aldrich) to final concentration of 50 µg/ml and let dry to air for 45 minutes at room temperature. Wash the NHBE cells with PBS/EDTA 0.01M, trypsinize NHBE colonies with trypsin/EDTA for 5 min at 37°C to obtain a single cell suspension. Centrifuge at 1200 rpm for 5 min, gently resuspend high density cells in fresh medium, seed 200,000 cells/3D equivalent and incubate at 37°C for 60 min. In order to stimulate the cell proliferation, during the first three days the 3D bronchial epithelium equivalent were cultured in submerged condition, while to favorite the differentiation during second and third week were cultured in air liquid interface condition. For submerged culture the BEGM (LONZA) was added both on the top and on the bottom of the transwell, while for air liquid interface condition the BEGM was mixed with DMEM (LONZA) 1:1 and added only on the bottom of the polycarbonate membrane.

### **3.2.6 Immunofluorescence, multiphoton imaging and histology on HL- $\mu$ TP**

Aliquot of 1 ml aliquots were collected at day 1, 3, 7, 14, 21 and 28 from the spinner culture and the HD- $\mu$ TP were stained with phalloidin tetramethylrhodamine B isothiocyanate (Sigma-Aldrich) and SYTOX® Green (INVITROGEN) for cell cytoskeleton and cell nuclei detecting respectively. Briefly, for both analyses, the HL- $\mu$ TP were fixed with 4% paraformaldehyde for 20 min at room temperature, rinsed twice with PBS buffer, and incubated with PBS-BSA 0.5% to block unspecific binding. In particular the samples were incubated with SYTOX® Green stock solution (10 mg/mL in dimethyl sulfoxide) diluted in PBS (1/500 v/v) for 10 min at 37°C, and after rinsing in PBS, they were stained with phalloidin for 30 min at room temperature. After that, the stained HL- $\mu$ TP were imaged under multichanneled Leica TCS SP5 II coupled with a Multiphoton Microscope where the NIR femtosecond laser beam was derived from a tunable compact mode-locked titanium: sapphire laser (Chameleon Compact OPO-Vis, Coherent). Two channels were used for confocal imaging of cell nuclei ( $\lambda_{\text{ex}} = 500 \text{ nm} / \lambda_{\text{em}} = 520\text{-}530 \text{ nm}$ ) and cytoskeleton ( $\lambda_{\text{ex}} = 573 \text{ nm} / \lambda_{\text{em}} = 588\text{-}598 \text{ nm}$ ) respectively. Two-photon excited fluorescence ( $\lambda_{\text{ex}} = 840 \text{ nm}$ ) was used in another channel to induce second harmonic generation (SHG) of unstained neo-synthesized collagen structures by collecting the emission

wavelength in the range  $\lambda_{em} = 420 \pm 5$  nm. For histological analysis, 1 ml of HL- $\mu$ TP suspension was fixed in a solution of 10% neutral buffered formalin for 24 h, dehydrated in an incremental series of alcohol (75%, 85%, 95% and 100%, and 100% again, each step 20 min at room temperature) treated with xylene and then embedded in paraffin. Successively, the samples were sectioned at a thickness of 6  $\mu$ m, and stained with hematoxylin and eosin. The sections were mounted with Histomount Mounting Solution (INVITROGEN) on coverslips and the morphological features of constructs were observed with a light microscope (Olympus, BX53). Furthermore, deparaffined 6  $\mu$ m sections were immune-stained by using keratin 14, P63, collagen I and IV, ZO-1 were performed using keratin 14 polyclonal antibody (dilution 1:1000; Covance), Anti-p63 monoclonal antibody (dilution 1:50; abcam), Anti-collagen I monoclonal antibody (dilution 1:500; abcam), Anti-collagen IV monoclonal antibody (dilution 1:500; abcam) and Anti-ZO-1 polyclonal antibody respectively as primary antibody and Alexa fluor 488, Alexa fluor 546 and Alexa fluor 568 respectively as secondary antibody.

### **3.2.7 Scanning Electron microscopy**

The samples were observed using a scanning electron microscopy (FESEM UltraPlus Zeiss), dehydrated by gradually increasing the ethanol concentration (75%, 85%, 95% and 100%, for 20 min at room temperature) a placed in CDP critical point dryer. Subsequently they were place on conductive stub, metalized by Cressington 208HR High Resolution Sputter Coater with a 5nm of Au and observed by using a voltage of 7KV.

## **3.3 Results**

### **3.3.1 HL- $\mu$ TP Evolution: cell proliferation and biosynthetic activity**

The  $\mu$ tps evolution were evaluated during 28 days; as shown in figure 22 the number of cells per  $\mu$ tp grows during all the investigated temporal window, starting from 10 cells per microbead until to 310 cells per microbead, and the duplication rate remains constant.

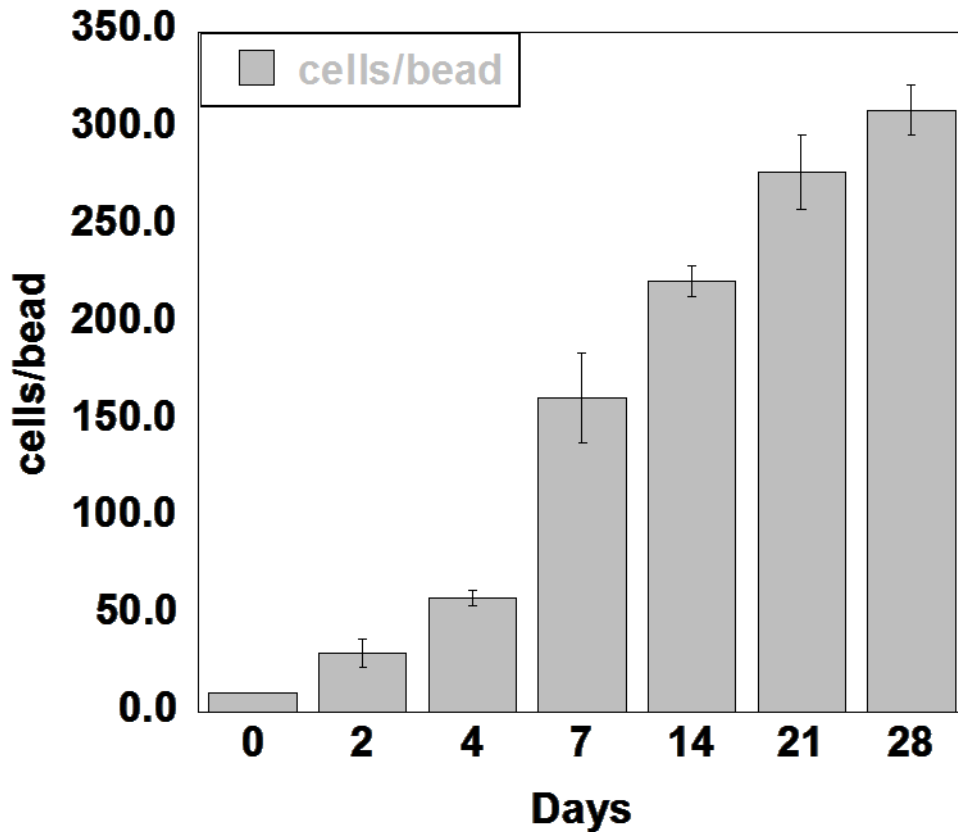


Figure 22 growth curve of NHLF per bead during culture time

The figure 23 assesses the presence of a viable neo-tissue that evolves and changes itself in terms of fusion capability and number of cells (a-e). The cells are able to colonize the space between each bead, and they colonize both the external surface and within the microbeads pores (l-o). The cells are embedded in own extracellular matrix, that evolves and changes the characteristics of the final tissue (f-i). The collagen signal inside the HL- $\mu$ TP increase consistently during culture time, making themselves, although in micrometric scale, complete tissue with own

organization and structure.

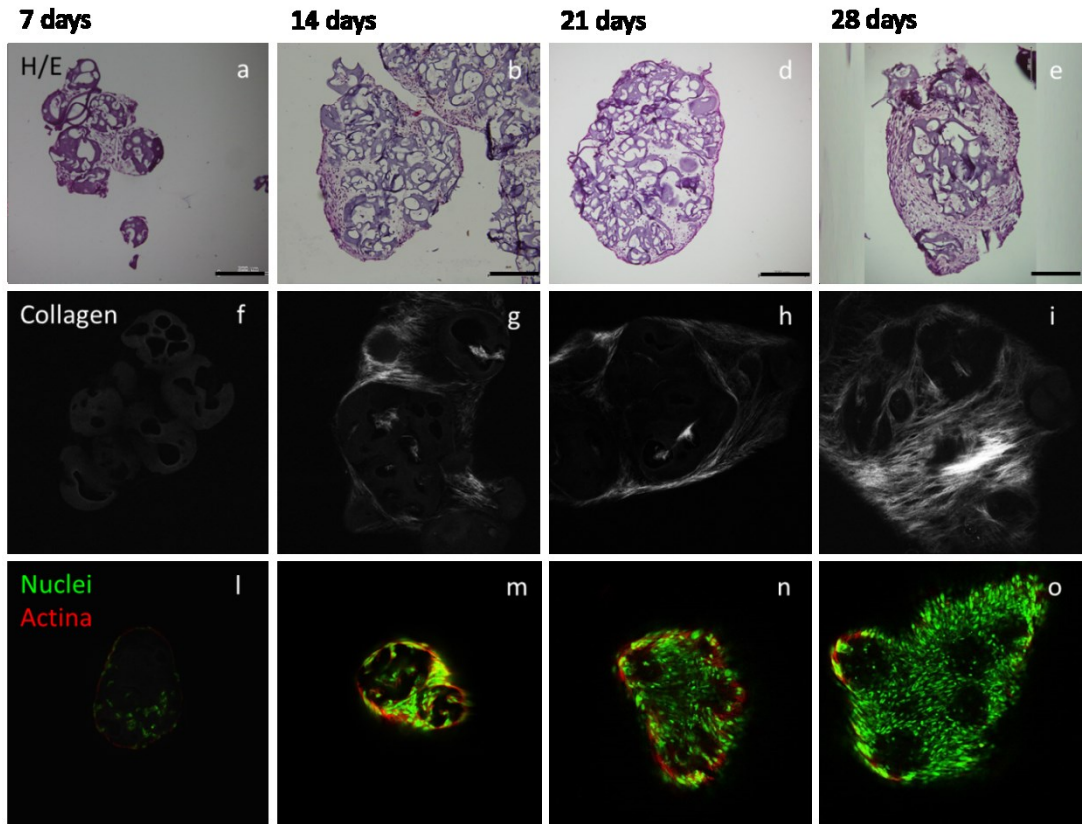


Figure 23 HL-  $\mu$ tp evolution during culture time: H/E staining during (a-e), SHG collagen signal (f-i) nuclei ad actina distribution (l-o)

### 3.3.2 Morphological analysis of human lung equivalent

The image 24 shows the differences between our 3D lung model, the 3D dermis model and lung structures *in vivo*, both in macroscopic and ultrastructural point of view. The histological image of lung (24g) shows a

classical sponge structure; in our model this kind of structure is repeated, in contrast with the human skin equivalent. The lung fibroblasts are completely immersed in their own extracellular matrix, the presence of collagen suggests that the cells not only proliferated but also work correctly, by secreting and remodeling collagen. Moreover, the close interdependence of matrix remodeling, mechanical properties and shape retention is fundamental to preserve the integrity in soft tissue. In this 3D structure the collagen isn't organized in parallel fibrils as detectable in human dermis equivalent, but the ECM is able to recreate the sponge structure such as the human lung *in vivo*. The immunofluorescence analysis shows the collagen I (25a) and collagen IV (25b) signals. The presence of these two types of collagen allows the correct differentiation of the epithelium [76]

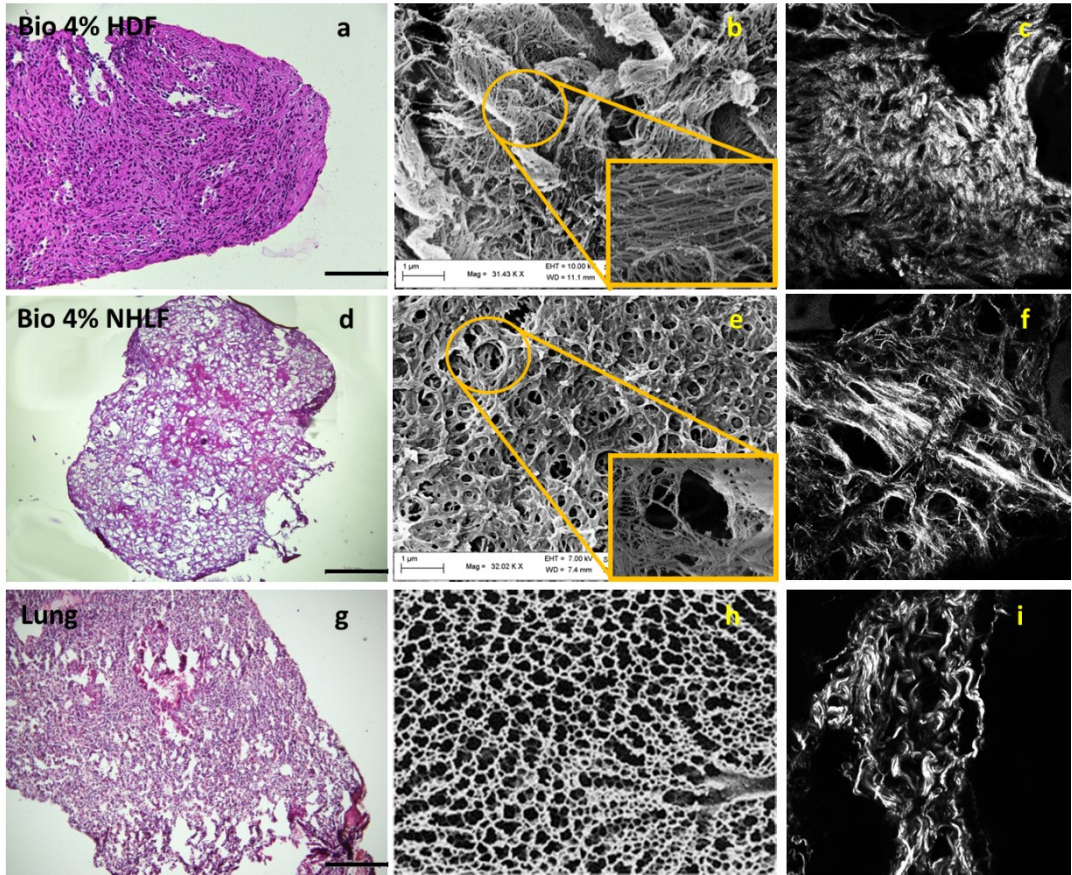


Figure 24 comparison of human skin equivalent, airway epithelium equivalent and lung structure; H/E staining (a-d-g), SEM (b-e-h) and MP (c-f-i) image

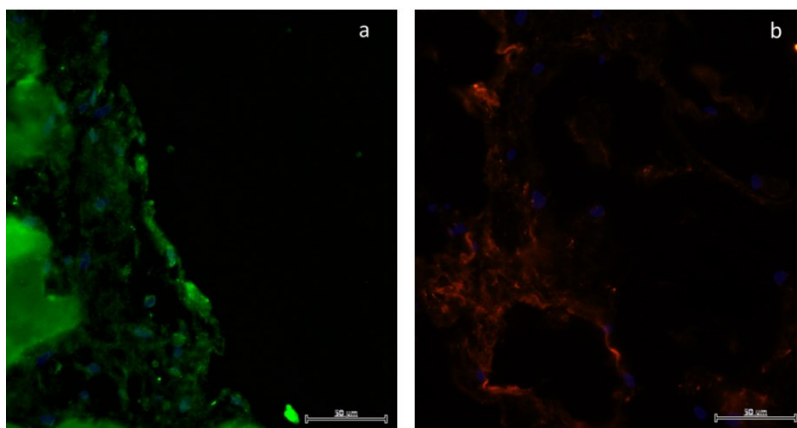
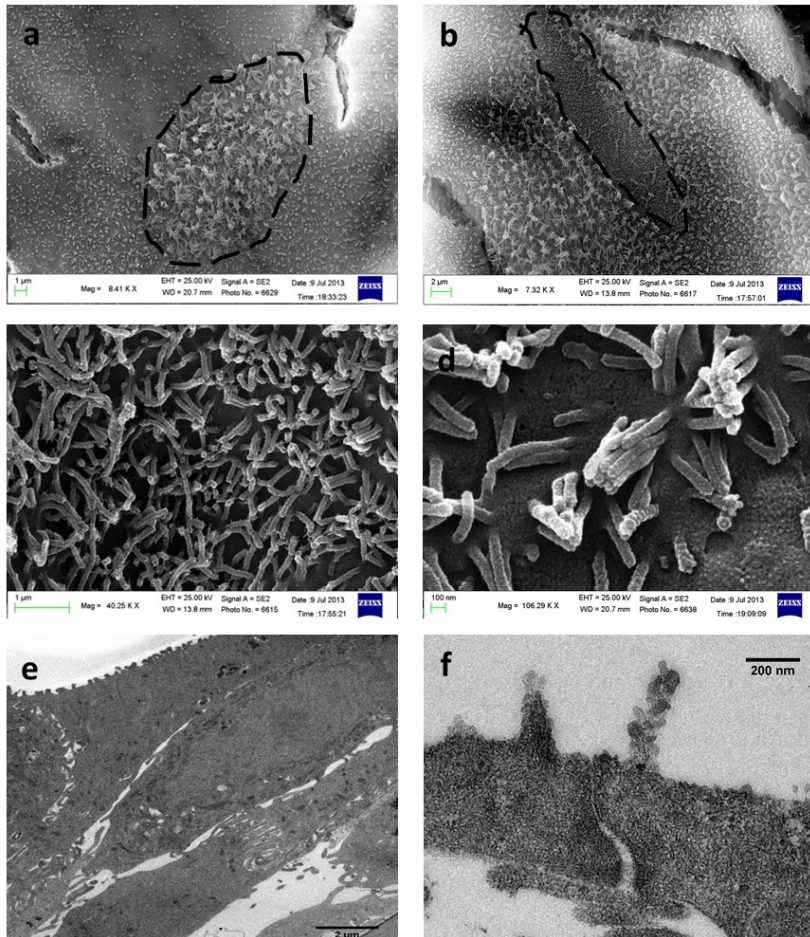


Figure 25 immunofluorescence analysis of histological section with thick 5 µm of human lung equivalent; Collagen I in green (a) and Collagen IV in red (b); scale bar 50 µm

### 3.3.3 Morphological analysis of 3D human bronchial epithelium equivalent

The normal human bronchial epithelial cells grow directly on 3D, during the submerged condition the proliferation is favorite, while in air-liquid interface condition overbear the differentiation. The resultant epithelium demonstrates a greater degree of tissue architecture and organization; both ciliate and goblet cells colonize the more external layer. The image 26a and b shows well delimited cells, the dashed lines underline the cellular borders of a ciliate cell surrounded of goblet cells (a) and goblet cell surrounded of ciliate cells (b). Ciliate cell zoom (c) shows the uniform distribution of the cilia on all the cell surface, and their characteristic tuft like structure (d), indeed, such as in *in vivo* bronchial epithelium, the cilia growth non in parallel structures, but in small groups of few units [77]. In figure 26e and f the epithelium stratification and tight junction were shown; in particular bronchial epithelium is thin and characterized from just some cellular layers [78], the more external one is very tight, in order to have the barrier function [79, 80] and it is confirmed by very frequent cellular junction.



**Figure 26** Scanning electron microscopy (SEM) top view of bronchial epithelium, ciliate and goblet cells (a-b), cilia structures (d-e), transmission electron microscopy (TEM) section of bronchial epithelium stratification (e) and tight junction (f). scale bar: 1  $\mu\text{m}$  (a-c) 100 nm (d), 2  $\mu\text{m}$  (e), 200 nm (f).

In the figure 27a are shown K14/P63; the red signal of K14 is expressed even after air-liquid interface conditions, in the basal layer, the transcriptional factor p63 is expressed in high proliferative epithelial cells in order to have the normal epithelial turn-over. In 27b the signal of ZO-1, tight junction marker, demonstrates the barrier function of the epithelium.

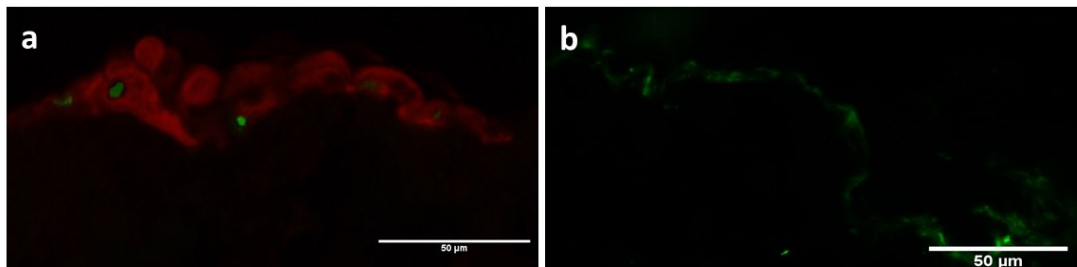


Figure 27 immunofluorescence analysis of histological section with thick 5  $\mu\text{m}$  of human bronchial epithelium; Keratine 14 in red and P63 in green (a); ZO-1 (b)

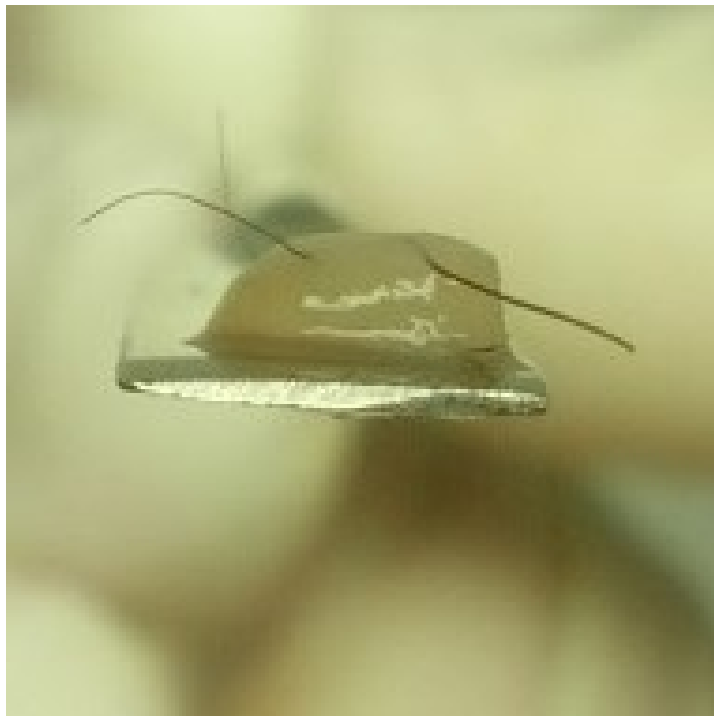
### 3.4 Discussion

In this work we report a full thickness model of lung made up of lung fibroblast embedded in own ECM and bronchial epithelial cells. These epithelia contain columnar cells, secretory goblet cells and non-secretory ciliated epithelial cells [75, 78]. Our model replicates many of the morphological and functional characteristics of the human bronchial epithelium and it is capable of forming a more physiologically relevant representation of lung tissue than culturing cells alone or in 2D systems. The 3D lung model presented in this study successfully supports the culture of multiple cell types, and structurally resemble the native lung ECM. The fibroblasts were well organized in the extracellular matrix, and the epithelial cells proliferated and differentiated to produce a pseudostratified structure. The epithelial cells control the proliferation of bronchial fibroblasts grown in a 3-dimensional model [1]; this supports the hypothesis that the tissue

environment and cell contact are key factors in reproducing *in vitro* the cascade of events that occur *in vivo*. There have been several previous reports describing the co-culture of lung fibroblasts and human bronchial epithelial cells in 3D type-I collagen gels [76, 81]. However, these published models used collagen concentrations that varied widely from 0.715 mg/ml to 2.5 mg/ml [76]. The collagen concentration and composition affected the phenotype of bronchial epithelial cells in 3D culture; on the 1 mg/ml type-I collagen gels, epithelia became stratified compared to HBECs that were cultured on coated Millicell\_inserts [76]. The addition of type-IV collagen generated epithelia that were thicker than when the gels consisted of type-I collagen alone; furthermore, there was a significant positive correlation between collagen concentration and the epithelium thickness [76, 82, 83]. In our model, the endogenous ECM play a key role for well epithelium differentiation, indeed both type-I collagen and of type-IV collagen were detected. The exploration of a 3D bronchial tissue model suggest that it presents an invaluable tool for academic and pharmaceutical research in understanding how epithelial and stromal interactions regulate lung homeostasis and disease, for drug discovery and delivery with the potential of reducing the need for some animal experimentation in this area. In conclusion, using tissue engineering technology, we produced well-organized normal bronchial mucosa tissues.

## Chapter 4

Human skin equivalent maintains exogenous hair  
viability and functionality



# Chapter 4

## 4.1 Introduction

The classical tissue engineering approach to produce viable in vitro tissues by seeding cells into preformed, porous, and biodegradable scaffolds presents several shortcomings, mainly due to the difficulty in reproducing adequate micro-environmental conditions in a three-dimensional (3D) thick structure [5]. Therefore, devising new biomimetic techniques for generating engineered tissues with micrometer-scale resolution is of great scientific interest. Microfabrication technologies have been applied to cell culture techniques in the effort to better direct tissue formation and function [84]. As a result, self-assembling of micrometer-scale tissues in order to create the native microarchitecture of natural tissues is a promising approach for the fabrication of functional complex tissue constructs [6, 85]. Skin substitutes can be used in various fields of skin biology, pharmacotoxicology, cellular and molecular biology studies and also as a replacement for human skin in clinical applications. They are designed (1) to provide a mechanical barrier against infection and fluid loss (burn patients), (2) to close wounds (diabetic ulcers), and (3) to replace animal models for dermatopharmaceutical testing [86, 87]. The skin is the largest organ in mammals and serves as a protective barrier at the interface between the human body and the

surrounding environment. It guards the underlying organs and protects the body against pathogens and microorganisms. Accordingly, it is directly exposed to potentially harmful microbial, thermal, mechanical and chemical influences. In the past 25 years, great efforts have been made to create substitutes that mimic human skin. In skin tissue engineering, various biological and synthetic materials are combined with *in vitro*-cultured cells to generate functional tissues (Fig. 28). However, besides their use as *in vivo* grafts, recently, other applications have emerged for skin substitutes as *in vitro* test systems [89]. Many types of skin substitutes have been developed by different groups [90-92], and they are commercially available as reported in figure 29. These skin substitutes can be classified in two types. The first type consists of keratinocytes seeded on a synthetic or collagen carrier simulating only the human epidermis (epidermal substitutes). The second type consists additionally of a dermal layer of human fibroblasts embedded in various kinds of scaffolds (full-thickness skin substitutes).

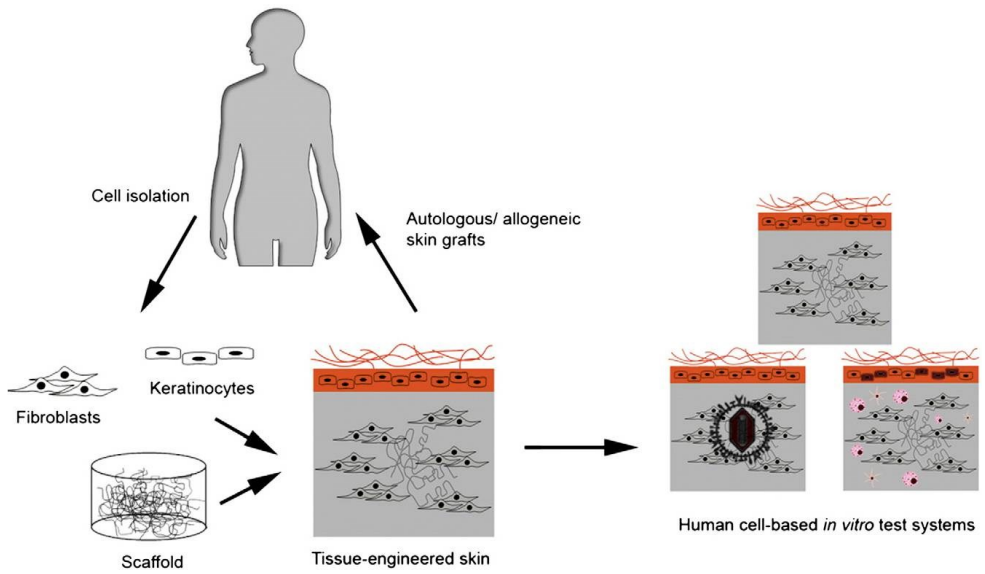


**Figure 28 schematic illustration of principles of skin tissue engineering. Primary eratinocytes and fibroblasts are isolated from human donor tissues, which are then in vitro expanded prior seeding onto suitable scaffold materials/matrices. For a full-thickness skin equivalent, the fibroblasts and the matrix are initially used to establish the dermal part. The keratinocytes are seeded afterwards on the top of the dermis to ultimately form the epidermal part of the skin substitute. The in vitro-engineered skin can serve as skin graft or can be used as human-cell based in vitro test system. Adapted from [92]**

Commercial product	Description
<b>Epidermal substitutes</b>	
BioSeed-S™	Subconfluent autologous keratinocytes on a fibrin matrix
CelliSpray™	Noncultured autologous keratinocyte suspension
Cryoskin™	Cryopreserved monolayer of noncultured allogeneic keratinocytes coating with silicone backing
Epibase	Cultured autologous keratinocytes
Epicef®	Cultured autologous keratinocytes from skin on petrolatum gauze backing
EpideX™	Cultured autologous keratinocytes from the outer root sheath on silicone membrane
Episkin™	Cultured keratinocytes on a collagen matrix
Laserskin™ (Vivoderm™)	Cultured autologous keratinocytes in a matrix of a hyaluronic acid ester
LyphoDerm™	Freeze-dried lysate from cultured allogeneic epidermal keratinocytes into a hydrophilic gel
Myskin™	Cultured autologous keratinocytes seeded on specially treated silicone sheet
ReCell®	Noncultured autologous keratinocyte suspension
Suprathel®	Absorbable, synthetic wound dressing with properties of natural epithelium
<b>Dermal substitutes</b>	
AlloDerm™	Allogeneic acellular dermal matrix
Biobrane™	Porcine collagen chemically bound to silicone/nylon membrane
Cymetra™	Micronized particulate acellular cadaveric dermal matrix
Dermagen	Allogeneic fibroblasts cultured in a collagenous sponge
Dermagraft™	Allogeneic living human-derived fibroblast skin substitute
Dermamatrix	Allogeneic acellular human dermis
EZ-Derm™	Acellular xenogeneic collagen matrix
FortaFlex™	Acellular collagen matrix material derived from porcine small intestine submucosa
Giyaderm®	Acellular human dermis
GraftJacket®	Allogeneic human acellular pre-meshed dermis
Hyalograft 3D™	Autologous dermal substitute including a matrix of a hyaluronic acid ester
ICX-SKN	Allogeneic dermal substitute with human dermal fibroblasts in human collagen matrix
Integra®	Nonliving extracellular matrix of collagen and chondroitin-6-sulfate with silicone backing
Karoderm	Allogeneic human acellular dermis
Matriderm™	Acellular scaffold composed of elastin and collagen types I, III and V
Oasis™	Acellular collagen matrix material derived porcine small intestinal submucosa
Permacol Surgical Implant	Acellular porcine dermis
Repliform™	Acellular cadaveric human dermal allograft
Strattice™	Acellular porcine dermis
SureDerm	Allogeneic acellular human lyophilized dermis
TransCyte™	Polymer membrane and allogeneic neonatal human fibroblast cells on a nylon mesh coated with porcine dermal collagen and bonded to a polymer membrane (silicone)
<b>Bilayer substitutes</b>	
Apligraf®	Allogeneic cultured human keratinocytes and fibroblasts in a bovine collagen sponge
OrCel®	Similar to Apligraf®
PermaDerm™	Autologous keratinocytes seeded onto dermal substitute made with autologous fibroblasts in bovine collagen matrix
PolyActive	Autologous cultured keratinocytes and fibroblasts in elastomeric and biodegradable polyethylene oxide terephthalate/polybutylene terephthalate copolymer
StrataGraft®	Allogeneic dermis and epidermis generated from a progenitor cell line: neonatal immortalized keratinocytes (NIKS®)
TissueTech™	Autologous dermal substitute Hyalograft 3D combined with an autologous epidermal replacement (Laserskin autograft)

Figure 29 Commercially available skin substitutes

In our group the process in order to recreate an human skin equivalent well stratified has been developed. The keratinocytes growth directly on 3D dermis equivalent; during the submerged condition their proliferation is

favorite, while in air-liquid interface condition overbear the differentiation. As shown in figure 30, the resultant epithelium demonstrates a greater degree of tissue architecture and organization (a-c), in particular is possible to distinguish 3 layers: basal layer (cuboidal cell shape), spinous and granulose layer (elongate cell shape) corneal layer (the absence of the cellular nuclei that indicate the keratinization of the cells). Moreover, the very important aspect of this human skin model is the presence of keratinocytes inclusions in the dermis (d-f), this event remembers the embryonal hair follicles development [93]. The keratinocytes inclusions (placode) of the embryonic epidermis was surrounded by a fibroblasts condensation [94]. Reciprocal signaling between the condensate and the placode leads to proliferation of the overlying epithelium and downward extension of the new follicle into the dermis [95]. Such epithelial cyst like inclusions present in dermal portion contained keratinocytes; the condensate changes its shape, starting from a spheroidal aggregate it polarize during the time. This cysts in terms of shape and organization can be considerate an hair bulb precursor. We hypothesized that the microenvironment that we are able to recreate, represents an optimal soil in which hair follicle-like structure can be recapitulated. As consequence in this chapter we use the conclusions of the previous work [93] as starting point to evaluate the capability of our model to recreate a suitable environment for exogenous hair maintenance.

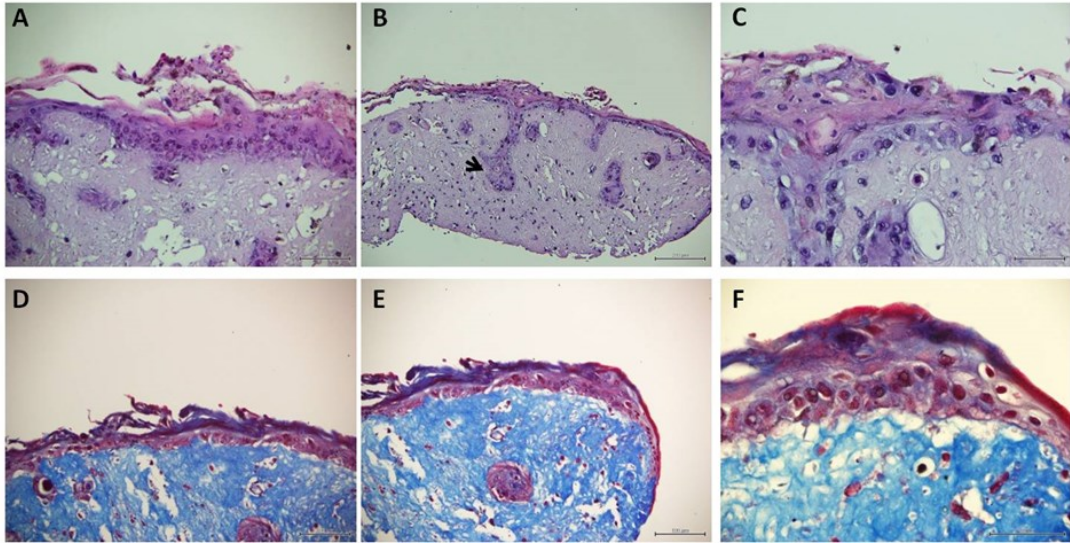


Figure 30 histological analysis of cross section of human skin equivalent with endogenous dermis. (A, B,C) hematoxylin and eosin staining and introction of basal layer was indicated by black arrow ; (D,E,F) Masson trichromic staining. Adapted from [97].

## 4.2 Materials and Methods

### 4.2.1 Microscaffold production

Gelatin porous microbeads (GPMs) have been prepared according to a modified double emulsion technique (O/W/O). Gelatin (type B Sigma Aldrich Chemical Company, Bloom 225, Mw=1 76654 Dalton) was dissolved into 10 ml of water. Beads of gelatin containing droplets of toluene were produced through the addition of excess toluene (30 ml) that allowed for a double emulsion (O/W/O). The resulting

microspheres were filtered and washed with acetone and then dried at room temperature. Microspheres were separated selectively by using commercial sieves (Sieves IG/3-EXP, Retsch, Germany). GPMs with 75-150  $\mu\text{m}$  size range were recovered and further processed. GPMs have been stabilized by means of chemical treatment with glyceraldehyde (GAL), in order to make them stable in aqueous environment at body temperature. In particular, GPMs were dispersed into an acetone/water solution containing 4% of GAL and mixed at 4°C for 24 h. Then microspheres were filtered and washed with acetone and dried at room temperature. Before their use in cell culture dry GPM were sterilized by absolute ethanol sub-immersion for 24h. After that, in order to remove ethanol completely, several washings in calcium-free and magnesium-free phosphate-buffered saline (PBS) were performed. Before cell seeding PBS was removed and replaced with the culture medium.

#### **4.2.2 Cell expansion**

Human dermal fibroblasts (neonatal HDF 106-05n ECACC) were sub-cultured onto 150  $\text{mm}^2$  Petri dishes in culture medium (Eagle's BSS Minimum Essential Medium containing 20% fetal bovine serum, 100  $\mu\text{g}/\text{mL}$  L-glutamine, 100 U/mL penicillin/streptomycin, and 0,1 mM Non

Essential Amino Acids). Cells were maintained at 37°C in humidified atmosphere containing 5% CO<sub>2</sub>. HDF of passages 4-7 were used

### **4.2.3 HD-μTP culture**

To realize the HD-μTP, spinner flask bioreactor was inoculated with 10<sup>5</sup>cell\*ml<sup>-1</sup> and 2mg\*ml<sup>-1</sup> of microbeads, corresponding to 10 cells per bead. The culture suspension was stirred intermittently at 30 rpm (5 min stirring and 30 min static incubation) for the first 6h post-inoculation for cell adhesion, and then continuously agitated at 30 rpm up to 28 days. The growth medium was replenished on the first day and every 2 days until the end of experiments. From the day 4<sup>th</sup>, 50μg/ml of ascorbic acid (l-ascorbic acid Sigma A-5960) were added and freshly added at each medium change.

### **4.2.4 Hair follicle extraction**

Human hair were obtained from scalp with terminal hair follicles in anagen phase of the hair growth cycle. Individual hair follicles are isolated by using a fine tweezers in order to draw out the hair follicles via clasping the protruding upper hair follicle. Each hair follicle was observed with stereomicroscope, only hair follicles depicting the morphology of anagen

hair follicles were collected, any damaged follicles or follicles with morphologic features of non-growing catagen or telogen hair follicles were discarded. The isolated hair follicles are collected in quick succession into cell culture dish for 24h into EMEM (Lonza) containing 20% fetal bovine serum, 100 mg/mL L-glutamine, 100 U/mL penicillin/streptomycin, and 0,1 mM Non Essential Amino Acids, 25 mg/mL amphotericin b 5 µg/mL gentamicin, and placed in incubator.

#### **4.2.5 Realization of 3D Human dermis equivalent with hair**

Tissue precursors obtained as described in 3.2.3 section, have been injected in maturation chamber to allow their molding in disc-shaped construct (1 mm in thickness, 5 mm in diameter), filled the mold same hair follicles were placed inside the mold using a PMMA grid with holes of 500 µm and distance between two centers of 1 mm. After 4 weeks of culture, under dynamic conditions, the bio-hybrid obtained has been removed from the maturation chamber and seeded with keratinocytes in order to obtain the epithelial layer.

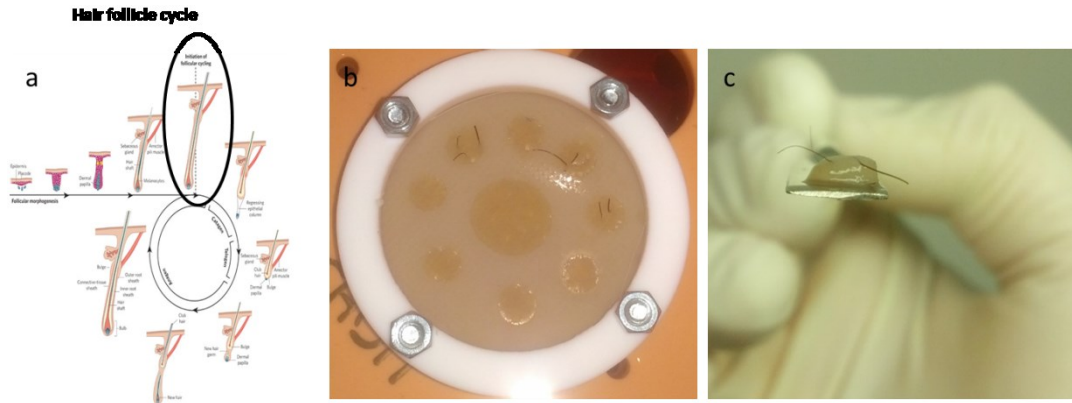


**Figure 31** hair follicle cycle (a); hair implantation inside the maturation chamber (b) and 3D dermis equivalent with hair after two weeks of maturation time (c)

## 4.2.6 Keratinocyte extraction from foreskin

Skin sample derived from reduction surgery with the informed consent of the patient. Rinse the biopsy 3 times with PBS, remove fat from the bottom side, rinse with PBS again, till the PBS stays clear. Cut skin into strips of about 3mm width, incubate it with Dispase solution (2U/mL; about 5-10 ml for 6cm<sup>2</sup> of skin) over night for 16h to 18h at 4°C. Remove the Dispase solution and rinse with PBS, separate epidermis from dermis with tweezers, store both parts separately in two petri dishes. Wash epidermal parts with PBS and transfer pieces into the tube, incubate with Trypsin/EDTA for 5 min at 37°C. In order to stop the enzymatic reaction add 1 mL FBS. Resuspend the solution for 5 min in order to separate cell clusters and strain solution by using a 100µm filter. After centrifugation (5 min 1200 rpm) the solution was

suspended in fresh culture medium (KBM + supplementary mix lonza) and seed to recommended density of  $8 \times 10^3$  cells per  $\text{cm}^2$ .

#### **4.2.7 Realization of human skin equivalent**

The 3D dermis equivalent was accommodate on transwell insert (corning), coated by 20 $\mu\text{l}$  of human fibronectin solution (Sigma Aldrich) to final concentration of 50  $\mu\text{g/ml}$  and let dry to air for 45 minutes at room temperature. Wash the keratinocyte with PBS/EDTA 0.01M, trypsinize keratinocyte colonies with trypsin/EDTA for 5 min at  $37^\circ\text{C}$  to obtain a single cell suspension. Centrifuge at 1200 rpm for 5 min, gently resuspend high density keratinocytes in fresh medium, seed 200,000 cells/dermis equivalent and incubate at  $37^\circ\text{C}$  for 60 min. In order to stimulate the cell proliferation, during the first week the 3D skin equivalent were cultured in submerged condition, while to favorite the differentiation during second and third week were cultured in air liquid interface condition. For submerged culture the KGM was added both on the top and on the bottom of the transwell, while for air liquid interface condition the KGM medium without EGF and PTB but with  $\text{CaCl}_2$  concentration of 1.88 mM was added only on the bottom of the polycarbonate membrane.

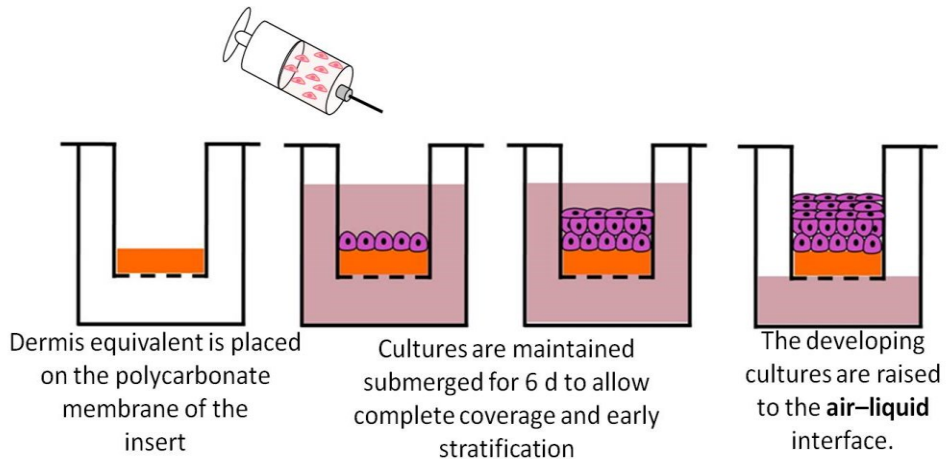


**Figure 32 schematic procedure for human skin equivalent realization**

#### **4.2.8 Immunofluorescence, multiphoton imaging and histology on biohybrids**

For all the analyses, the biohybrids were fixed with 4% paraformaldehyde for 20 min at room temperature, rinsed twice with PBS buffer, After that, the samples were imaged under multichanneled Leica TCS SP5 II coupled with a Multiphoton Microscope where the NIR femtosecond laser beam was derived from a tunable compact mode-locked titanium: sapphire laser (Chameleon Compact OPO-Vis, Coherent). Two-photon excited fluorescence ( $\lambda_{ex} = 840\text{nm}$ ) was used to induce second harmonic generation (SHG) of unstained neo-synthesized collagen structures by collecting the emission wavelength in the range  $\lambda_{em} = 420 \pm 5 \text{ nm}$ . For histological analysis, the biohybrids were fixed in a solution of 10% neutral buffered formalin for 24 h, dehydrated in an incremental series of alcohol (75%, 85%, 95% and

100%, and 100% again, each step 20 min at room temperature) treated with xylene and then embedded in paraffin. Successively, the samples were sectioned at a thickness of 6µm, and stained with hematoxylin and eosin and masson trichrome. The sections were mounted with Histomount Mounting Solution (INVITROGEN) on coverslips and the morphological features of constructs were observed with a light microscope (Olympus, BX53). Furthermore, deparaffined 6 µm sections were immune-stained by using CD133 and Versican; they were performed using Anti-CD 133 monoclonal antibody (dilution 1:500; Miltenyi Biotec), Anti-versican polyclonal antibody (dilution 1:500; Abcam), respectively as primary antibody and Alexa fluor 488 and Alexa fluor 568 respectively as secondary antibody.

#### **4.2.9 Hair elongation measurement**

Hair elongation measurement were been performed in four condition: Only medium, fibroblast conditioned medium, collagen + fibroblast, Biohybrid. For all the experimental configurations the hairs were extracted as described in the section 3.2.4, and placed in sterilizing solution for 24h, and starting from the second day the total number of hairs were divided per four experimental configurations. The first and second groups have been placed in a low

attachment petri dish (corning) covered with freshly and fibroblast preconditioned EMEM (lonza) containing 20% fetal bovine serum, 100 mg/mL L-glutamine, 100 U/mL penicillin/streptomycin, and 0,1 mM Non Essential Amino Acids respectively. The third and fourth groups were placed in a cellularised (400000 cells/ml) rat tail collagen (2.4 mg/ml IBIDI), 3D dermis equivalent respectively. All the samples were monitored during 17 days and the medium was exchanged every 3 days; the images were acquired by stereomicroscope (OLYMPUS SZ) and the hairs length were measured by imagej software using analyze particle plugin.

## 4.3 Results

### 4.3.1 Morphological analysis of dermis equivalent

The image 33 shows a cross section of 4% biohybrid. The histological images (a-b-d-e) concerning human dermis equivalent show the collagen (in blue) along the whole thickness of the sample (1mm), no necrotic region are visible and the microbeads are not more present. The fibroblasts are completely immerse in own extracellular matrix and the elongated nuclear morphology underlines the good condition of the cells. It is interesting to highlight that after 4 weeks of culture time the tissue is completely made-up of endogenous ECM. The presence of collagen (c-f), suggest that the cells not only proliferated but also work correctly, like *in vivo* dermal fibroblasts by secreting and remodeling collagen. Moreover the close interdependence of matrix remodeling, mechanical properties and shape retention is fundamental to preserve the integrity in soft tissue [96].

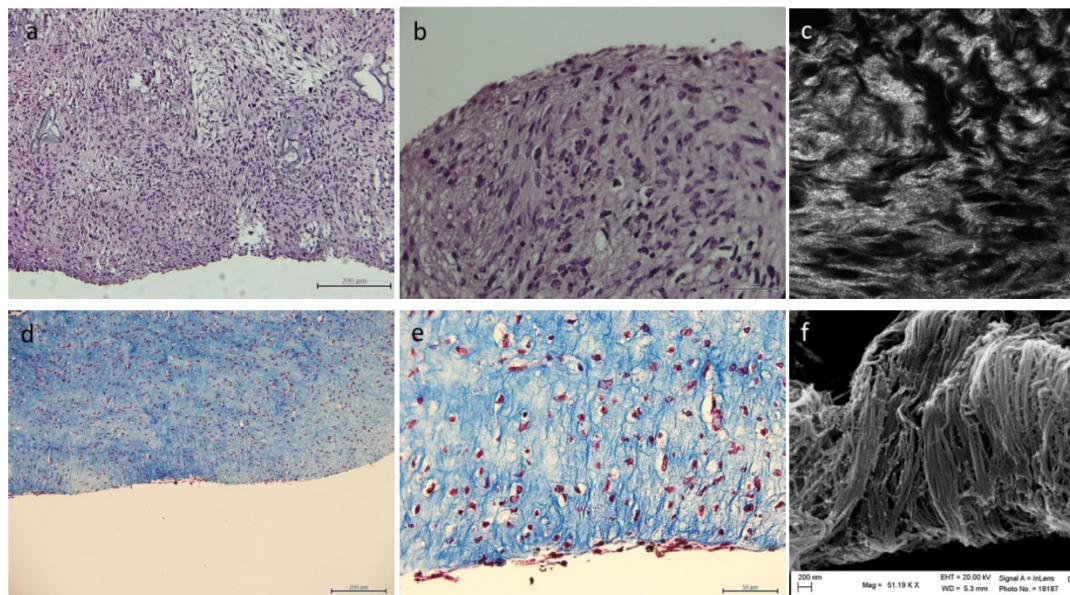


**Figure 33** H/E staining (a-b) and masson trichrome staining (d-e) of biohybrid with 4 weeks of maturation; scale bar 200  $\mu\text{m}$  (a-d) and 50  $\mu\text{m}$  (d-e); collagen signal acquired by SHG MP microscopy (c) and SEM image (f)

### 4.3.2 Hair elongation

The images 35 show the hair elongation in our *in vitro* model, in particular at  $t_0$  the exogenous hair was placed into biohybrid and no external hair shaft is visible. Just after two days of culture few microns of external shaft are visible, and a consistent elongation persists for 17 days still. The graph reports the hair elongation tested in four several condition: fresh medium (I), conditioned medium (II), exogenous collagen with cells (III) and biohybrid (IV). During the first two days, for all the culture condition the elongation values presents the same values of about 6%; while in the next time points the results drastically change. For the (I) condition the final hair shaft is of about 10% more of the initial value, with a consistent decrease of the elongation rate; same trend is seen in the (II) experiment, with a final elongation percent of 11%. The collagen and cells (III) reaches the 15% more of the initial length, showing the same trend of (I) and (II) from rate elongation point of view. The better results were obtained into the biohybrid, in which the final elongation is of about 35%, showing a constant elongation rate during culture time.

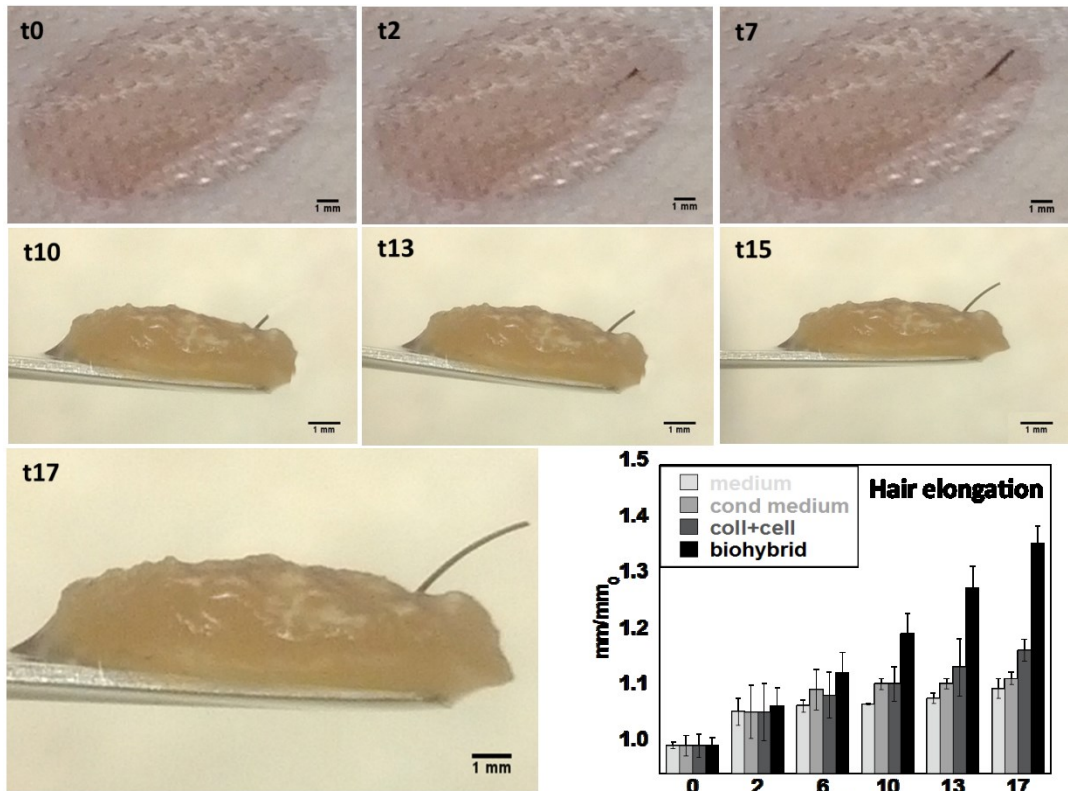


Figure 34 hair elongation during maturation time; quantification of hair elongation in fresh medium, condizionated medium, exogenous collagen and cells, biohybrid

The figure 36 shows the dermis equivalent with implanted exogenous hair (a), the h/e staining (b-c) shows the complete model of human skin equivalent whit implanted exogenous hair; the exogenous hair is ECM surrounded, and the model is able to sustain the external shaft portion. The hair bulbs (d-f) keep their structure, DP cells are well visible both in immune-staining Versican signal and in H/E staining on the bottom of the bulb. The inner and outer sheaths made of keratinocytes layers are preserved during the trials time (d-f).

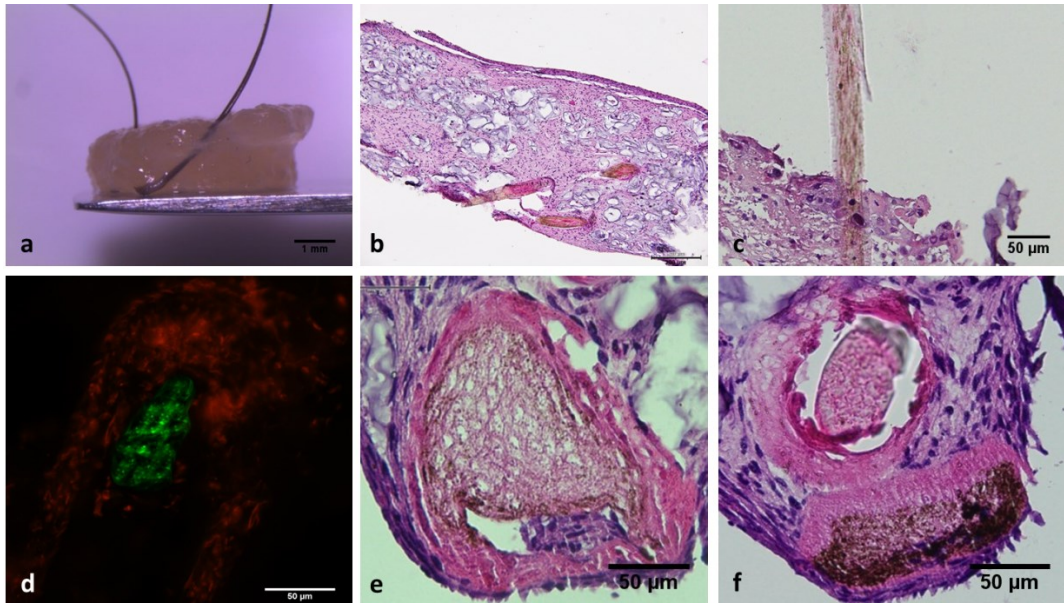


Figure 35 biohybrid with exogenous hair (a); H/E staining of human skin equivalent with hair implantation (b-c); immunofluorescence analysis of hair follicle, Versican in green and CD133 in red; H/E staining of exogenous hair bulb (e-f); scale bar 1mm (a), 200  $\mu\text{m}$  (b), 50  $\mu\text{m}$  (c-f)

## 4.4 Discussion

The goal of this study is to develop skin substitutes with greater homology to native skin, in terms of dermis layer, extra cellular matrix, epidermal differentiated layer, and hair follicles. The dermis part is totally made of fibroblast and own ECM [13], the keratinocytes are seeded directly on the dermis part, and they are able to differentiate in all the three layers, basal layer, spinous and granulose layer, corneal layer [97, 98]. The hair follicle morphogenesis is mediated by the crosstalk between mesenchymal cells

(fibroblasts) and epithelial cells (keratinocytes) [99-103], this kind of interaction is an essential feature of hair follicle formation. In our complete model the crosstalk between fibroblasts and keratinocytes leads to a cysts like formation that can be considerate as hair follicle precursors. Moreover, in order to obtain a complete hair follicle structure (inner and outer sheaths, hair shaft), a lot of biochemical stimuli are needed, growth factors, cytokines, hormones and other factors too [104]. This great number of stimuli, could be the explanation why in our human skin equivalent just hair follicle precursors are visible, indeed in literature many works overcome this problem by the *in vivo* implantation [105-107]. The introduction of anagen hairs in our 3D human skin equivalent, demonstrates the relevance of the endogenous ECM. The mature hair follicles are able to growth in several kind of conditions, fresh medium, conditioned medium, in exogenous ECM and fibroblasts [108-110]; we demonstrate that inside the biohybrid they find an environment much more similar to the *in vivo* skin, indeed they keep on the own elongation capability during time; the DP cells signal confirms that they remain undifferentiated, and so able to recreate a new follicle . In the hair follicles, after a variable period of time, anagen phase end, follicle growth stop, and catagen phase begins [111]; the first sign of regression in the catagen follicle is the withdrawal of papilla cells from the basement membrane [104]. The implanted hairs in human skin equivalent model, are all in anagen phase (dauration of 2-7 years [104]); if it was possible to

extend the experiment until to a complete hair cycle, the DP cells migration and the restart of the cycle will happen inside the 3D model; this could lead to an hair follicle regeneration just in our human skin equivalent. Following this not confirmed hypothesis, thanks to surrounding environment, we could recreate a complete hair follicle inside the 3D model, by using a complete hair follicle as vector for the DP cells. The goal of this work is validate the endogenous ECM, synthesized, assembled and remodeled by cells, which, in turns, are regulated and controlled by ECM. This better environment is able to recreate an “*in vivo* like” tissue conditions, that accommodate the crosstalk between several cellular lines, and support the exogenous hair elongation, and, in future, the complete hair regeneration.

# Conclusion

The results described in this thesis work, show a process able to obtain bioengineered micro tissues with endogenous ECM, that can be used as functional units both in micrometric and macrometric scale. This new class of  $\mu$ tp can be queried in order to study the effects of drugs or external stimuli on the equivalent tissue; they can be printed in different shape, overcoming the shape limits related to of preformed scaffold, thanks to versatility of the bottom-up process. This printing process leads to an ECM deposition and remodeling, that make the realized tissues very similar to native organs. The endogenous ECM allows a great degree of organization and is possible to recreate *in vitro* the complexity of native tissue, in terms of epithelium stratification, structures reconstruction etc. This technique is applicable to several kind of cell lines, in order to obtain several kind of tissues, each one with its specific characteristic and morphology; whereby, the final 3D tissue equivalent, represent an important tool for researcher in order to better understand the biology of the tissues.

# REFERENCES

1. Chakir, J., et al., *Bronchial mucosa produced by tissue engineering: a new tool to study cellular interactions in asthma*. Journal of allergy and clinical immunology, 2001. **107**(1): p. 36-40.
2. Gomez-Lechon, M., et al., *In vitro evaluation of potential hepatotoxicity induced by drugs*. Current pharmaceutical design, 2010. **16**(17): p. 1963-1977.
3. Lu, T., Y. Li, and T. Chen, *Techniques for fabrication and construction of three-dimensional scaffolds for tissue engineering*. International journal of nanomedicine, 2013. **8**: p. 337.
4. Shi, J., et al., *Nanotechnology in drug delivery and tissue engineering: from discovery to applications*. Nano letters, 2010. **10**(9): p. 3223-3230.
5. Yu, H., D. Wang, and M.-Y. Han, *Top-down solid-phase fabrication of nanoporous cadmium oxide architectures*. Journal of the American Chemical Society, 2007. **129**(8): p. 2333-2337.
6. Nichol, J.W. and A. Khademhosseini, *Modular tissue engineering: engineering biological tissues from the bottom up*. Soft matter, 2009. **5**(7): p. 1312-1319.
7. Urciuolo, F., et al., *Novel strategies to engineering biological tissue in vitro*, in *Nanotechnology in Regenerative Medicine*. 2012, Springer. p. 223-244.
8. Stella, J.A., et al., *On the biomechanical function of scaffolds for engineering load-bearing soft tissues*. Acta biomaterialia, 2010. **6**(7): p. 2365-2381.
9. Chen, M., et al., *A modular approach to the engineering of a centimeter-sized bone tissue construct with human amniotic mesenchymal stem cells-laden microcarriers*. Biomaterials, 2011. **32**(30): p. 7532-7542.
10. Rivron, N.C., et al., *Tissue assembly and organization: developmental mechanisms in microfabricated tissues*. Biomaterials, 2009. **30**(28): p. 4851-4858.
11. Du, Y., et al., *Sequential assembly of cell-laden hydrogel constructs to engineer vascular-like microchannels*. Biotechnology and bioengineering, 2011. **108**(7): p. 1693-1703.
12. Gauvin, R. and A. Khademhosseini, *Microscale technologies and modular approaches for tissue engineering: moving toward the fabrication of complex functional structures*. Acs Nano, 2011. **5**(6): p. 4258-4264.
13. Imparato, G., et al., *The role of microscaffold properties in controlling the collagen assembly in 3D dermis equivalent using modular tissue engineering*. Biomaterials, 2013. **34**(32): p. 7851-7861.
14. Bronzino, J.D. and D.R. Peterson, *Tissue engineering and artificial organs*. 2010: CRC press.
15. Griffith, L.G. and G. Naughton, *Tissue engineering--current challenges and expanding opportunities*. science, 2002. **295**(5557): p. 1009-1014.
16. Cukierman, E., R. Pankov, and K.M. Yamada, *Cell interactions with three-dimensional matrices*. Current opinion in cell biology, 2002. **14**(5): p. 633-640.

17. Rosso, F., et al., *Smart materials as scaffolds for tissue engineering*. Journal of cellular physiology, 2005. **203**(3): p. 465-470.
18. Lang, M., *Systems for the automated 3D assembly of micro-tissue and bio-printing of tissue engineered constructs*. 2012.
19. Geckil, H., et al., *Engineering hydrogels as extracellular matrix mimics*. Nanomedicine, 2010. **5**(3): p. 469-484.
20. Morgan, J.R., D. Dean, and A. Rago, *Assays and methods for fusing cell aggregates to form proto-tissues*. 2013, Google Patents.
21. Matsunaga, Y.T., Y. Morimoto, and S. Takeuchi, *Molding cell beads for rapid construction of macroscopic 3D tissue architecture*. Advanced Materials, 2011. **23**(12): p. H90-H94.
22. Kumachev, A., *Generation of Cell-laden Biopolymer Microgels with Tunable Mechanical Properties for Cancer Cell Studies*. 2012.
23. Park, S.J., et al., *Synthesis and Dispersion Characteristics of Multi-Walled Carbon Nanotube Composites with Poly (methyl methacrylate) Prepared by In-Situ Bulk Polymerization*. Macromolecular Rapid Communications, 2003. **24**(18): p. 1070-1073.
24. Cornbrooks, C., et al., *In vivo and in vitro observations on laminin production by Schwann cells*. Proceedings of the National Academy of Sciences, 1983. **80**(12): p. 3850-3854.
25. John, A. and G. Tuszynski, *The role of matrix metalloproteinases in tumor angiogenesis and tumor metastasis*. Pathology oncology research, 2001. **7**(1): p. 14-23.
26. Sanes, J.R., *Roles of extracellular matrix in neural development*. Annual review of physiology, 1983. **45**(1): p. 581-600.
27. Ingber, D.E., *Cellular mechanotransduction: putting all the pieces together again*. The FASEB journal, 2006. **20**(7): p. 811-827.
28. Basson, M.D., I.M. Modlin, and J. Madri, *Human enterocyte (Caco-2) migration is modulated in vitro by extracellular matrix composition and epidermal growth factor*. Journal of Clinical Investigation, 1992. **90**(1): p. 15.
29. Madri, J.A., et al., *Effects of soluble factors and extracellular matrix components on vascular cell behavior in vitro and in vivo: Models of de-endothelialization and repair*. Journal of cellular biochemistry, 1991. **45**(2): p. 123-130.
30. Gospodarowicz, D., D. Delgado, and I. Vlodavsky, *Permissive effect of the extracellular matrix on cell proliferation in vitro*. Proceedings of the National Academy of Sciences, 1980. **77**(7): p. 4094-4098.
31. Ozbolat, I.T., *Bioprinting Technology: A Current State-of-the-Art*. Journal of Manufacturing Science and Engineering, 2014. **136**: p. 061016-1.
32. Fedorovich, N.E., et al., *Hydrogels as extracellular matrices for skeletal tissue engineering: state-of-the-art and novel application in organ printing*. Tissue engineering, 2007. **13**(8): p. 1905-1925.
33. Chang, C.C., et al., *Direct-write bioprinting three-dimensional biohybrid systems for future regenerative therapies*. Journal of Biomedical Materials Research Part B: Applied Biomaterials, 2011. **98**(1): p. 160-170.

34. Tseng, Y., T.P. Kole, and D. Wirtz, *Micromechanical mapping of live cells by multiple-particle-tracking microrheology*. Biophysical journal, 2002. **83**(6): p. 3162-3176.
35. Rich, L. and P. Whittaker, *Collagen and picosirius red staining: a polarized light assessment of fibrillar hue and spatial distribution*. Braz J Morphol Sci, 2005. **22**(2): p. 97-104.
36. Whittaker, P., et al., *Quantitative assessment of myocardial collagen with picosirius red staining and circularly polarized light*. Basic research in cardiology, 1994. **89**(5): p. 397-410.
37. Raub, C., et al., *Predicting bulk mechanical properties of cellularized collagen gels using multiphoton microscopy*. Acta biomaterialia, 2010. **6**(12): p. 4657-4665.
38. Raub, C.B., et al., *Image correlation spectroscopy of multiphoton images correlates with collagen mechanical properties*. Biophysical journal, 2008. **94**(6): p. 2361-2373.
39. Hynes, R.O., *The extracellular matrix: not just pretty fibrils*. Science, 2009. **326**(5957): p. 1216-1219.
40. Ashe, K.M., et al., *BIOMIMETIC MATRICES FOR INTEGRIN-MEDIATED CELL ADHESION*. 2010: World Scientific Publishing Co., Singapore.
41. Seal, B., T. Otero, and A. Panitch, *Polymeric biomaterials for tissue and organ regeneration*. Materials Science and Engineering: R: Reports, 2001. **34**(4): p. 147-230.
42. Khademhosseini, A. and R. Langer, *Microengineered hydrogels for tissue engineering*. Biomaterials, 2007. **28**(34): p. 5087-5092.
43. Kotobuki, N., et al., *Cultured autologous human cells for hard tissue regeneration: preparation and characterization of mesenchymal stem cells from bone marrow*. Artificial organs, 2004. **28**(1): p. 33-39.
44. Jakab, K., et al., *Tissue engineering by self-assembly and bio-printing of living cells*. Biofabrication, 2010. **2**(2): p. 022001.
45. Pizzo, A.M., et al., *Extracellular matrix (ECM) microstructural composition regulates local cell-ECM biomechanics and fundamental fibroblast behavior: a multidimensional perspective*. Journal of applied physiology, 2005. **98**(5): p. 1909-1921.
46. Huh, D., et al., *Microengineered physiological biomimicry: organs-on-chips*. Lab on a chip, 2012. **12**(12): p. 2156-2164.
47. Ramadan, Q., et al., *NutriChip: nutrition analysis meets microfluidics*. Lab on a Chip, 2013. **13**(2): p. 196-203.
48. Sikavitsas, V.I., G.N. Bancroft, and A.G. Mikos, *Formation of three-dimensional cell/polymer constructs for bone tissue engineering in a spinner flask and a rotating wall vessel bioreactor*. Journal of biomedical materials research, 2002. **62**(1): p. 136-148.
49. Meinel, L., et al., *Bone tissue engineering using human mesenchymal stem cells: effects of scaffold material and medium flow*. Annals of biomedical engineering, 2004. **32**(1): p. 112-122.

50. Bancroft, G.N., V.I. Sikavitsas, and A.G. Mikos, *Technical note: Design of a flow perfusion bioreactor system for bone tissue-engineering applications*. Tissue engineering, 2003. **9**(3): p. 549-554.
51. Zhao, F. and T. Ma, *Perfusion bioreactor system for human mesenchymal stem cell tissue engineering: dynamic cell seeding and construct development*. Biotechnology and bioengineering, 2005. **91**(4): p. 482-493.
52. Sodian, R., et al., *Tissue-engineering bioreactors: a new combined cell-seeding and perfusion system for vascular tissue engineering*. Tissue engineering, 2002. **8**(5): p. 863-870.
53. Polini, A., et al., *Organs-on-a-chip: a new tool for drug discovery*. Expert opinion on drug discovery, 2014. **9**(4): p. 335-352.
54. Ramadan, Q. and M.A. Gijs, *In vitro micro-physiological models for translational immunology*. Lab on a Chip, 2015.
55. Ni, M., et al., *Cell culture on MEMS platforms: A review*. International journal of molecular sciences, 2009. **10**(12): p. 5411-5441.
56. Kim, L., et al., *A practical guide to microfluidic perfusion culture of adherent mammalian cells*. Lab on a Chip, 2007. **7**(6): p. 681-694.
57. Zhang, C., *Perfusion culture of mammalian cells in a microfluidic channel with a built-in pillar array*, in *Single-Cell Analysis*. 2012, Springer. p. 83-94.
58. Kim, L.Y., *Microfluidic perfusion culture for controlling the stem cell microenvironment*. 2008, Massachusetts Institute of Technology.
59. Chan, D., et al., *Regulation of procollagen synthesis and processing during ascorbate-induced extracellular matrix accumulation in vitro*. Biochem. J, 1990. **269**: p. 175-181.
60. Peterkofsky, B., *The effect of ascorbic acid on collagen polypeptide synthesis and proline hydroxylation during the growth of cultured fibroblasts*. Archives of biochemistry and biophysics, 1972. **152**(1): p. 318-328.
61. Robertson, W.v.B. and B. Schwartz, *Ascorbic acid and the formation of collagen*. Journal of Biological Chemistry, 1953. **201**(2): p. 689-696.
62. Hata, R.I. and H. Senoo, *L-ascorbic acid 2-phosphate stimulates collagen accumulation, cell proliferation, and formation of a three-dimensional tissuelike substance by skin fibroblasts*. Journal of cellular physiology, 1989. **138**(1): p. 8-16.
63. Gould, B.S. and J.F. Woessner, *BIOSYNTHESIS OF COLLAGEN THE INFLUENCE OF ASCORBIC ACID ON THE PROLINE, HYDROXYPROLINE, GLYCINE, AND COLLAGEN CONTENT OF REGENERATING GUINEA PIG SKIN*. Journal of Biological Chemistry, 1957. **226**(1): p. 289-300.
64. Vogel, V. and M.P. Sheetz, *Cell fate regulation by coupling mechanical cycles to biochemical signaling pathways*. Current opinion in cell biology, 2009. **21**(1): p. 38-46.
65. Kvietys, P.R. and D.N. Granger, *Endothelial cell monolayers as a tool for studying microvascular pathophysiology*. American Journal of Physiology-Gastrointestinal and Liver Physiology, 1997. **273**(6): p. G1189-G1199.

66. Minuth, W.W., M. Sittinger, and S. Kloth, *Tissue engineering: generation of differentiated artificial tissues for biomedical applications*. Cell and tissue research, 1997. **291**(1): p. 1-11.
67. Babu, M., *Collagen based dressings—a review*. Burns, 2000. **26**(1): p. 54-62.
68. Schulz Iii, J., R. Tompkins, and J. Burke, *Artificial skin*. Annual review of medicine, 2000. **51**(1): p. 231-244.
69. Vaughan, M.B., et al., *A three-dimensional model of differentiation of immortalized human bronchial epithelial cells*. Differentiation, 2006. **74**(4): p. 141-148.
70. Ramirez, R.D., et al., *Immortalization of human bronchial epithelial cells in the absence of viral oncoproteins*. Cancer research, 2004. **64**(24): p. 9027-9034.
71. Forbes, B., *Human airway epithelial cell lines for in vitro drug transport and metabolism studies*. Pharmaceutical science & technology today, 2000. **3**(1): p. 18-27.
72. Puchelle, E., et al., *Airway epithelial repair, regeneration, and remodeling after injury in chronic obstructive pulmonary disease*. Proceedings of the American Thoracic Society, 2006. **3**(8): p. 726-733.
73. Ghaemmaghami, A.M., et al., *Biomimetic tissues on a chip for drug discovery*. Drug Discovery Today, 2012. **17**(3): p. 173-181.
74. Harrington, H., et al., *Immunocompetent 3D Model of Human Upper Airway for Disease Modeling and In Vitro Drug Evaluation*. Molecular pharmaceutics, 2014. **11**(7): p. 2082-2091.
75. Tam, A., et al., *The airway epithelium: more than just a structural barrier*. Therapeutic advances in respiratory disease, 2011. **5**(4): p. 255-273.
76. Pageau, S.C., et al., *The effect of stromal components on the modulation of the phenotype of human bronchial epithelial cells in 3D culture*. Biomaterials, 2011. **32**(29): p. 7169-7180.
77. Crystal, R.G., et al., *Airway epithelial cells: current concepts and challenges*. Proceedings of the American Thoracic Society, 2008. **5**(7): p. 772-777.
78. FRANKE, W.W., et al., *Identification and characterization of epithelial cells in mammalian tissues by immunofluorescence microscopy using antibodies to prekeratin*. Differentiation, 1979. **15**(1-3): p. 7-25.
79. Knight, D.A. and S.T. Holgate, *The airway epithelium: structural and functional properties in health and disease*. Respirology, 2003. **8**(4): p. 432-446.
80. Xiao, C., et al., *Defective epithelial barrier function in asthma*. Journal of Allergy and Clinical Immunology, 2011. **128**(3): p. 549-556. e12.
81. Mondrinos, M.J., et al., *Engineering three-dimensional pulmonary tissue constructs*. Tissue engineering, 2006. **12**(4): p. 717-728.
82. Hoshino, M., et al., *Bronchial subepithelial fibrosis and expression of matrix metalloproteinase-9 in asthmatic airway inflammation*. Journal of allergy and clinical immunology, 1998. **102**(5): p. 783-788.
83. Boulet, L.-P., et al., *Bronchial subepithelial fibrosis correlates with airway responsiveness to methacholine*. CHEST Journal, 1997. **112**(1): p. 45-52.

84. Andersson, H. and A. Van Den Berg, *Microfabrication and microfluidics for tissue engineering: state of the art and future opportunities*. Lab Chip, 2004. **4**(2): p. 98-103.
85. Leong, K., et al., *Engineering functionally graded tissue engineering scaffolds*. Journal of the mechanical behavior of biomedical materials, 2008. **1**(2): p. 140-152.
86. MacNeil, S., *Progress and opportunities for tissue-engineered skin*. Nature, 2007. **445**(7130): p. 874-880.
87. Someya, T., et al., *A large-area, flexible pressure sensor matrix with organic field-effect transistors for artificial skin applications*. Proceedings of the National Academy of Sciences of the United States of America, 2004. **101**(27): p. 9966-9970.
88. Palmiero, C., et al., *Engineered dermal equivalent tissue in vitro by assembly of microtissue precursors*. Acta biomaterialia, 2010. **6**(7): p. 2548-2553.
89. Fernandes, H., et al., *Extracellular matrix and tissue engineering applications*. Journal of Materials Chemistry, 2009. **19**(31): p. 5474-5484.
90. Boehnke, K., et al., *Effects of fibroblasts and microenvironment on epidermal regeneration and tissue function in long-term skin equivalents*. European journal of cell biology, 2007. **86**(11): p. 731-746.
91. Groeber, F., et al., *Skin tissue engineering—in vivo and in vitro applications*. Advanced drug delivery reviews, 2011. **63**(4): p. 352-366.
92. Roguet, R., *Use of skin cell cultures for in vitro assessment of corrosion and cutaneous irritancy*. Cell biology and toxicology, 1999. **15**(1): p. 63-75.
93. Casale, C., *3D COMPLEX ENDOGENOUS TISSUE EQUIVALENT IN VITRO: PROCESSING AND BIOTECHNOLOGICAL APPLICATION*. 2013.
94. Inamatsu, M., et al., *Embryonic dermal condensation and adult dermal papilla induce hair follicles in adult glabrous epidermis through different mechanisms*. Development, growth & differentiation, 2006. **48**(2): p. 73-86.
95. Driskell, R.R., et al., *Hair follicle dermal papilla cells at a glance*. Journal of cell science, 2011. **124**(8): p. 1179-1182.
96. Grinnell, F., *Fibroblast biology in three-dimensional collagen matrices*. Trends in cell biology, 2003. **13**(5): p. 264-269.
97. Bierkamp, C., et al., *Embryonic heart and skin defects in mice lacking plakoglobin*. Developmental biology, 1996. **180**(2): p. 780-785.
98. Härle-Bachor, C. and P. Boukamp, *Telomerase activity in the regenerative basal layer of the epidermis in human skin and in immortal and carcinoma-derived skin keratinocytes*. Proceedings of the National Academy of Sciences, 1996. **93**(13): p. 6476-6481.
99. Schneider, M.R., R. Schmidt-Ullrich, and R. Paus, *The hair follicle as a dynamic miniorgan*. Current Biology, 2009. **19**(3): p. R132-R142.
100. Schmidt-Ullrich, R. and R. Paus, *Molecular principles of hair follicle induction and morphogenesis*. Bioessays, 2005. **27**(3): p. 247-261.
101. Millar, S.E., *Molecular mechanisms regulating hair follicle development*. Journal of Investigative Dermatology, 2002. **118**(2): p. 216-225.

102. Rendl, M., L. Polak, and E. Fuchs, *BMP signaling in dermal papilla cells is required for their hair follicle-inductive properties*. *Genes & development*, 2008. **22**(4): p. 543-557.
103. LINDNER, G., et al., *Involvement of hepatocyte growth factor/scatter factor and met receptor signaling in hair follicle morphogenesis and cycling*. *The FASEB Journal*, 2000. **14**(2): p. 319-332.
104. Stenn, K. and R. Paus, *Controls of hair follicle cycling*. *Physiological reviews*, 2001. **81**(1): p. 449-494.
105. Zheng, Y., et al., *Organogenesis from dissociated cells: generation of mature cycling hair follicles from skin-derived cells*. *Journal of investigative dermatology*, 2005. **124**(5): p. 867-876.
106. Stenn, K.S. and G. Cotsarelis, *Bioengineering the hair follicle: fringe benefits of stem cell technology*. *Current opinion in biotechnology*, 2005. **16**(5): p. 493-497.
107. Larouche, D., et al., *Tissue-engineered skin preserving the potential of epithelial cells to differentiate into hair after grafting*. *Tissue Engineering Part A*, 2010. **17**(5-6): p. 819-830.
108. Frater, R. and P. Whitmore, *In vitro growth of postembryonic hair*. *Journal of Investigative Dermatology*, 1973. **61**(2): p. 72-81.
109. Philpott, M.P., M.R. Green, and T. Kealey, *Human hair growth in vitro*. *Journal of cell science*, 1990. **97**(3): p. 463-471.
110. Philpott, M., M. Green, and T. Kealey, *Rat hair follicle growth in vitro*. *British Journal of Dermatology*, 1992. **127**(6): p. 600-607.
111. Fuchs, E., et al., *At the roots of a never-ending cycle*. *Developmental cell*, 2001. **1**(1): p. 13-25.

## *Ringraziamenti*

*Le strade non siamo sempre noi a sceglierle, ma talvolta capita che siano loro a scegliere noi...un intricato dedalo di eventi....che poi alla fine ti porta ad essere in un posto piuttosto che in un altro.*

*Grazie a tutti coloro con cui ho lavorato in questi anni....*

*partendo dal prof. Netti...che da quando mi disse..."dobbiamo fare il pelo"...ha ridotto di molto le mie già scarse ore di sonno.*

*..passando per Ciccio e Giorgia, da cui, grafici in scale di grigio, barre uguali a tutte le immagini...sono stati suggerimenti fondamentali...per non vedere scene tipo: "nooo...questo no..(con una mano in fronte e l'altra dietro la schiena)".*

*Costantino, Fzia, Virginia, Sara, Brunella, Francesca M, Filomena, Francesca R Claudia, Bernadette...per il confronto avuto in questi anni...*

*tutti i "festaioli di piazzale tecchio" ...anche se ve lo devo dire....quel gruppo è un bombardamento...*

*agli iit-iani...Valeria Manuela Raffaella Fabio Valentina Fnzo...*

*Spero di avervi restituito, almeno in parte...qualunque cosa si debba restituire in questi casi...*

*In ultimo....ringrazio i miei tre "animaletti"...voi siete il mio motore....e tutto quello che faccio...o provo a fare...credetemi è per voi!! Vi adoro!!*

*Chiara...ovviamente il più grande grazie va a te!!*

*Le nostre prove non sono state solo lavorative ...e senza di te gestire tutto sarebbe stato impossibile... sei la mia compagna di tutto...grazie di tutto, e per tutto... Ti Amo..*